

FINITE ELEMENT EVALUATION OF HYDROGEN SOLUBILITIES DUE TO THERMAL RESIDUAL STRESSES IN PALLADIUM-ALUMINA COMPOSITES

1998 *A Thesis Submitted
in Partial Fulfilment of the Requirements
for the Degree of*

MASTER OF TECHNOLOGY

by
SOMNATH DAS

to the
**DEPARTMENT OF MATERIALS AND METALLURGICAL ENGINEERING
INDIAN INSTITUTE OF TECHNOLOGY, KANPUR**

MAY 2000

6 OCT 2000 /MME

CENTRAL LIBRARY
I. I. T., KANPUR

NO. A 132610

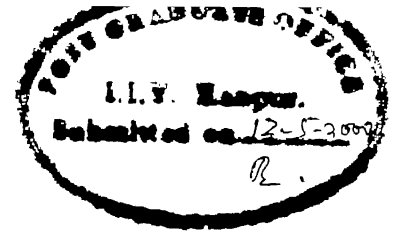
TH

MME/2000/M

D262



A132010



CERTIFICATE

This is to certify that the present work, entitled **FINITE ELEMENT EVALUATION OF HYDROGEN SOLUBILITIES DUE TO THERMAL RESIDUAL STRESSES IN Pd-Al₂O₃ COMPOSITES** has been carried out by Mr. SOMNATH DAS under my supervision and to the best of my knowledge it has not been submitted elsewhere for a degree.

(Dr. R. BALASUBRAMANIAM)

Associate Professor

Department of Materials & Metallurgical Engineering

Indian Institute of Technology

Kanpur 208016, INDIA

May 12, 2000

Acknowledgement

I acknowledge with sincerity and deep sense of gratitude the expert guidance and continuous encouragement provided by my thesis supervisor Dr. R. Balasubramaniam throughout the course of this thesis.

I wish to express my sincere appreciation of valuable help and suggestions obtained from Prof. P.M. Dixit (Mech. Engg.). Without his valuable suggestion it was difficult to complete this thesis. Special thanks to him for providing me all possible helps regarding FEM Formulation and Simulation.

Thanks are due to all my friends from department and outside who have helped me in various capacities throughout my stay at Kanpur. Prominent amongst them are Tapan, Badrujjaman, Onong, Sourabh, Bansal, Kapil, Sharad, Ashish, Rohit, Samit, Kundu, Pranay, Bama and Ajay. The list goes on and is in no means exhaustive.

At the end I am thankful to all those who helped me directly or indirectly during my stay in IIT Kanpur.

Somnath Das

CONTENTS

	Page Number
Abstract	i
List of Figures	iii
List of Tables	vii
Chapter 1 INTRODUCTION	
1.1 Hydrogen Solubilities In Composites	1
1.2 Finite Element Method	2
1.3 Work Plan	2
1.3.1 Plan For Spherical Precipitates In An Infinite Spherical Matrix	3
1.3.2 Plan For Cylindrical Precipitates In An Infinite Cylindrical Matrix	3
Chapter 2 LITERATURE REVIEW	
2.1 Internal Oxidation and Hydrogen Solubilities in Composites	4
2.1.1 Hydrogen Isotherms After Internal Oxidation	4
2.1.2 Theoretical Analysis Of Hydrogen Solubility	5
2.2 Residual Stresses	11
2.2.1 Thermal Effects	12
2.3 Brief Introduction Of Finite Element Method (FEM) and Its Application	17
2.4 Helmholtz Free Energy	18
Chapter 3 SPHERICAL PRECIPITATES	
3.1 Formulation of Basic Equations	20
3.2 Variational FEM Method	23
3.2.1 Shape functions	25
3.3 Estimation Of Displacements	28

3.4	Estimation Of Strains	28
3.5	Estimation Of Stresses	33
3.6	Estimation Of Solubility Enhancement Ratio	37
3.7	Estimation Of Helmholtz Free Energy	41
3.8	Limitations Of The Model	45
Chapter 4	CYLINDRICAL PRECIPITATES (CASE - I)	
4.1	Formulation Of Basic Equations	46
4.2	Variational FEM Method	49
4.2.1	Calculation Of $\{B\}^e$ matrix	52
4.2.2	Gaussian Quadrature	52
4.2	Estimation of Displacements	56
4.3	Estimation Of Strains	63
4.4	Estimation Of Stresses	63
4.4.1	Estimation Of Polar Stresses From Cartesian Stresses	67
4.5	Estimation of Solubility Enhancement Ratio	78
4.6	Estimation of Helmholtz Free Energy	78
Chapter 5	CYLINDRICAL PRECIPITATES (CASE – II)	84
Chapter 6	CYLINDRICAL PRECIPITATES (CASE - III)	89
6.1	Limitations Of Case I, Case II and Case III.	95
Chapter 7	CONCLUSIONS AND SCOPE FOR FUTURE WORK	
7.1	Conclusions	96
7.2	Scope For Future Work.	98
Chapter 8	REFERENCES	99

ABSTRACT

If a Pd alloy containing a substitutional base element (Al) is exposed to an oxidizing environment at high temperatures, internal oxidation of the base element may occur if the solute is present in small quantities. Internal oxidation of Pd-Al alloys results in alumina (Al_2O_3) precipitates within the Pd-Al matrix, this produces Pd- Al_2O_3 composites. The shape of alumina precipitates varies as a function of temperature. The thermal expansion coefficient and Young's Modulus of Pd matrix ($\alpha_m = 11.5 \times 10^{-6} \text{ K}^{-1}$, $E_m = 123 \text{ GPa}$) is different from that of the Al_2O_3 precipitate ($\alpha_m = 8.0 \times 10^{-6} \text{ K}^{-1}$, $E_m = 380 \text{ GPa}$). Therefore residual stresses are generated in the composites upon cooling from the oxidation temperature due to difference of thermal expansion coefficients of Pd and Al_2O_3 precipitates. It is known that Hydrogen is absorbed by Pd-matrix and the presence of these residual tensile stresses in the Pd matrix results in solubility enhancements. This demonstrates the nature of stresses developed in the composite and therefore hydrogen has been used as a probe for estimating residual stresses in Pd-alumina composites.

The strains and stresses developed in the Pd- Al_2O_3 composite have been thoroughly studied by Finite Element Method (FEM). In this study, the FEM has been applied to study the thermal strains and stresses at every point generated in the Pd- Al_2O_3 composite. Two types of composites have been utilized to study the strains and stresses developed in the composite. The first model considers spherical Al_2O_3 precipitates distributed in an infinitely spherical matrix. This model has been utilized to obtain strains, stresses, thermal residual stress, solubility enhancement ratio and Helmholtz free energy.

The second model considers cylindrical Al_2O_3 precipitates in an infinite cylindrical matrix. This model is a plain strain case. FEM has been applied for various shapes and positions of the precipitates. Strains, stresses, solubility enhancement ratio and Helmholtz free energy are obtained from this model.

Strains obtained Pd matrix are always higher than Al_2O_3 precipitates due to high thermal expansion of Pd matrix. Higher thermal residual strains and stresses are developed in the composite with higher temperature difference. Stresses in Al_2O_3

precipitates are higher than Pd matrix, this is due to higher young's modulus of precipitates. Tangential stress for Al_2O_3 are tensile where as compressive stresses are developed in Pd matrix. Thermal residual stresses result in solubility ratio, higher ratios are obtained for higher temperature difference. Helmholtz free energies (HFEs) solely depend on strain and the temperature of the composite but not on the stresses. As the Pd strains are always higher than Al_2O_3 so their HFEs are always higher.

List of Figures

Figures		Page number
2.1	Dilute phase hydrogen Isotherms for completely oxidized $\text{Pd}_{0.97}\text{Al}_{0.03}$ measured after an initial isotherm measurement followed by evacuation at 323K; Δ ,1073K; O ,1173K; $[\]$, 1273K [1].	6
2.2	Variation of solubility enhancement factor as a function of P_{H_2} for the alloy $\text{Pd}_{0.97}\text{Al}_{0.03}$ measured at 32K after complete oxidation at : Δ , 1073K; O , 1173K; $[\]$, 1273K [1].	7
2.3	Estimated residual stresses induced in the Ti-14Al-21Nb matrix reinforced with 35% SCS-6 fibers cool down from the strain-free temperature (806° C) to room temperature [27].	14
2.4	Equivalent stress in the A357.0 matrix around SiC fiber at the fiber/matrix interface (air cooling: temperature of air is 27° C) [19].	15
2.5	Radial stress at the interface as a function of temperature during cooling room temperature at K/s and subsequent heating at various rates [26].	16
3.1	A schematic diagram for an idealized ceramic configuration in Infinite spherical matrix.	21
3.2	Discretization of the quarter domain using 1-D elements.	24
3.3.a	Spherical Al_2O_3 precipitate is inside and spherical Pd is outside for IO case at $\Delta T = 1000\text{K}$.	30
3.3.b	Spherical Al_2O_3 precipitate is outside and spherical Pd is inside for OI case at $\Delta T = 1000\text{K}$.	30
3.4	Variation of displacements as a function of radial distance at $\Delta T = 1000\text{K}$ for IO and OI case.	31
3.5	Variation of radial strain (ϵ_{rr}) as a function of radial distance at $\Delta T = 1000\text{K}$ for IO and OI case.	32
3.6	Variation of tangential strain ($\epsilon_{\theta\theta}$) as a function of radial distance at $\Delta T = 1000\text{K}$ for IO and OI case.	34

3.7	Variation of radial stress (σ_{rr}) as a function of radial distance at $\Delta T = 1000K$ for IO and OI case.	35
3.8	Variation of tangential stress ($\sigma_{\theta\theta}$) as a function of radial distance at $\Delta T = 1000K$ for IO and OI case.	36
3.9	Variation of Tensile Hydrostatic stress(σ_h^m) of as a function of radial distance at $\Delta T = 1000K$ for IO and OI case.	38
3.10	Variation of solubility enhancement ratio as a function of Al_2O_3 precipitate volume fraction for different temperature difference values for IO case.	39
3.11	Variation of solubility enhancement ratio as a function of Al_2O_3 precipitate volume fraction for different temperature difference values for OI case.	40
3.12	Variation of Helmholtz free energy as a function of radial distance at $\Delta T = 1000K$ for IO and OI case.	42
3.13	Variation of Helmholtz free energy as a function of Al_2O_3 precipitate volume fraction for different temperature difference values for IO case.	43
3.14	Variation of Helmholtz free energy as a function of Al_2O_3 precipitate volume fraction for different temperature difference values for OI case.	44
4.1	Discretization of the quarter domain using 2-D elements.	48
4.2	8-Noded Isoparametric Serendipity element.	
4.3	Temperature profile as a function of radial distance for $\Delta T = 800K$.	57
4.4.a	Cylindrical Al_2O_3 precipitate is inside and cylindrical Pd is outside for IO case at $\Delta T = 800K$.	58
4.4.b	Cylindrical Al_2O_3 precipitate is outside and cylindrical Pd is inside for OI case at $\Delta T = 800K$.	58
4.5.a	Variation of displacements at nodal points as a function of distance along x-axis for $\Delta T = 800K$ for IO case.	59
4.5.b	Variation of displacements at nodal points as a function of distance along x-axis for $\Delta T = 800K$ for OI case.	60
4.6.a	Variation of displacements at nodal points as a function of distance along y-axis for $\Delta T = 800K$ for IO case.	61
4.6.b	Variation of displacements at nodal points as a function of distance along y-axis	

	for $\Delta T=800K$ for OI case.	62
4.7	Variation of ε_{xx} strain as a function of distance along x-axis for $\Delta T=800K$.	64
4.8	Variation of ε_{yy} strain as a function of distance along x-axis for $\Delta T=800K$.	65
4.9	Variation of ε_{xy} strain as a function of distance along x-axis for $\Delta T=800K$.	66
4.10.a	Variation of σ_{xx} stress as a function of distance along x-axis for $\Delta T=800K$ for IO case.	68
4.10.b	Variation of σ_{xx} stress as a function of distance along x-axis for $\Delta T=800K$ for OI case.	69
4.11.a	Variation of σ_{yy} stress as a function of distance in x-direction for $\Delta T=800K$ for IO case.	70
4.11.b	Variation of σ_{yy} stress as a function of distance in x-direction for $\Delta T=800K$ for OI case.	71
4.12	Variation of σ_{xy} stress as a function of distance along x-axis for $\Delta T=800K$ for IO case.	72
4.13.a	Variation of σ_{rr} radial stress as a function of distance along x-axis for $\Delta T=800K$ for IO case.	74
4.13.b	Variation of σ_{rr} radial stress as a function of distance along x-axis for $\Delta T=800K$ for OI case.	75
4.14.a	Variation of $\sigma_{\theta\theta}$ tangential stress as a function of distance along x-axis for $\Delta T=800K$ for IO case.	76
4.14.b	Variation of $\sigma_{\theta\theta}$ tangential stress as a function of distance along x-axis for $\Delta T=800K$ for OI case.	77
4.15.a	Variation of solubility enhancement curve as a function of ceramic volume fraction for different temperature difference values for IO case.	80
4.15.b	Variation of solubility enhancement curve as a function of ceramic volume fraction for different temperature difference values for OI case.	81
4.16.a	Variation of Helmholtz free energy as function of ceramic volume fraction at	

different temperature differences for IO case.	82
4.16.b Variation of Helmholtz free energy as function of ceramic volume fraction at different temperature differences for OI case.	83
5.1 Discretization of the quarter domain using 2-D elements having intermediate 8-elements precipitates.	86
5.2 Variation of σ_r radial stress as a function of distance along x-axis for $\Delta T=800K$ for case II.	87
5.3 Variation of solubility enhancement curve as a function of ceramic volume fraction for different temperature difference values for case II.	88
5.4 Variation of Helmholtz free energy as function of ceramic volume fraction at different temperature differences for case II.	89
6.1 Discretization of the quarter domain using 2-D elements having intermediate 4-elements precipitates.	90
6.2 Variation of σ_r radial stress as a function of distance along x-axis for $\Delta T=800K$ for case III.	91
6.3 Variation of solubility enhancement curve as a function of ceramic volume fraction for different temperature difference values for case III.	92
6.4 Variation of Helmholtz free energy as function of ceramic volume fraction at different temperature differences for case III	94

List of Tables

Table	Page numbers
2.1 Calculated hydrostatic stress and solubility enhancement for different volume fraction.	10
3.1 Material properties of composites.	27
3.2 Validation of results with theoretical & FEM results.	29
6.1 Comparison of solubility curve for two cases.	93

Chapter 1

INTRODUCTION

One method to obtain Pd-Al₂O₃ composites is by internal oxidation of Pd-Al alloy at high temperature. Oxygen dissolves in the Pd-Al alloys and internally oxidation of Al produces alumina (Al₂O₃) precipitate in the nearly pure Pd matrix. The thermal expansion coefficient of Pd matrix ($\alpha_m = 11.5 \times 10^{-6} \text{ K}^{-1}$, $E_m = 123 \text{ GPa}$) is different from that of the Al₂O₃ precipitate ($\alpha_m = 8.0 \times 10^{-6} \text{ K}^{-1}$, $E_m = 380 \text{ GPa}$). Thermal residual stresses developed when ideally oxidized alloys are cooled from high temperature to low temperature due to mismatch of material properties. These thermal residual stresses can be modeled theoretically also.

1.1 Hydrogen Solubilities in Composites

The stress distribution in the Pd-Al₂O₃ composite is complex. Hydrogen can be used as probe to understand the stress generated within the composite [1]. Hydrogen behavior in Pd is well-known [1] and additional stress in the Pd-matrix results in the solubility enhancements [2].

Solubility enhancements ratio (n'/n) can be calculated from the equation [3].

$$\frac{n'}{n} = \exp\left(\frac{\sigma_h^m \cdot V_H}{RT}\right) \quad 1.1$$

Where,

V_H = Partial molar volume of hydrogen.

T = Temperature of solubility measurement

σ = Tensile hydrostatic stress present in the Pd matrix.

n' and n are the atom fractions of hydrogen in equilibrium in the stress field. (σ_h^m) of the precipitate and in the absence of stress (i.e. $\sigma_h^m = 0$), respectively.

In the present case above ratio is always greater than 1.0 for Pd-Al₂O₃ composite because tensile stress are generated in the Pd matrix on cooling down.

Experimentally, we can find the solubility enhancement ratio. However, the procedure does not help in understanding how the strains and stresses are distributed within the composite. These can be easily studied by Finite Element Method (FEM). Here FEM has been applied to understand the stresses developed in Pd-Al₂O₃ composites. The radial stress generated in the Pd matrix helps in calculating (σ_r/σ_t) ratio.

1.2 Finite Element Method

Finite element method (FEM) is a versatile method for the approximate solution of the differential equations. Its use in industry is enormous and it is said that without it many problems would remain unsolvable. FEM method is particularly applicable for the stress-strain relations as these relations involve differential equations. FEM has been applied for two types of models. Spherical precipitate is embedded in infinite spherical matrix in the first model and second model considers cylindrical precipitate in infinite cylindrical matrix.

Hydrogen solubility enhancements in Pd-Al₂O₃ composite only provides information about the maximum radial stress build in the Pd-matrix. It does not tell about the distribution of radial and tangential stress build in the composite. FEM model can provide the radial stress, tangential stress and tensile stress generated throughout the composite at different positions.

1.3 Work Plan

Elastic FEM formulation has been evaluated to study various stresses generated in Pd-Al₂O₃ composite. Two types of models are evaluated through FEM formulation. Spherical precipitates in infinite spherical matrix are considered in first model whereas the second model deals with cylindrical precipitate in infinite cylindrical matrix.

1.3.1 Plan For Spherical Precipitates In An Infinite Spherical Matrix

Assumptions are made before applying this model. Respective force balance equations are established and stress equations are evaluated involving displacements and strains. The variation method was used for solving the FEM model. In order to simplify

the model, two noded element was used to get displacement at every nodal point. Strains and stresses were evaluated at every element to show how strains and stresses were generating in whole composite. Results were generated by varying the temperature by keeping the volume fraction of Al_2O_3 precipitates same, and the vice-versa. Finally, results are obtained for solubility enhancement ratio and Helmholtz free energy.

1.3.2 Plan For Cylindrical Precipitate In An Infinite Cylindrical Matrix

Firstly, basic assumptions were made before evolving this model. Respective differential equations were generated for stresses and strains. Variation method was applied to solve the differential equations. Axis-symmetric case was made to simplify the model, eight noded isoparametric serendipity isoparametric element was evaluated for generating displacements in co-ordinate axis. Stresses were transformed into polar co-ordinates from cartesian co-ordinates for calculating solubility ratio and Helmholtz free energy.

Chapter 2

LITERATURE REVIEW

2.1 Internal Oxidation And Hydrogen Solubilities In Composites

If a Pd alloy containing a substitutional base element is exposed to an oxidizing environment at high temperatures, internal oxidation of the base element may occur if the solute is present in small quantities and it has been studied in a variety of noble metal-base metal alloy systems [4,5].

Al particle internally oxidizes to Al_2O_3 precipitates which results in formation of Pd- Al_2O_3 composite at higher temperature. As the temperature is cooled from high temperature to room temperature, thermal residual stresses are generated at the composite due to mismatch of material properties of Pd and Al_2O_3 precipitates in composite.

Thermal residual stresses generation in composite is complex in nature. It is well known that Pd absorbs H_2 and this property of H_2 has been utilized to study stresses developed in the composite. Additional stress in the composite results in the solubility enhancements and given by equation 1.1. Hydrogen can be used as probe element to know the stress distribution in composite. Higher the solubility enhancements, higher will be stresses. These stresses developed depend upon the temperature of internal oxidation and precipitate volume fraction.

2.1.1 Hydrogen Isotherms After Internal Oxidation

Hydrogen solubility in Pd matrix helps in calculating hydrogen solubility isotherm in α -phase for alloy and pure Pd is shown in Figure 2.1. The Figure 2.1 shows that the low pressure solubilities decrease only slightly and the terminal hydrogen solubilities increase significantly with increase significantly with increasing mol fraction of Al, X_{Al} . There is only a small difference between the dilute phase H_2 solubilities of Pd and the Pd-Al alloy because of the low Al content [1].

The solubility of hydrogen at 323 K is enhanced in the dilute region of the internally oxidized Pd-Al alloys after complete oxidation at 1073 K, 1173 K and 1273 K as can be seen in Fig. 2.1 for Pd-Al alloys after they have been internally oxidized.

In Fig. 2.1 the hydrogen content is expressed as the mol H-to-mol metal ratio where the latter is that of the initial, unoxidised alloy. If M is computed, instead, on the basis of mols of Pd matrix after oxidation, the calculated H/M values are very similar [1]. It can be seen that the hydrogen solubility enhancement decreases with increasing oxidation temperature. The solubility enhancement factor (n'/n) is defined as the ratio of hydrogen solubility at a fixed hydrogen chemical potential, i.e. fixed equilibrium hydrogen pressure, in the dilute phase after oxidation treatment (n') to that in pure Pd (n). It has been shown [6] that the Pd matrix after internal oxidation of Pd-Al alloys is essentially pure, and therefore, if there were no influence of the ceramic particles on the solubility, the solubility enhancement, (n'/n), would be 1.

The variation of the solubility enhancement factors alloys are shown as a function of equilibrium hydrogen pressures in Fig 2.2, which shows that the enhancement factor for complete oxidation at all of the temperatures is larger at the lower, as compared to the higher pressures where it becomes relatively constant. At all of the equilibrium hydrogen pressures, lower oxidation temperatures lead to greater solubility enhancements in the dilute phase isotherms at 323 K.

2.1.2 Theoretical Analysis Of Hydrogen Solubility

At the relatively high temperatures employed for the internal oxidation 983, 1073, 1173 and 1273 K, it seems reasonable to assume that the transformation stresses which result from the precipitation of alumina particles at the above temperatures are largely accomplished by the relaxation of the matrix. Stresses will develop, however, during cooling from the oxidation temperature. They will start to develop at a temperature below approximately half of the melting point (K) of Pd (913 K). The stresses develop because

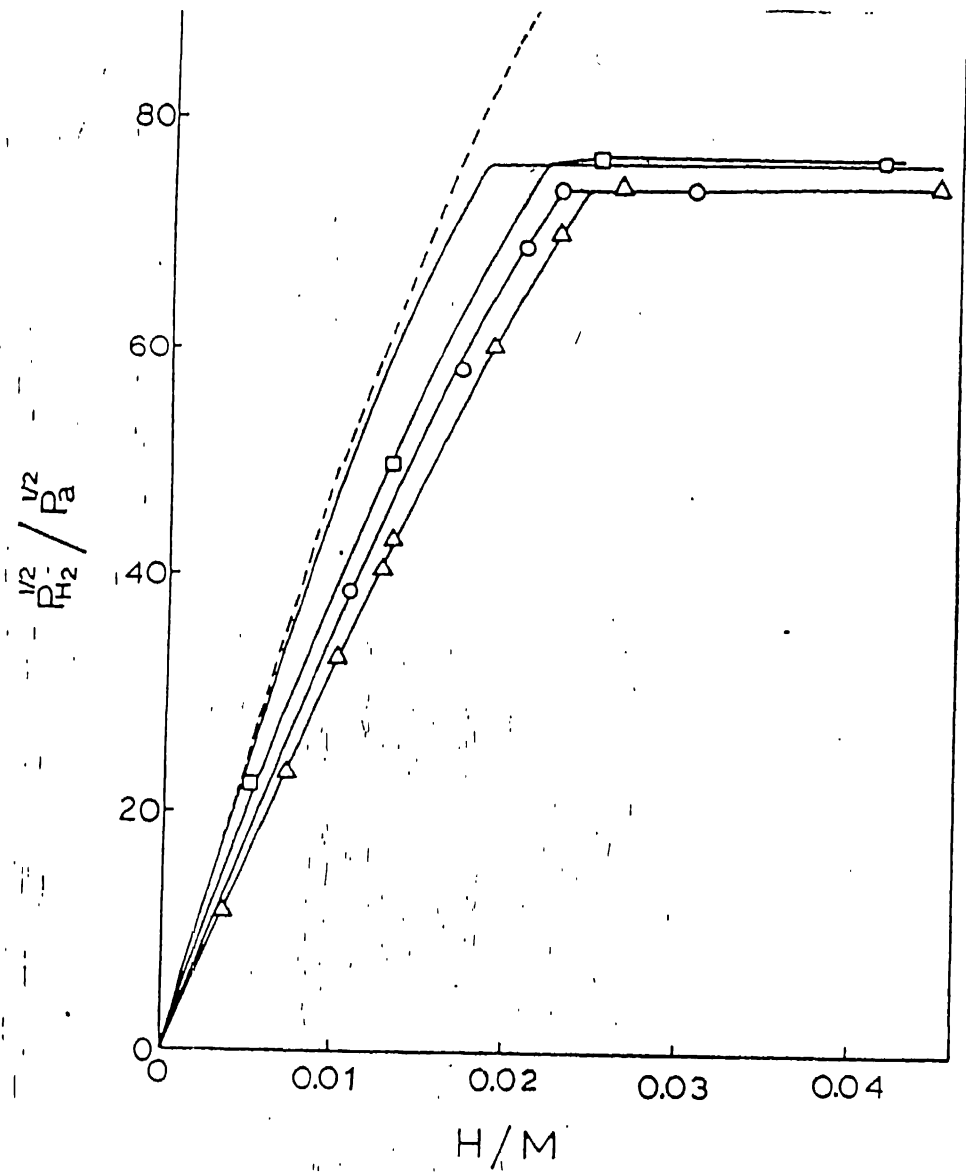


Figure 2.1 -- Dilute phase hydrogen Isotherms for completely oxidized Pd_{0.97}Al_{0.03} measured after an initial isotherm measurement followed by evacuation at 323K: Δ, 1073K; O, 1173K; □, 1273K [1].

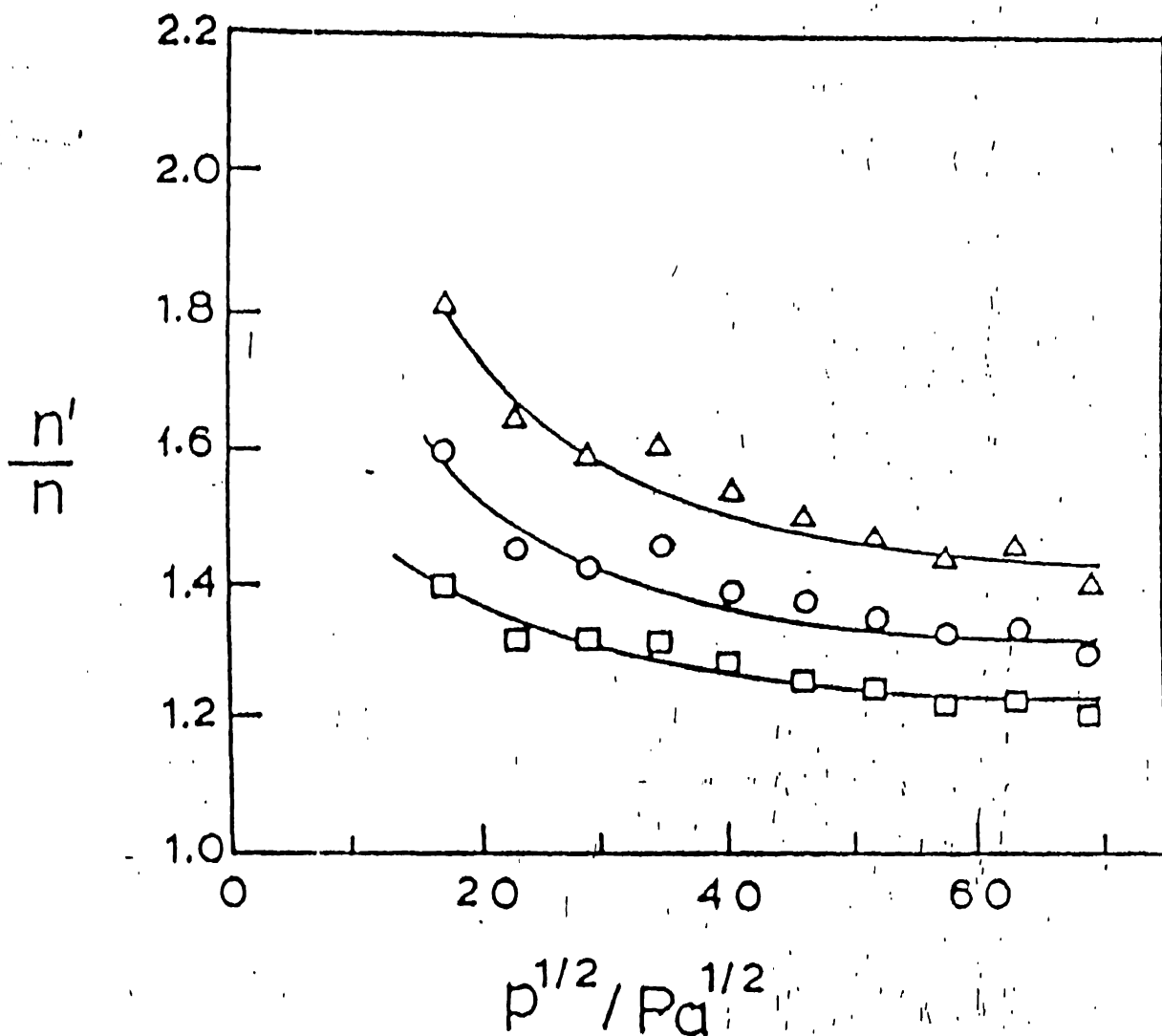


Figure 2.2 - Variation of solubility enhancement factor as a function of P_{H_2} for the $Pd_{0.97}Al_{0.03}$ alloy measured at 32K after complete oxidation at : Δ , 1073K; O, 1173K; \square , 1273K [1].

of the difference in the coefficients of thermal expansion of the palladium matrix (α_m) and the embedded alumina ceramic (α_c) precipitates. Upon cooling, an imbedded ceramic particle contracts to smaller extent than the Pd matrix and hence the metallic matrix will be subjected to tensile and the ceramic precipitates to compressive stress. These states of stress resulting from cooling ceramic precipitates within metallic matrices have been experimentally verified in analogous systems by X-ray diffraction, e.g. in Al-graphite [7] and Al-SiC particulate-composite [8] systems where an average tensile stress state was found in the matrix phase.

The thermal stresses developed in the spherical alumina precipitates and matrix have been derived for composite systems by assuming elastic. Among the models which have been proposed, that of Kim et al, [2] seems to be the most realistic because it accounts for the volume fraction of the precipitates in a finite matrix, whereas the other models are based on a single ceramic particle in an infinite metallic matrix. According to this elastic model of Kim et al.[2] the tensile hydrostatic stress (σ_h^m) developed in the matrix (superscript m), which can be shown to be independent of distance from the precipitate-matrix interface, is given by [1]

$$\sigma_h^m = \frac{-P_1 a^3 (1 + \nu_m)}{a^3 + 2b^3 + \nu_m (a^3 - 4b^3)} \quad 2.1$$

where P_1 , the radial pressure at the metal-ceramic interface, is given by

$$P_1 = \frac{-(\alpha_m - \alpha_c) \Delta T}{\frac{1}{E_m} \left[\nu_m + (1 - \nu_m) \frac{b^3 - a^3 - \nu_m (a^3 + 2b^3)}{a^3 + 2b^3 + \nu_m (a^3 - 4b^3)} \right] + \frac{1 - 2\nu_c}{E_c}} \quad 2.2$$

In the above equations, α_m is the thermal expansion coefficient of the matrix, α_c is the thermal expansion coefficient of the ceramic precipitate, T is the difference between the temperature at which relaxation of the lattice ceases, which is taken as one-half of the melting point in Kelvin, and 323 K (the temperature at which the isotherms were measured), E_m is the elastic modulus of Pd (123 GPa), E_c the elastic modulus of alumina (380 GPa), ν_m the Poisson's ratio of the matrix (0.375), ν_c the Poisson's ratio of alumina (0.250), a is the radius of the precipitate and b is the average half distance between the

center of two neighbouring precipitates. For a dispersed spherical precipitate system, the relationship between a , b and ϕ (the precipitate volume fraction) is obtained from [9]

$$b = a + \frac{a \exp(8\phi)}{6\phi^{1/3}} \int_{\phi}^{\infty} x^{-2/3} e^{-x} dx \quad 2.3$$

The above expression is accurate at low volume fractions, i.e. when $\phi \leq 0.1$. The tensile hydrostatic stress developed in the matrix is a function of the elastic properties of the matrix and precipitate, and the volume fraction of precipitate. It is not, surprisingly, a function of distance from the ceramic/matrix interface because the terms involving this distance cancel out when individual stress components are summed to obtain the net hydrostatic stress[2]. The hydrostatic stresses in the matrix for different volume fractions of alumina, as calculated from equations (2.1) to (2.3), are tabulated in Table 2.1.

If the tensile hydrostatic stress is much less than the modulus of Pd, which is true in the present case, then the interaction energy between the stress field and one mole of hydrogen atoms is given by [10]

$$\frac{n'}{n} = \exp\left(\frac{E(\sigma_h^n)}{RT}\right) \quad 2.4$$

where V_H is the partial molar volume of hydrogen in Pd ($V_H = 1.77 \times 10^{-6} \text{ m}^3/\text{mol}$). The absorption of hydrogen in the stress field of the ceramic precipitate is given using the Boltzmann approximation as

$$\frac{n'}{n} = \exp\left(\frac{\sigma_h^n V_H}{RT}\right) \quad 2.5$$

where n' and n are the atom fractions of hydrogen in equilibrium in the stress field (σ_h^m) of the precipitate and in the absence of the stress field (i.e. $\sigma_h^m = 0$), respectively. The above equation is integrated over the entire matrix from the ceramic-matrix interface ($r = a$) to half the distance of separation of the spherical ceramic precipitates ($r = b$). The b/a ratio can be estimated from equation [2.3].

φ	σ_h/MPa (spherical)	n'/n (spherical)	σ_h/MPa (cylindrical)	n'/n (cylindrical)
0.02	81	1.06	123	1.09
0.03	148	1.10	127	1.09
0.04	254	1.18	132	1.09
0.05	298	1.22	136	1.09
0.06	337	1.25	140	1.10
0.07	372	1.28	145	1.10
0.08	404	1.31	150	1.10
0.09	433	1.33	154	1.11
0.10	460	1.35	159	1.11

Table 2.1 - Calculated hydrostatic stresses and solubility enhancement for spherical and cylindrical alumina precipitates in Pd for $\Delta T=590\text{K}$ and $T=323\text{K}$ for n'/n .

The enhanced concentration in the presence of the tensile stress field in the Pd-matrix due to the ceramic precipitates is then given by,

$$\frac{n'}{n} = \frac{\int_0^b \int_0^{2\pi} \int_0^\pi \exp\left(\frac{E}{RT}\right) r^2 \sin\theta dr d\theta d\phi}{\int_0^b \int_0^{2\pi} \int_0^\pi r^2 \sin\theta dr d\theta d\phi} = \exp\left(\frac{E(\sigma_h^m)}{RT}\right) \quad 2.6$$

where $E(\sigma_h^m)$ is given by equation (2.1) using equations (2.2) and (2.5); it is surprising that n'/n does not depend on r, θ and ϕ . This is because the hydrostatic stress developed in the matrix is only a function of a and b , and does not depend upon the distance from the ceramic-matrix interface. From the known elastic properties of the matrix and the precipitate and the volume fraction of the precipitates, the solubility enhancement in the matrix due tensile hydrostatic stress can be calculated using equation [2.6]. For the case of spherical alumina precipitates in Pd, the calculated solubility enhancements for different volume fractions of alumina are tabulated in Table 2.1.

2.2 Residual Stresses

Residual stresses are the system of stresses which can exist in a body when it is free from external forces. They are sometimes referred to as internal stresses, or locked-in stresses. Classically, residual stresses are categorized into three types according to the length scale over which they act [11]. Type-I stresses act over distances measured in millimeters and are often referred to as macrostresses. They can typically develop within the material following welding, machining, or surface finishing processes. Stresses that act over length scales that are typical of a microstructure are termed type-II stresses. The residual stresses that are developed in MMCs due to the interactions between the reinforcement and the matrix belong to type-II stresses. Finally, the stresses that exist at an atomic scale and vary over individual grains are described as type -III stresses. Type-II and III are often collectively referred to as microstresses.

2.2.1 Thermal Effects

Thermal stresses in metal-matrix composites result during cooling either from temperature gradients within the specimen (leading to type-I stresses) or from a mismatch of coefficients of thermal expansion (CTE) between the constituents (introducing type-II stresses) [12]. The former effect can be controlled by slow cooling, but the latter is inherent and will always give interaction stresses unless the CTEs of the constituents are identical. Typically, the difference in CTEs in metal-matrix composites is large, for example Pd ($\alpha_m = 11.5 \times 10^{-6}/K$) and Al_2O_3 ($\alpha_c = 8.0 \times 10^{-6}/K$). Processing temperatures of metal-matrix composites are usually several hundred degrees above ambient. Thus, on cooling, the larger contraction of the matrix compared to the reinforcement leads to tensile and compressive residual stresses in the matrix and the reinforcement, respectively. In continuous fiber or aligned whisker composites, the anisotropic shape of the reinforcement induces larger axial than transverse residual stresses.

Most of the early analytical models proposed to estimate the thermal residual stresses are based on Eshelby's equivalent inclusion method [13,14]. Using Eshelby's method, the stress fields in the region surrounding a reinforcement, which form as a result of a uniform temperature change, may be determined [15,16]. Eshelby's method has also been used to predict the yield stress and the work hardening rate of metal matrix composites [17] as well as to estimate the overall thermal expansion characteristics of a heterogeneous solid containing a dispersion of aligned inclusions [18]. However, most of the published analytical studies are limited to simplified cases, such as those involving a uniform temperature change boundary condition, a single reinforcement in an infinite matrix, or the case of a perfectly elastic or elastic-perfectly plastic matrix. When the composite system involves non-homogenous deformation as a result of matrix plasticity and incorporates multiple reinforcements containing sharp corners, the analytical formulation deduced from analytical methods can become intractable and the need for a numerical analysis arises. Numerical techniques, such as the finite element method (FEM), have been widely used by a number of investigators to predict the residual stresses and the constitutive response of the MMCs [19-24].

Thermal residual stresses have been studied in several metal-matrix systems: Al/SiC (Ho 1990 [19]; Ho and Saigal 1994 [21]; Levy and Papazian 1991 [22]; Shi and Arsenault 1991 [23]; Suresh and Nakamura 1993 [24], Ho and Saigal 1994 [25]; Suery et al. 1993 [26]), Ti alloys composites (Saigal et al. 1992 [27], Durodola and Derby 1994 [28]; Bigelow 1992 [29]) and Pd alloy composites (Balasubramaniam et al. 1997 [1]; Eastman and Ruhle 1989 [30]), by a variety of techniques that include X-ray diffraction (Tsai et al. 1992 [7]; Ledbetter and Austin 1987 [8] and Cox 1987 [31]) and neutron diffraction (Ledbetter and Austin 1987 [8]; Krawitz 1990 [32] and Majumdar et al. 1991 [33]).

Saigal et al. [27] measured thermal residual stresses developed during cooling of silicon carbide fiber-reinforced titanium aluminide matrix composite using neutron diffraction and compared with those obtained by finite element analysis. Figure 2.3 illustrates the estimated thermally induced residual stresses in the titanium aluminide matrix as the composite is cooled from strain-free temperature of 806°C.

In modeling, the process of generation of thermal residual stresses in cast SiC fiber-reinforced aluminum alloy A357.0 matrix composites, Ho and Saigal [19] employed thermo-elastoplastic finite element analysis. Figure 2.4 shows the von Mises' equivalent stresses in the matrix around fiber at the fiber/matrix interface as the temperature decreases from 620 to 27°C [19].

Suery calculated the thermal residual stresses in 15 vol.-% SiC particulate reinforced Al 1100 -O composite [26]. In their study, it was found that the reheating of the composites after quenching to room temperature changes the sign of the radial stress, which become positive (Figure 2.5). Figure 2.5 shows the variation of the radial stress with temperatures (from 660°C down to 20°C and up to 660°C) at the particle/matrix interface. The combined effects of thermal residual stresses and fiber spatial distribution on the deformation of a 6061 aluminum alloy containing a fixed concentration unidirectional boron fibers have analyzed by Suresh and Nakamura [24] using detailed finite element methods. The model involves an elastic-plastic matrix, elastic fibers, and mechanically bonded interface. The results indicate that both the fiber packing and thermal residual stresses can have a significant effect on the stress-strain

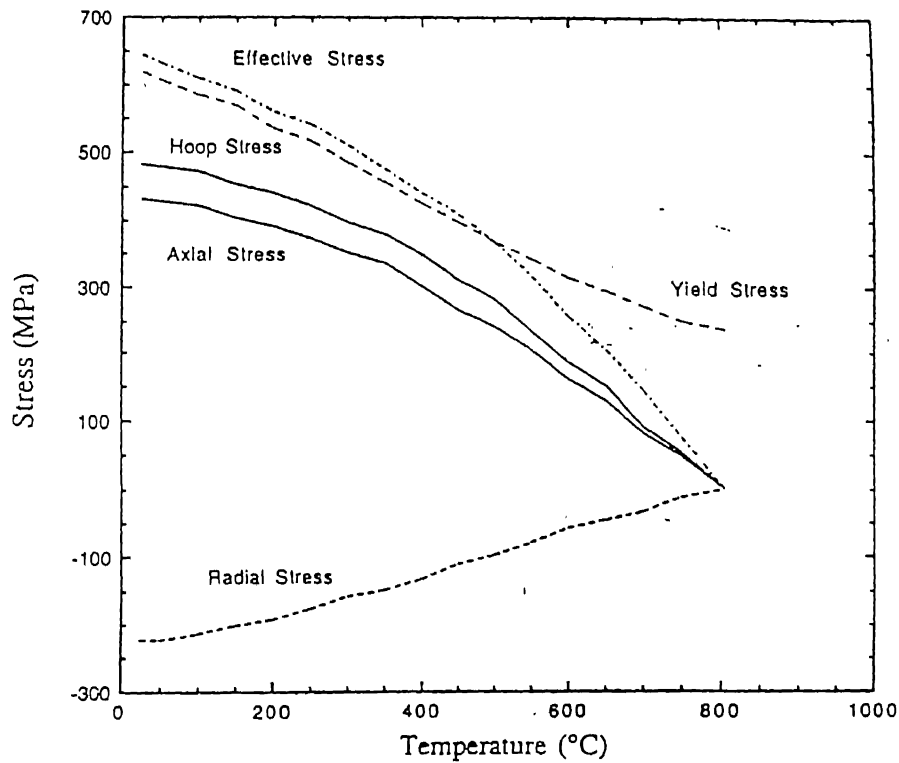


Figure 2.3 - Estimated residual stresses induced in the Ti-14Al-21Nb matrix reinforced with 35% SCS-6 fibers cool down from the strain-free temperature (806° C) to room temperature [27].

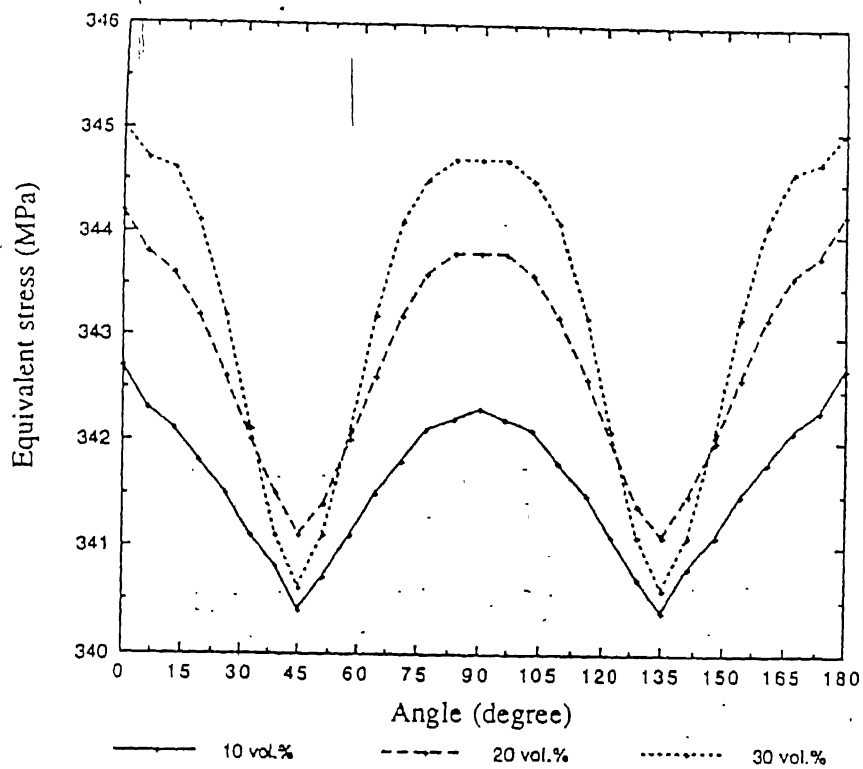


Figure 2.4 - Equivalent stress in the A357.0 matrix around SiC fiber at the fiber/matrix interface (air cooling: temperature of air is 27⁰ C) [19].

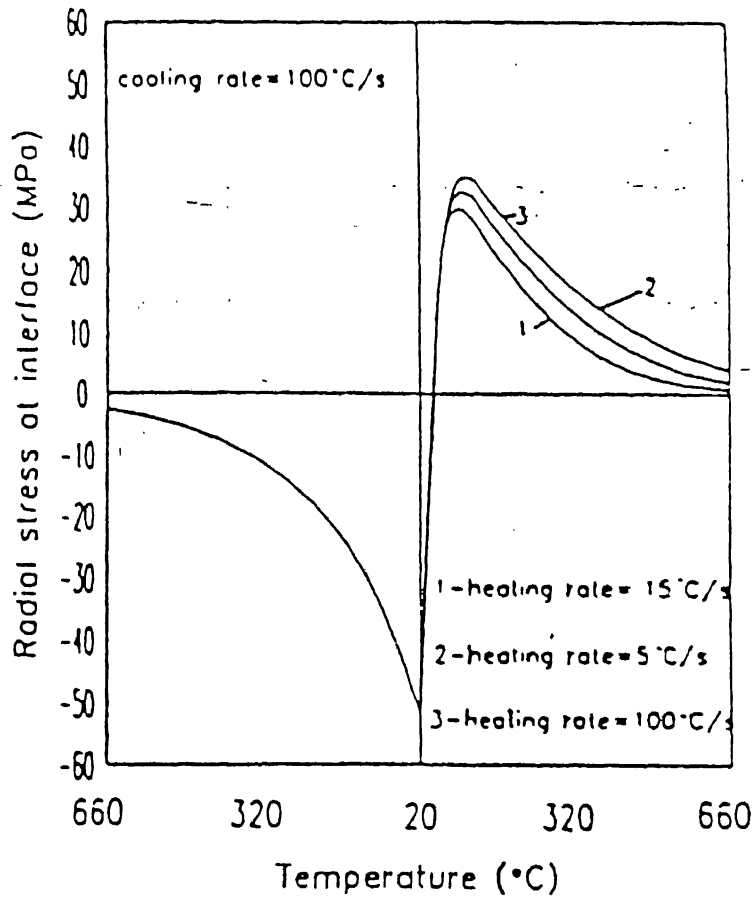


Figure 2.5 - Radial stress at the interface as a function of temperature during cooling to room temperature at K/s and subsequent heating at various rates [26].

characteristics of the composite. The thermal residual stresses cause pronounced matrix yielding which also influences the apparent overall stiffness of the composite during the initial stages of subsequent far-field loading along the axial and the transverse [21].

Thermal residual stresses developed during casting of SiC/aluminum particulate-reinforced composites were investigated by S.Ho and A.Saigal as a function of cooling rate and volume fraction of particles using thermo-elastoplastic finite element method [22].

It was found that the matrix undergoes significant plastic deformation during cool down and has higher residual stress distribution as the cooling rate increases. The presence of thermally induced residual stresses tends to decrease the apparent modulus of elasticity and increase the yield strength of the composite compared to those without residual stresses [22].

2.3 Brief Introduction Of Finite Element Method (FEM) And Its Application

Finite Element Method (FEM) is a powerful tool for the approximate solution of differential equations governing diverse physical phenomena . Its use in industry & research is extensive, indeed it could be said that without it many problems would be incapable of solution [35]. This method is normally applied when conventional method fails. Finite Element methods originated in the field of structural analysis, and many of the early applications were in civil and aeronautical engineering. Methods have also been developed for all types of two- and three-dimensional solid mechanics and recently have been extended into fluid mechanics, composites and heat transfer fields [34].

All finite element methods involve dividing the physical system, such as engineering component or structure, into small sub-regions or elements. Each element is an essentially simple unit, the behaviour of which can be readily analysed. The complexities of the overall system are accommodated by using large number of elements. In the case of a pin-jointed structure, for example, the choice of elements is clear; each

member of the structure is treated as an element, subject only to a tensile and compressive force. From simple analyses of the stiffness of the individual elements, it is possible to establish the behaviour of the overall structure in terms of, say, the displacement responses to externally applied loads. These loads are often applied at the joints of the structure, and it is convenient to consider the displacements at the same points, which are usually referred to as *nodes* or *nodal points* [35].

Frameworks in which relative rotations of the elements at the joints are restricted can be treated in a similar fashion except that, in addition to forces and linear displacements, bending moments and rotations must also be considered. When attention is extended to structure involving plates and shells, however, the choice of elements is less obvious; the continuous surfaces must be sub-divided. Nevertheless, once the elements have been chosen, the behaviour of each can be analysed in terms of displacement response to applied forces and moments, the variables being referred to the nodal points at which the elements are effectively connected together. Similar remarks concerning the choice of elements and the significance of nodal points can also be made in connection with other two- and three-dimensional solid continuum problems[34].

At first sight, some finite element methods may appear to be fundamentally different from analytical and finite difference methods in that they do not use the governing differential equations explicitly. They are, however, based on the physical principles of equilibrium, compatibility and constitutive relationships used to derive the differential equations.

2.4 Helmholtz Free Energy

There are four types of thermodynamic potentials but Gibbs energy (free enthalpy) and Helmholtz free energy are the most important. The free energy Ψ is the portion of the internal energy available for doing work at constant temperature. The enthalpy h as defined here is the portion of the internal energy that can be released as heat when thermodynamic tensions are held constant. The internal energy density u is a potential for the thermodynamic in an isentropic process ($s = \text{const.}$), while the

Helmholtz free energy density calculates potential for temperature and equation is given in terms of strain and temperature:-

$$\Psi = \mu \varepsilon_{ij} \varepsilon_{ji} + \frac{1}{2} \lambda e^2 - (3\lambda + 2\mu) \Delta T \alpha . e \quad 2.7$$

$$\text{where } e = \varepsilon_{rr} + \varepsilon_{\theta\theta} + \varepsilon_{\phi\phi} \quad \text{for polar coordinates.} \quad 2.8$$

$$\text{where } e = \varepsilon_{xx} + \varepsilon_{yy} + \varepsilon_{zz} \quad \text{for cartesian coordinates.} \quad 2.9$$

Chapter 3

SPHERICAL PRECIPITATES

In the first model that is considered for evaluating stresses and strains in the Pd- Al_2O_3 composite, the spherical Al_2O_3 precipitate is embedded in infinite spherical Pd matrix. It is cooled from high temperature to room temperature, pure elastic case is considered for simplification. This method was developed by Lee [2] and is popularly known as Lee model. It is necessary to consider assumptions before evaluating any mathematical model. Assumptions are basically the special cases which help to simply the mathematical model.

A numbers of assumptions are made to evaluate this model [2]. The reinforcement Al_2O_3 ceramic precipitate is considered as a sphere in an infinite matrix of metal-matrix composite (MMC). The matrix behaviour is elastic in nature . The stress-strain behaviour is independent of strain-rate and stress oriented. The temperature in MMC is uniform at all times in all directions. Matrix containing spherical Al_2O_3 precipitate is shown at Figure 3.1. For mathematical simplification, we assume that all other ceramic precipitates are of spherical shape with radius a , and further, that a given particle is surrounded by uniformly distributed neighbouring particles [2].

This assumption allows us to use spherical coordinates (r , θ and ϕ) whose origin is at the center of a ceramic particle with radial symmetry as shown in Figure 3.1.

3.1 Formulation Of Basic Equations

Consider a thick hollow sphere whose internal surface of radius a contains ceramic particle and outer surface contains matrix as shown in figure 3.1. Because of the radial symmetry approximation, the tangential displacements as well as the shear stresses are all zero [2]. The radial displacements u is a function of radial distance r . Further, the force balance in r direction in the absence of body forces leads to the following equilibrium equations.

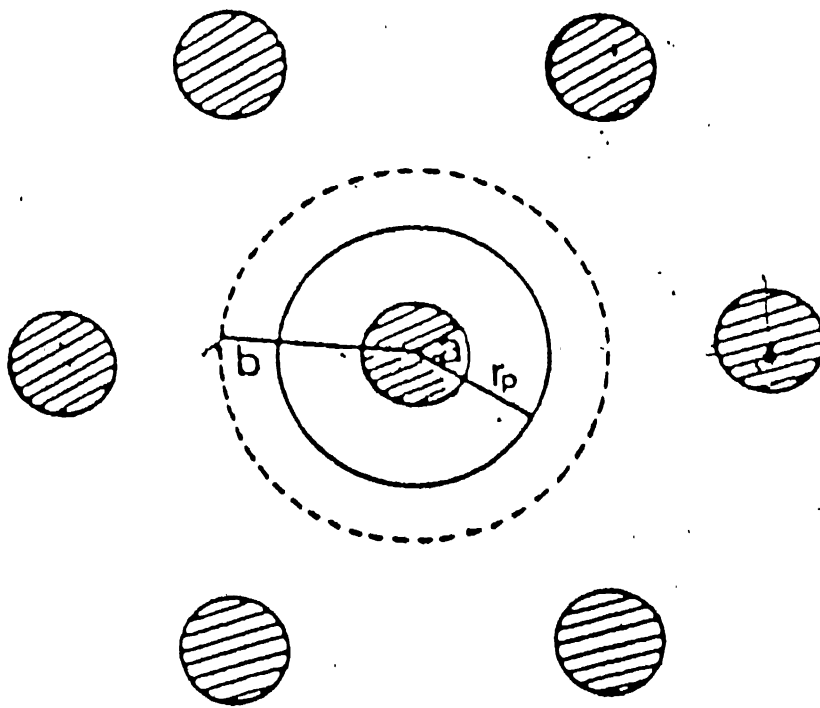


Figure 3.1 – A schematic diagram for an idealized ceramic configuration in Infinite spherical matrix.

$$\frac{d\sigma_r}{dr} + \frac{2(\sigma_r - \sigma_\theta)}{r} = 0 \quad 3.1$$

where σ_r is radial stress and σ_θ is tangential stress

The radial and tangential strains are defined as follows

$$\varepsilon_r = \frac{du}{dr} \text{ (radial strain)} \quad 3.2$$

$$\varepsilon_\theta = \frac{u}{r} \text{ (tangential strain)} \quad 3.3$$

Assumption is made that the stress and strain in third direction (ϕ) is equal to stress and strain in tangential (θ) direction. So the stress and strain in 3rd direction is given by

$$\sigma_\theta = \sigma_\phi \quad \text{and} \quad \varepsilon_\theta = \varepsilon_\phi$$

Under these conditions the necessary stress-strain temperature relations are

$$\varepsilon_r = \frac{1}{E}(\sigma_r - 2\nu\sigma_\theta) + \alpha\Delta T \quad 3.4$$

$$\varepsilon_\theta = \frac{1}{E}[-\nu\sigma_r + (1-\nu)\sigma_\theta] + \alpha\Delta T \quad 3.5$$

where E = Young's modulus of particle.

ν = Poisson's ratio of particle.

α = Coefficient of thermal expansion of particle.

ΔT = Temperature difference between high temperature and room temperature.

Equations 3.4 and 3.5 can be inverted to give the radial and tangential stress in terms of the strains and the temperature.

$$\begin{Bmatrix} \sigma_r \\ \sigma_\theta \sqrt{2} \end{Bmatrix} = \frac{E}{(1+\nu)(1-2\nu)} \begin{bmatrix} 1-\nu & \nu\sqrt{2} \\ \nu\sqrt{2} & 1 \end{bmatrix} \begin{Bmatrix} \varepsilon_r \\ \varepsilon_\theta \sqrt{2} \end{Bmatrix} - \frac{E\alpha\Delta T}{(1+\nu)(1-2\nu)} \begin{bmatrix} 1-\nu & \nu\sqrt{2} \\ \nu\sqrt{2} & 1 \end{bmatrix} \begin{Bmatrix} 1 \\ \sqrt{2} \end{Bmatrix}$$

$$\{\sigma\} = [D]_e \{\varepsilon\} - [D]_{th} \begin{Bmatrix} 1 \\ \sqrt{2} \end{Bmatrix} \quad 3.6$$

$$[D]_e = \frac{E}{(1+\nu)(1-2\nu)} \begin{bmatrix} 1-\nu & \nu\sqrt{2} \\ \nu\sqrt{2} & 1 \end{bmatrix}$$

where $[D]_e$ is known as the elastic property matrix which is a symmetric matrix.

Where $[D]_{Th} = [D]_e \alpha \cdot \Delta T$ is known as the thermal property matrix which is a symmetric matrix.

3.2 Variational FEM Method

An alternative, although entirely equivalent, approach to that of solving the governing differential equation is the variational method which seeks to solve a problem by finding the conditions for a stationary value (either a maximum or a minimum) of some quantity with respect to the unknowns of the problem [23]. This quantity, which is often referred to as a functional, generally involves an appropriate integral of the unknowns or derivatives of the unknowns over the region of interest, which in engineering elasticity problems is the component or structure concerned. Variational formulations for elasticity problems can be developed from either the governing differential equations or an equivalent physical principle, such as an energy minimization [23]. Here the first approach is followed. The equilibrium equation (3.1) leads to

$$\begin{aligned} \int_0^a \left(\frac{d\sigma_r}{dr} + \frac{2(\sigma_r - \sigma_\theta)}{r} \right) \delta u \cdot 4\pi r^2 \cdot dr &= 0 \\ \int_0^a \left(\frac{d\sigma_r}{dr} + \frac{2\sigma_r}{r} - \frac{2\sigma_\theta}{r} \right) \delta u \cdot 4\pi r^2 \cdot dr &= 0 \end{aligned} \quad 3.7$$

After integration by parts, the matrix form of this equation becomes

$$\int_0^a r^2 (\sigma_r - \sigma_\theta \sqrt{2}) \delta \left\{ \frac{\partial u}{\partial r} \right\} \frac{dr}{\sqrt{2}u} = 0 \quad 3.8$$

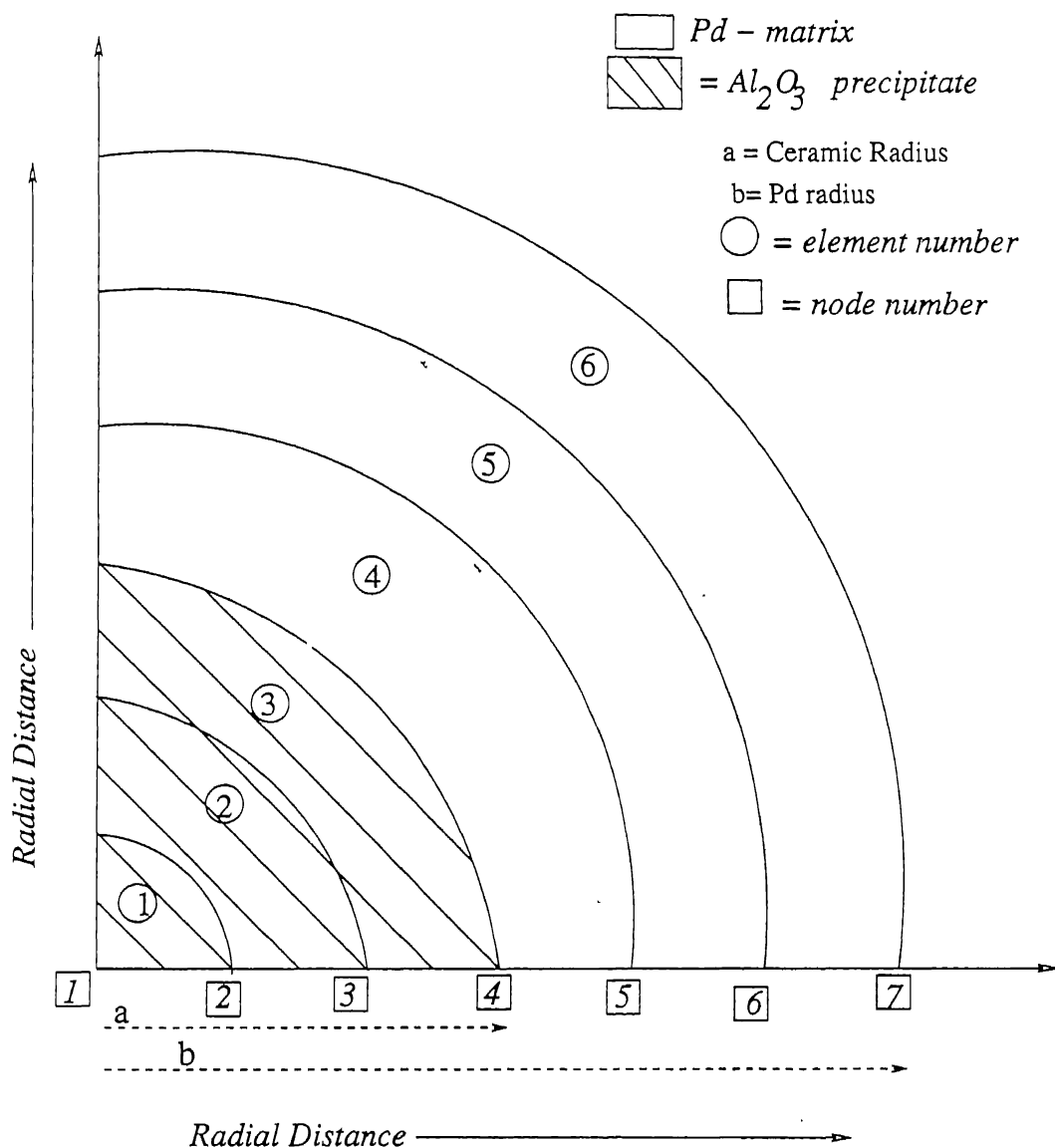


Figure 3.2 -- The discretization of the domain for the case where Al_2O_3 precipitate is inside the composite.

Substitution of equations (3.6), (3.2) and (3.3) and use of properties of variational operator leads to the following equations

$$\text{We get } \delta I = 0 \quad 3.9$$

$$\text{where } I = \int_0^r \left[\frac{1}{2} r^2 \{\varepsilon\}^T [D]_e \{\varepsilon\} - r^2 [D]_{th} \{\varepsilon\} \right] dr \quad 3.10$$

where I is the variational functional of the problem..

3.2.1 Shape Functions

The variation of the dependent variable over each element is often expressed in terms of the variable at certain points called as nodes and the known functions are called shape functions. The discretization of the domain of the composites shown on Figure 3.2. In the present case a simple approximation consisting of 2 nodes and linear shape functions is used :

$$\begin{array}{ccc} & e & \\ 1 & \text{-----} & 2 \\ u_1^e & & u_2^e \end{array}$$

simple element for evaluations of shape functions

$$u = N_1^e u_1^e + N_2^e u_2^e = \{N\}^e \{u\}^e \quad 3.11$$

where u is the displacement term with respect of shape functions $\{N\}^e$ and elemental displacement $\{u\}^e$.

$$\text{where } N_1^e = \frac{r - r_2^e}{r_1^e - r_2^e} \text{ and } N_2^e = \frac{r - r_1^e}{r_2^e - r_1^e} \quad 3.12$$

The derivatives of shape functions with respect to r are given by

$$\frac{dN_1^e}{dr} = \frac{1}{r_1^e - r_2^e} \quad \text{and} \quad \frac{dN_2^e}{dr} = \frac{1}{r_2^e - r_1^e} \quad 3.13$$

Radial strain in terms of derivatives of shape functions and displacements is given by

$$\frac{du}{dr} = \left\{ \frac{dN}{dr} \right\}^e \{u\}^e \quad 3.14$$

Strain vector terms of displacements and shape functions from equations (3.11) and (3.14) is given by

$$\{\varepsilon\} = \left\{ \begin{matrix} \varepsilon_{rr} \\ \sqrt{2} \varepsilon_{\theta\theta} \end{matrix} \right\} = \left\{ \begin{matrix} \partial u / \partial r \\ \sqrt{2} u / r \end{matrix} \right\} = \begin{bmatrix} \partial N_1 / \partial r & \partial N_2 / \partial r \\ \sqrt{2} N_1 / r & \sqrt{2} N_2 / r \end{bmatrix} \begin{Bmatrix} u_1 \\ u_2 \end{Bmatrix} = \{B\}^e \{\delta\}^e \quad 3.15$$

Here, $\{\delta\}^e$ is the elemental displacement vector containing the radial displacement at each node, substitution of equation 3.15 in the expression for I leads to

$$I = \sum_{e=1}^{n_e} \frac{1}{2} \left[\{\delta\}^{eT} [K]^e \{\delta\}^e - \{\delta\}^{eT} \{f\}^e \right] \quad 3.16$$

$$[K]^e = \int_{r_1^e}^{r_2^e} r^2 \{B\}^{eT} [D]_e \{B\}^e .dr \quad 3.17$$

where $[k]^e$ is the elemental coefficient matrix and is obtained from the 1st integral of equation 3.16.

$$\{f\}^e = \int_{r_1^e}^{r_2^e} r^2 \{T\}^T [D]_{Th} \{B\} .dr \quad 3.18$$

where $\{f\}^e$ is the elemental right side vector containing the thermal residual stress term.

The elemental displacement vector $\{\delta\}^e$ is related to the global displacement vector $\{\Delta\}$ by the following relations

$$\{\delta\}^e = [A]^e \{\Delta\} \quad 3.19$$

where the matrix $[A]^e$ depends on the elemental (i.e. local node) and global node numbering systems. Substitution of equations 3.19 and 3.14 gives

$$I = \sum_{e=1}^{n_e} \frac{1}{2} \left[\{\Delta\}^T [K]^e \{\Delta\} - \{\Delta\}^T \{F_{Th}\}^e \right] \quad 3.20$$

$$[K] = \sum_{e=1}^{n_e} [A]^eT [K]^e [A]^e \quad \text{where } [K] \text{ is the global coefficient matrix.} \quad 3.21$$

$$\{F_{Th}\} = \sum_{e=1}^{n_e} [A]^e \{F\}^e \quad \text{where } \{F_{Th}\} \text{ is the global right side vector.} \quad 3.22$$

Equation 3.20 leads to

$$I = \frac{1}{2} \{\Delta\}^T [K] \{\Delta\} - \{F\} \{\Delta\}$$

Extremization of I leads to

$$\boxed{[K] \{\Delta\} = \{F_{Th}\}} \quad 3.23$$

Solving of the above equations gives displacements at all the nodes.

Data for FEM Formulation

Composite consists of two materials, Palladium (Pd) is the matrix and alumina (Al_2O_3) is the ceramic precipitate & their material properties is given below in table 3.1.

Criteria	Material Properties of Pd-matrix	Material Properties of Al_2O_3 Ceramic particle
Poisson's Ratio (ν)	0.375	0.25
Young Modulus (E)	$123 * 10^9$ Pascal(N/m^2)	$380 * 10^9$ Pascal(N/m^2)
Coefficient of thermal Expansion(CTEs)	$11.5 * 10^{-6}/K$	$8.0 * 10^{-6}/K$

Table 3.1 - Material properties of composite.

Calculation of [D] and {T} matrices

For these materials, the matrices appearing in equation (3.6) are as follows :

For Pd-matrix

$$[D]_{mat} = \frac{4E_{mat}}{11} \begin{bmatrix} 5 & 3\sqrt{2} \\ 3\sqrt{2} & 8 \end{bmatrix} \quad [D]_{Th} = 11.5 * 10^{-6} \Delta T [D]_{mat}$$

For Al_2O_3 Ceramic Precipitates

$$[D]_{ppt} = \frac{E_{ppt}}{10} \begin{bmatrix} 12 & 4\sqrt{2} \\ 4\sqrt{2} & 10 \end{bmatrix} \quad [D]_{Th} = 8.0 * 10^{-6} \Delta T [D]_{ppt}$$

3.3 Estimation Of Displacements

Displacement of node can be evaluated by FEM formulation is given by solving equation 3.10 and theoretical displacements is given by

$$u = \alpha r \Delta T \quad 3.24$$

Validation of results is made by using only one type of material, it may be total Al_2O_3 precipitate or may be total Pd-matrix. Exactly same type of results are obtained for both FEM modeling and theoretical equations and it is shown on table 3.1. Two kinds of cases are considered in analyze the FEM formulation result and shown in Figure 3.3. In the first case called IO case where Al_2O_3 ceramic precipitate is inside and Pd matrix is outside. In the second case called OI case where ceramic precipitate is outside and Pd matrix is inside.

Thermal residual stresses occur due to temperature difference and the temperature difference is kept at 1000K at both the above cases to obtain the various results. Figure 3.4 shows the displacement for the composite as a function of radial distance. The Pd matrix has higher displacement because its coefficient of thermal expansion ($\alpha_m = 11.5 \times 10^{-6}/\text{K}$) is higher than that of Al_2O_3 ceramic precipitate ($\alpha_c = 8.0 \times 10^{-6}/\text{K}$). The change of slope at the interface occur due to the presence of Al_2O_3 and Pd matrix at the interface. IO and OI case are taken from the Figure 3.3.

3.4 Estimation Of Strains

Radial and tangential strains are calculated from equation 3.15 .

Where ϵ_r is the strain at each element at radial direction and $\epsilon_{\theta\theta}$ is the strain at each element at the tangential direction.

Figure 3.5 shows the variation of radial strain for $\Delta T = 1000\text{K}$ for IO and OI cases. The figure shows the radial strain is higher for Pd matrix ($\alpha_m = 11.5 \times 10^{-6}/\text{K}$) then that of Al_2O_3 precipitate ($\alpha_c = 8.0 \times 10^{-6}/\text{K}$). No temperature changes occur within

Radial Dist. In Mts.	FEM Calculation	Theoretical Calculation	FEM Calculation	Theoretical Calculation
Total Pd Matrix			Total Ceramic Particle	
0	0	0	0	0
0.001	1.15E-05	1.15E-05	8.00E-06	8.00E-06
0.002	2.30E-05	2.30E-05	1.60E-05	1.60E-05
0.003	3.45E-05	3.45E-05	2.40E-05	2.40E-05
0.004	4.60E-05	4.60E-05	3.20E-05	3.20E-05
0.005	5.75E-05	5.75E-05	4.00E-05	4.00E-05
0.006	6.90E-05	6.90E-05	4.80E-05	4.80E-05
0.007	8.05E-05	8.05E-05	5.60E-05	5.60E-05
0.008	9.20E-05	9.20E-05	6.40E-05	6.40E-05
0.009	0.0001035	0.0001035	7.20E-05	7.20E-05
0.01	0.000115	0.000115	8.00E-05	8.00E-05

Table 3.2 -- Validation of results with theoretical and FEM results.

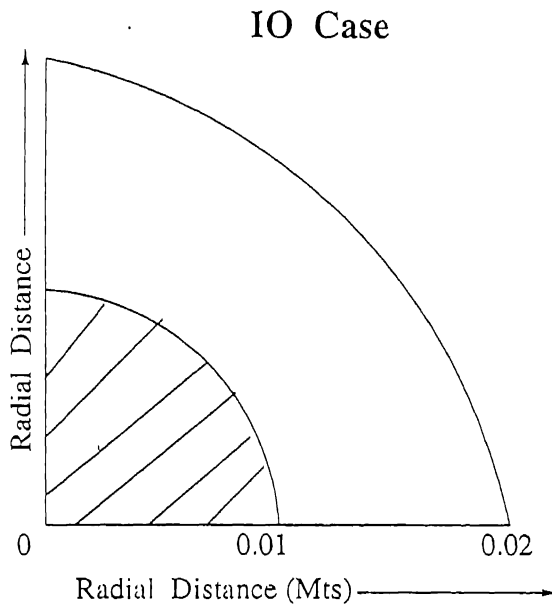


Figure 3.3.a
Ceramic ppt. is inside and
Pd is outside at $\Delta T=1000K$
(ceramic volume
fraction = 0.125)

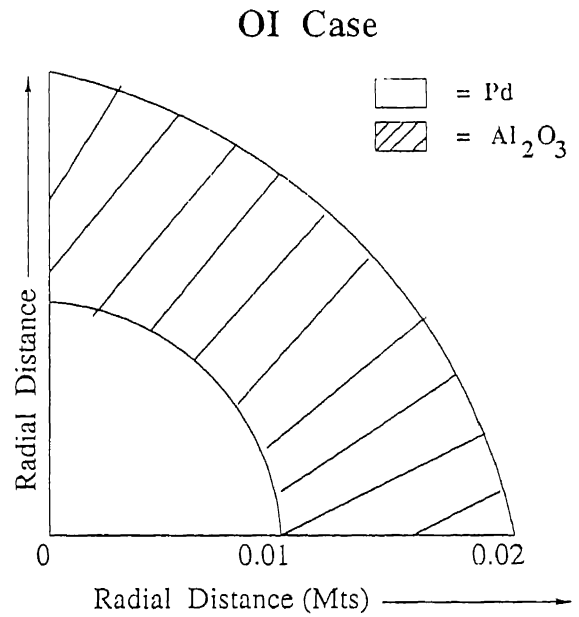


Figure 3.3.b
Ceramic ppt. is outside and
Pd is inside at $\Delta T=1000K$
(ceramic volume
fraction = 0.875)

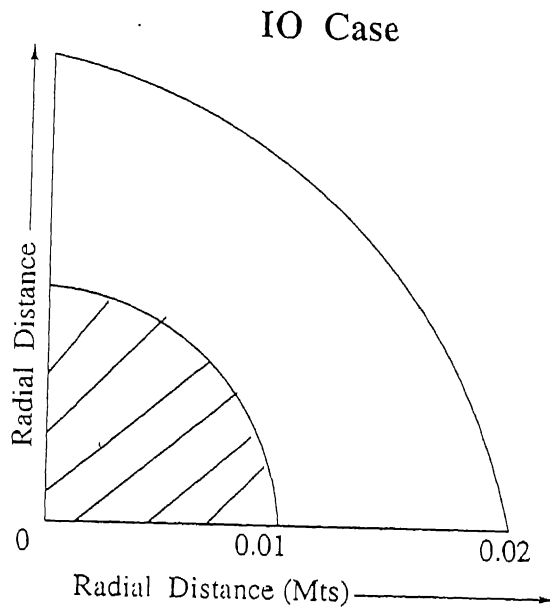


Figure 3.3.a
Ceramic ppt. is inside and
Pd is outside at $\Delta T=1000K$
(ceramic volume
fraction = 0.125)

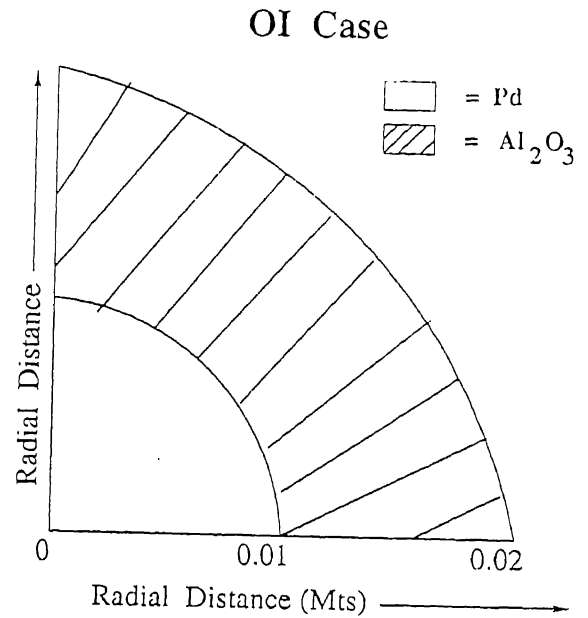


Figure 3.3.b
Ceramic ppt. is outside and
Pd is inside at $\Delta T=1000K$
(ceramic volume
fraction = 0.875)

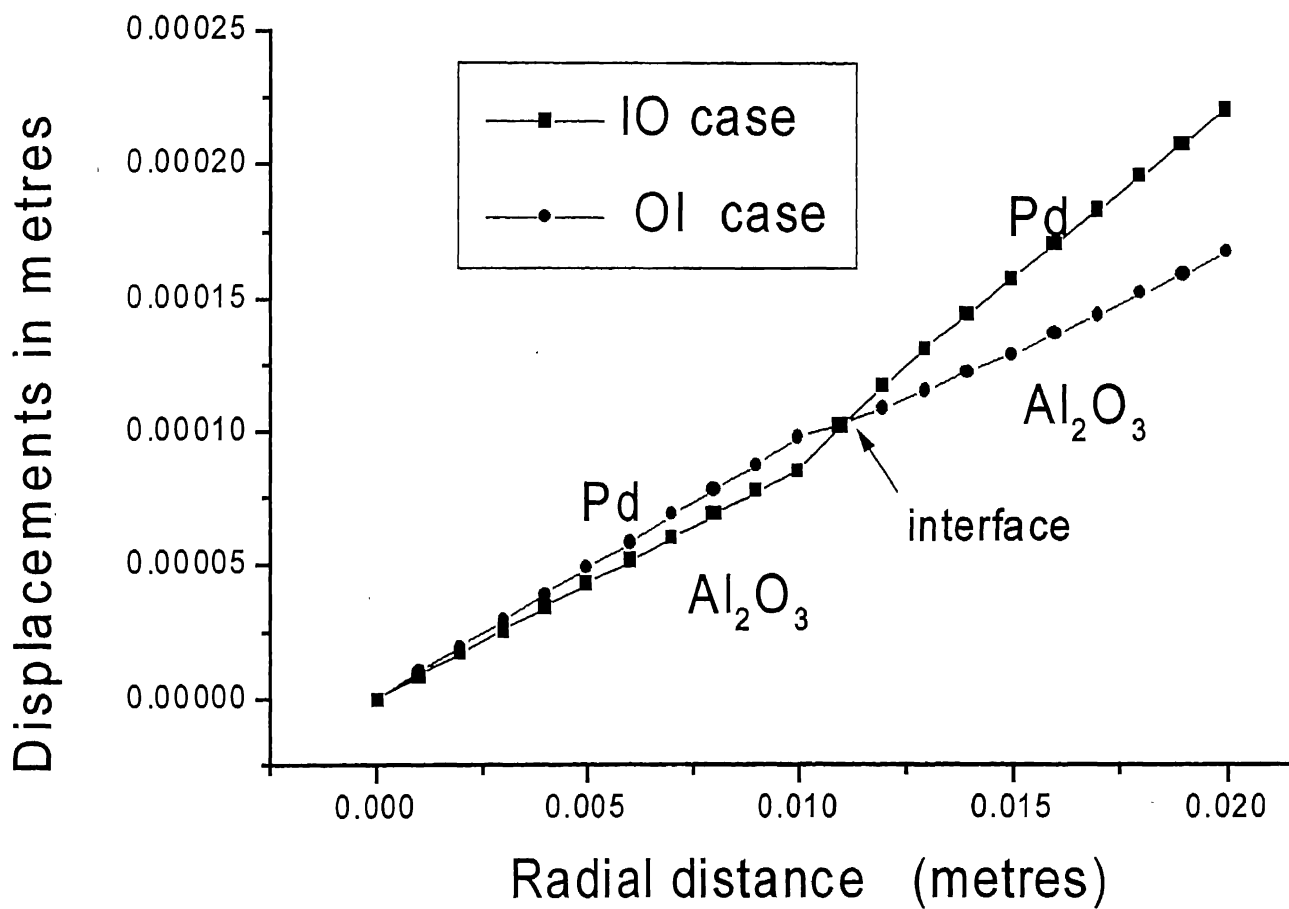


Figure 3.4 -- Variation of displacements as a function of radial distance at $\Delta T = 1000\text{K}$ for IO and OI cases.

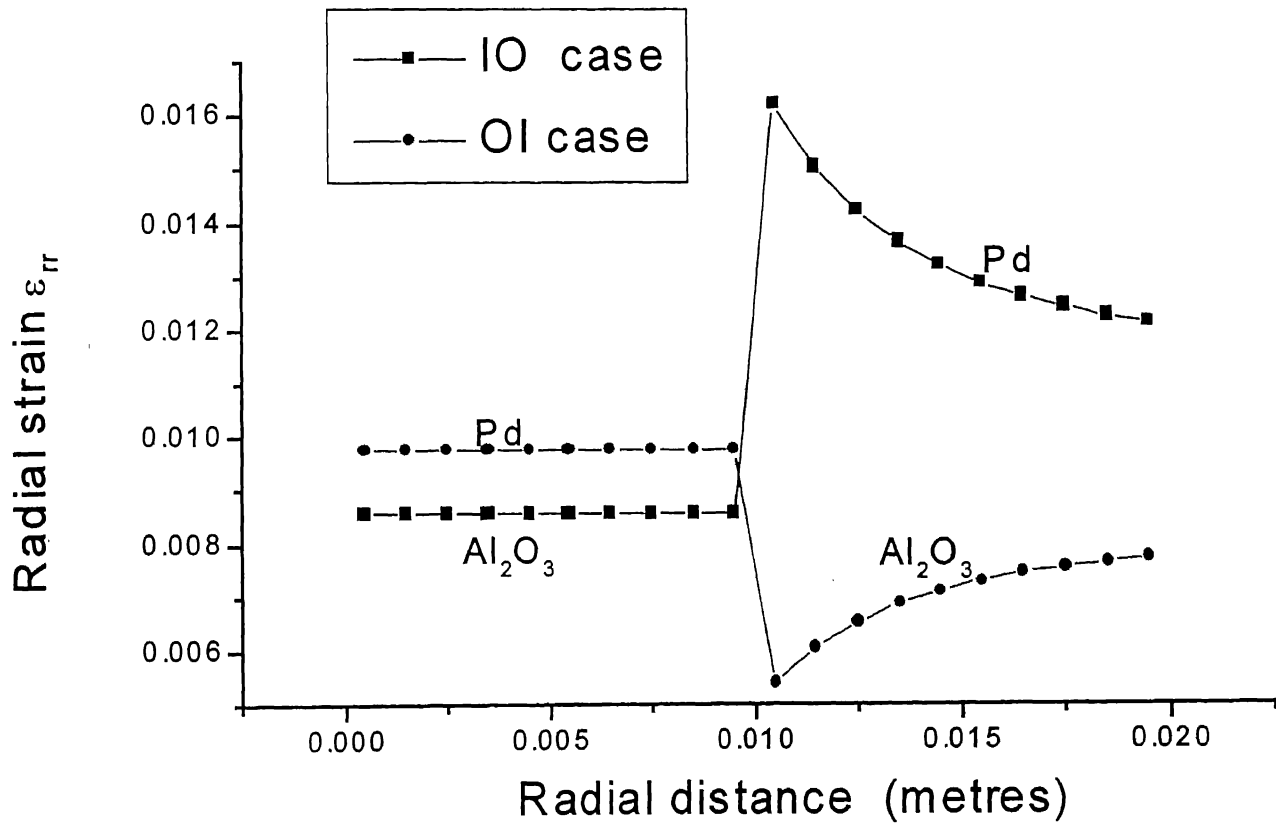


Figure 3.5 -- Variation of Radial strain (ϵ_{rr}) as a function of radial distance at $\Delta T = 1000\text{K}$ for IO and OI cases.

element during FEM modeling. Radial strain at initial part upto interface is influenced by individual part and temperature plays no part in influencing radial strain. That's why radial strains remain parallel to x-axis for initial part. At the junction of interface, slope of radial strains change drastically due to the mismatch of material properties.

Figure 3.6 shows the variation of tangential strain as a function of radial distance $\Delta T = 1000\text{K}$. Pd matrix ($\alpha_m = 11.5 \times 10^{-6}/\text{K}$) has higher strain than Al_2O_3 precipitate ($\alpha_c = 8.0 \times 10^{-6}/\text{K}$) due to higher coefficient thermal expansion of Pd matrix. Slope of strain changes drastically at the interface due to mismatch of material properties of Al_2O_3 precipitate and Pd matrix at interface.

3.5 Estimation Of Stresses

Radial and tangential stresses are calculated from the strain in each element using equation 3.6. The stresses are depending on strains, temperatures and material property of the particles. Radial stress variation as a functions of radial distance at $\Delta T = 1000\text{K}$ is shown at Figure 3.7. The ceramic volume fraction of alumina precipitate is 0.875 for OI where as for IO case is 0.125. The Young's modulus of alumina ($E = 380 \text{ Gpa}$) is more than that of Pd matrix ($E = 123\text{Gpa}$), stress is greatly influence by alumina than Pd matrix and has high negative value for OI case than that of IO case. The IO case radial shown value has less negative value due to less presence of alumina particle in the composite.

The stresses remain constant for initial part as the particle is solely influenced by individual particle change and no temperature changes occur within the composite during FEM formulation. Figure 3.8 shows the variation of tangential stress as a function of radial distance at $\Delta T = 1000\text{K}$. The interesting thing about this graph that stresses in alumina is always positive whereas stress in Pd is always negative. The reason

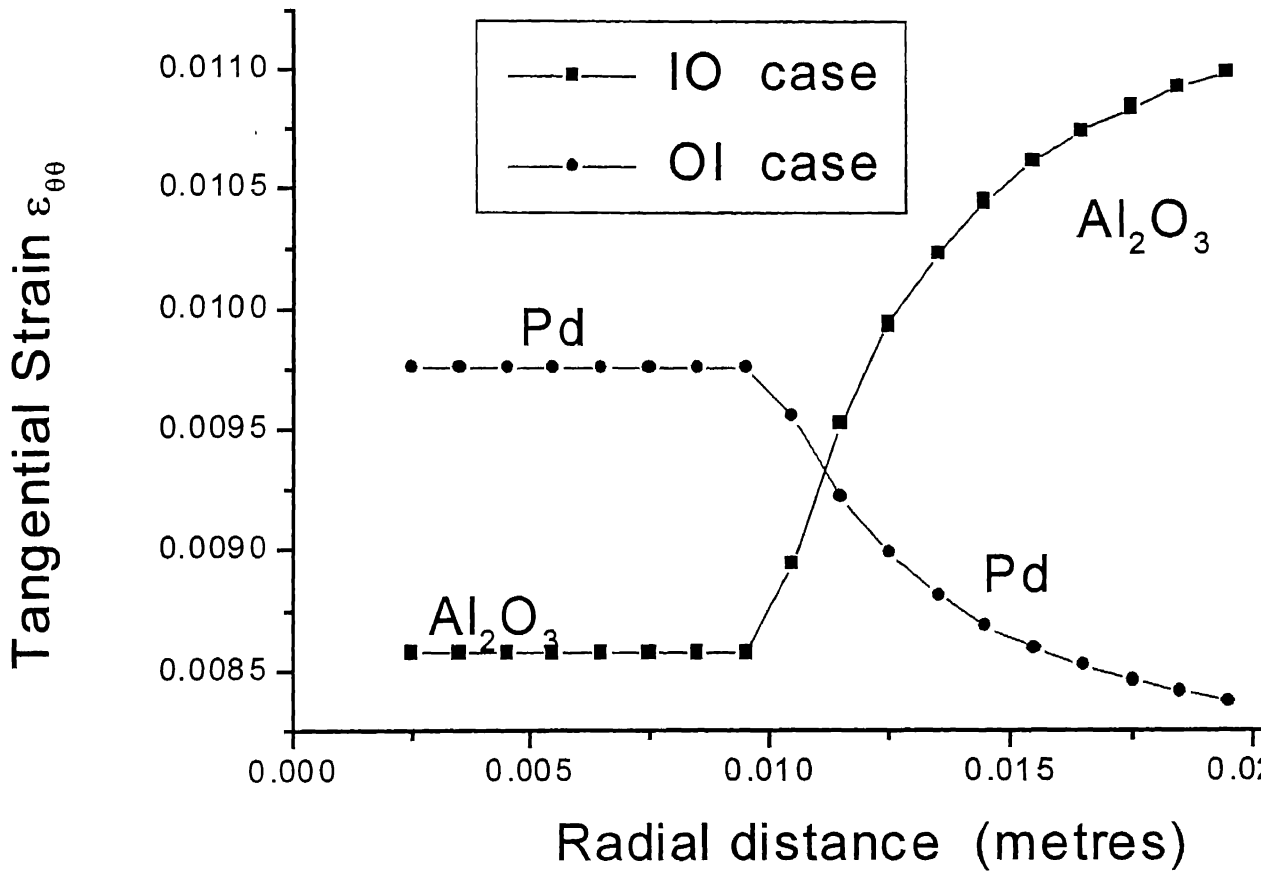


Figure 3.6 -- Variation of tangential strain ($\epsilon_{\theta\theta}$) as a function of radial distance at $\Delta T = 1000K$ for IO and OI cases.

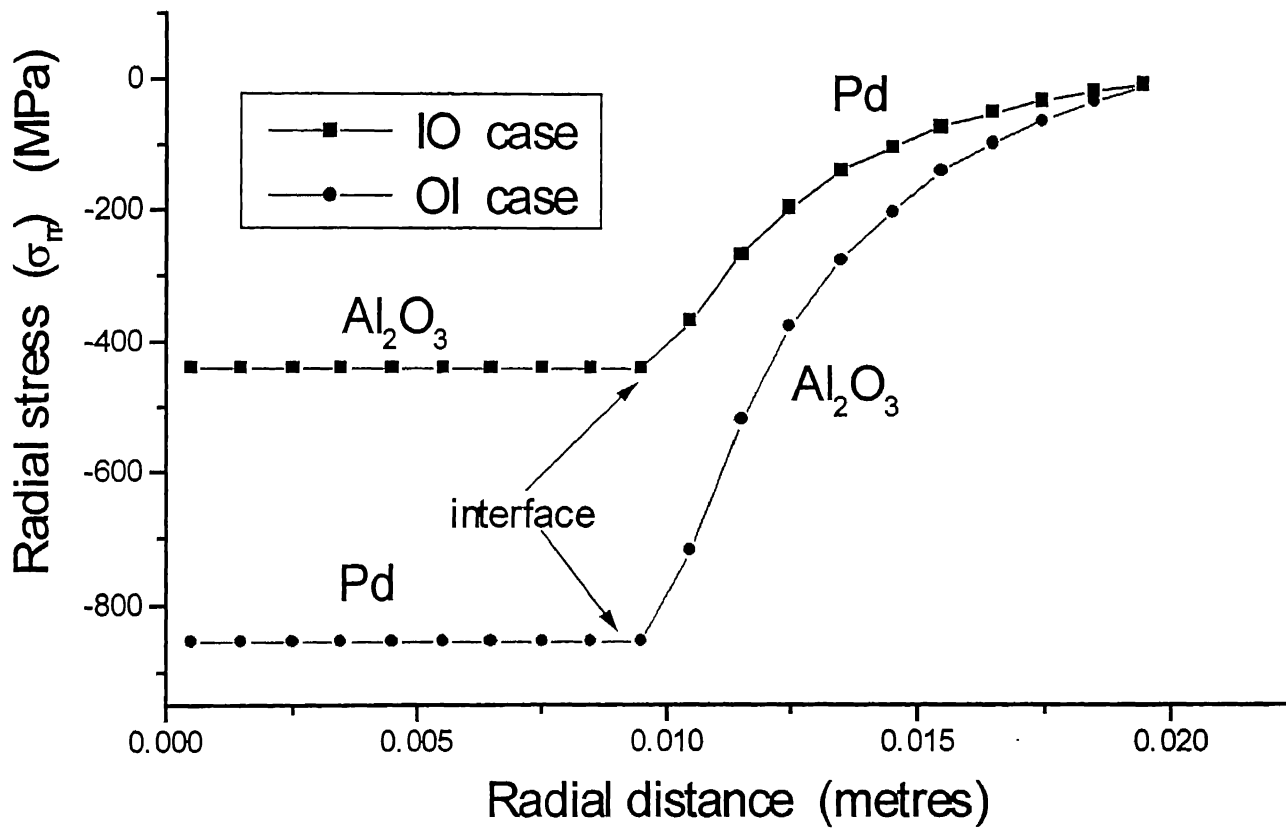


Figure 3.7 -- Variation of radial stress (σ_{rr}) as a function of radial distance at $\Delta T = 1000K$ for IO and OI cases.

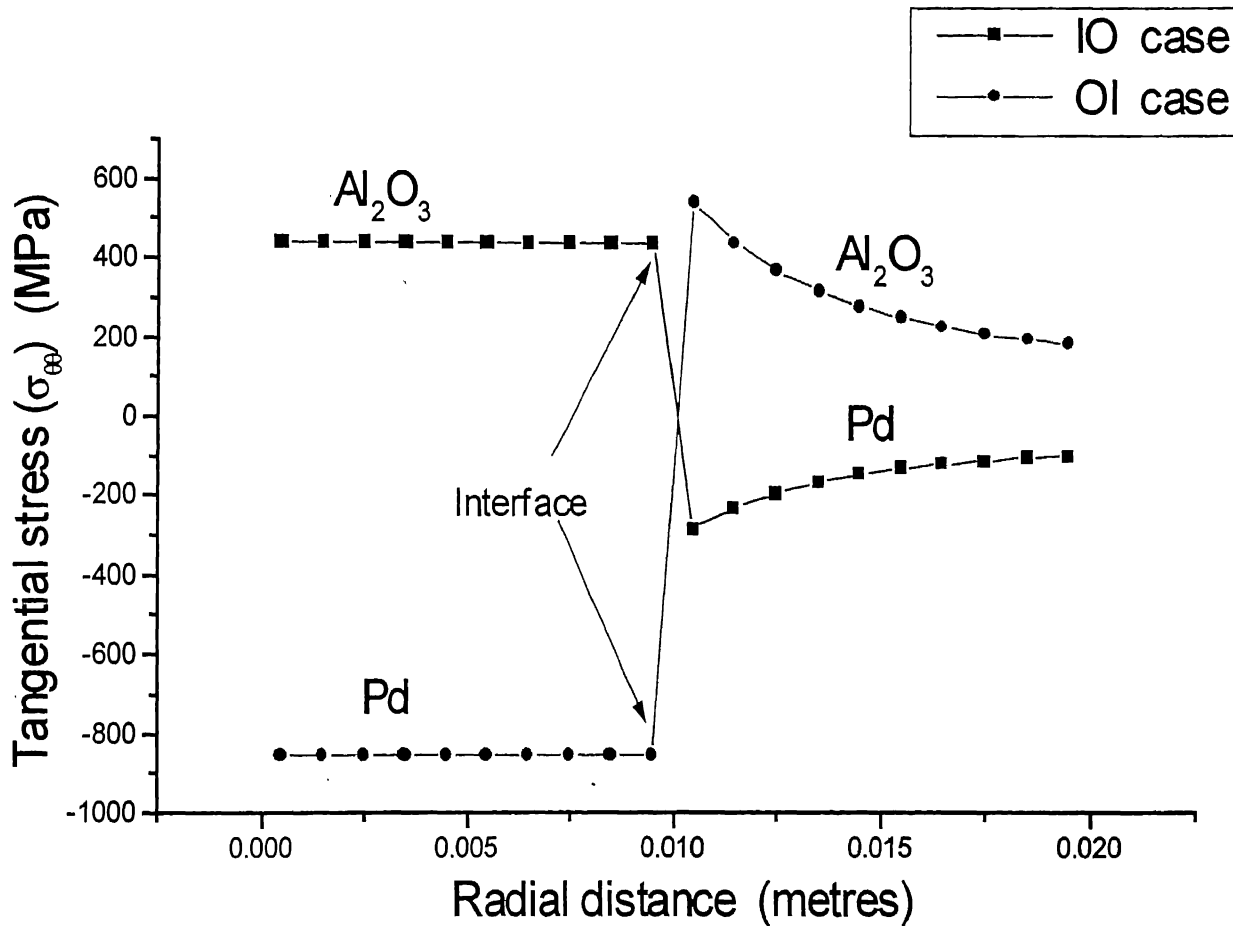


Figure 3.8 -- Variation of tangential stress ($\sigma_{\theta\theta}$) as a function of radial distance at $\Delta T = 1000\text{K}$ for IO and OI cases.

behind this, may be that alumina tangential stress must have tensile stress as it has high Young's modulus value. To compensate the tensile value of alumina precipitate, Pd matrix must have compressive stress due to less Young's modulus value.

3.6 Estimation Of Solubility Enhancement ratio

Hydrogen is only observed by Pd matrix and not by the alumina ceramic precipitate, This property of Pd is used to calculate thermal residual stress. According to Kim et al. model [2], the tensile hydrostatic stress (σ_h^m) developed in the matrix which can be shown to be independent of distance from the precipitate -matrix interface, is given by equation 2.1. The tensile hydrostatic stress (σ_h^m) curve which is estimated from the radial stresses is shown in Figure 3.9, the radial stresses being considered here is not at metal-ceramic interface but over the whole composite. OI case has more negative radial stress, so it has more positive tensile hydrostatic stress curve.

The solubility enhancement (n'/n) ratio can be calculated after having calculation of tensile hydrostatic stress (σ_h^m) and is given by equation (2.5). The solubility enhancement value changes with the changing value of ceramic volume fraction at particular temperature difference. These solubility enhancement values are plotted in Figure 3.10 and Figure 3.11 as a function of alumina volume fraction for different temperature difference for IO and OI respectively. Figure 3.10 shows ratio as one for zero alumina ceramic fraction, ratio goes to maximum with the increase of fraction. Then with the increase of ceramic fraction the ratio decreases slowly and becomes one at 100% ceramic particle. The Figure 3.10 clearly shows the higher temperature difference as higher solubility ratio. Figure 3.11 show solubility enhancement curve for OI case. It starts with value 1 and with the increase of ceramic fraction, ratio goes on increasing.

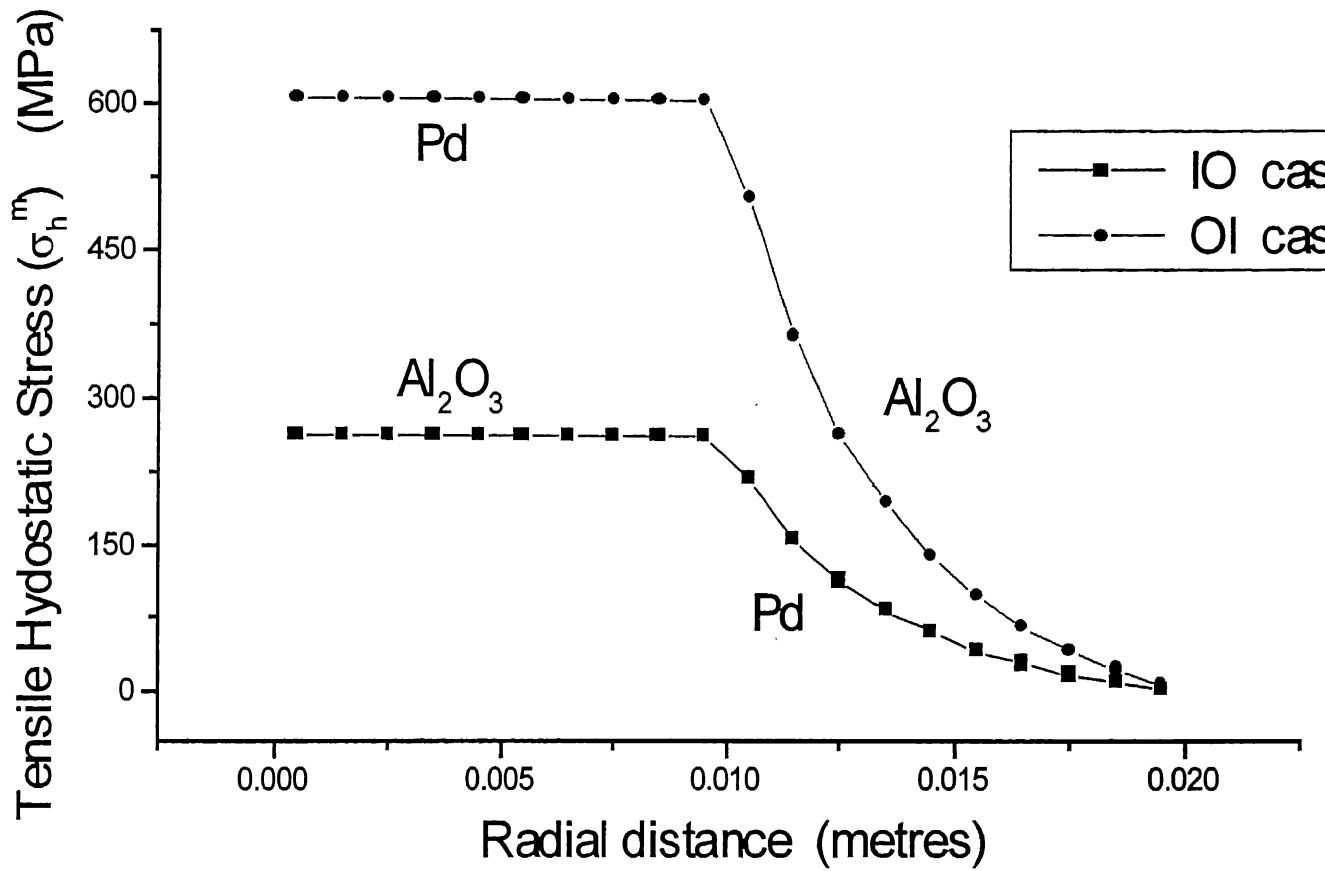


Figure 3.9 -- Variation of Tensile Hydrostatic stress (σ_h^m) of as a function of radial distance at $\Delta T = 1000K$ for IO and OI cases.

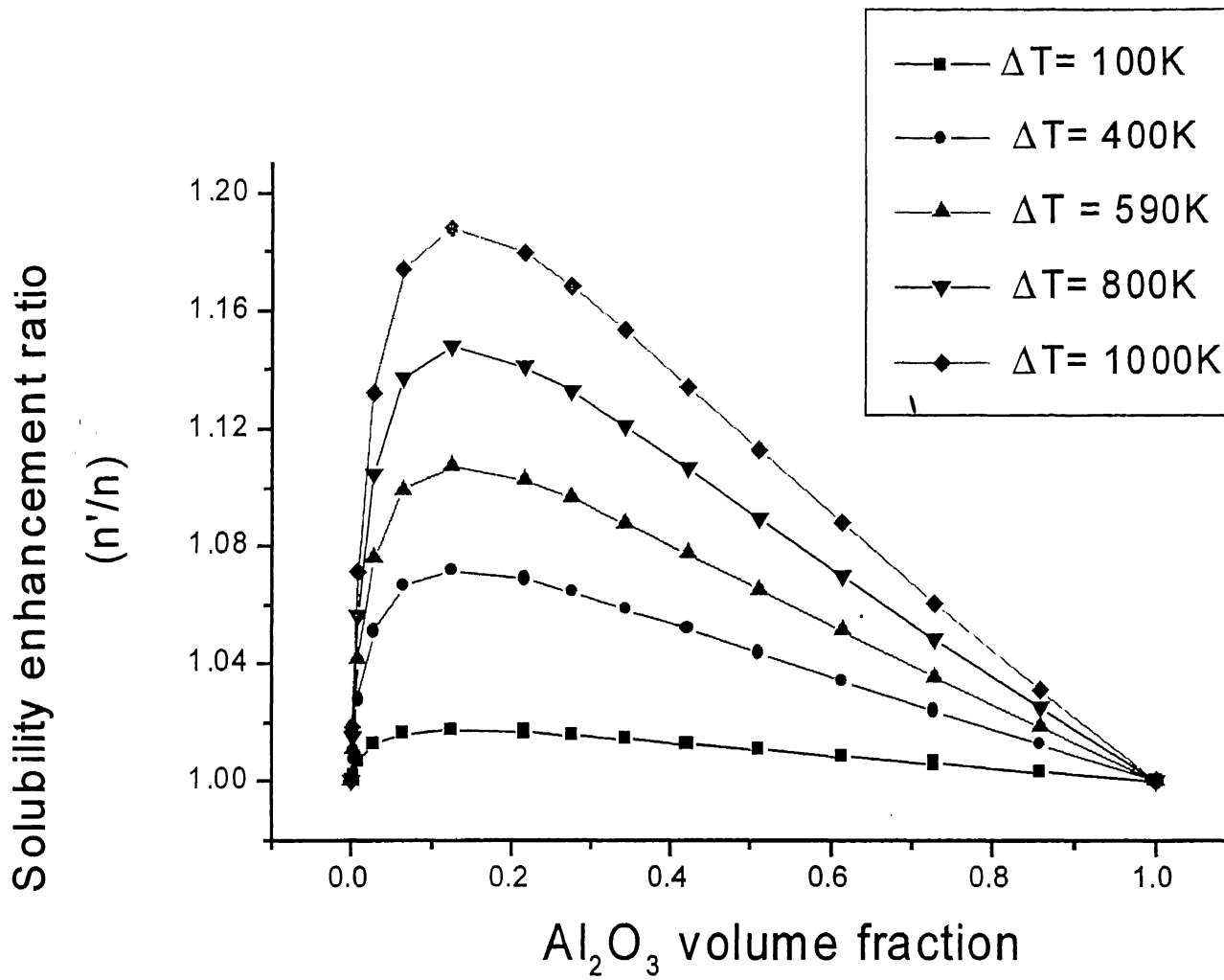


Figure 3.10 -- Variation of solubility enhancement ratio as a function of Al_2O_3 precipitate volume fraction for different temperature difference values for IO case.

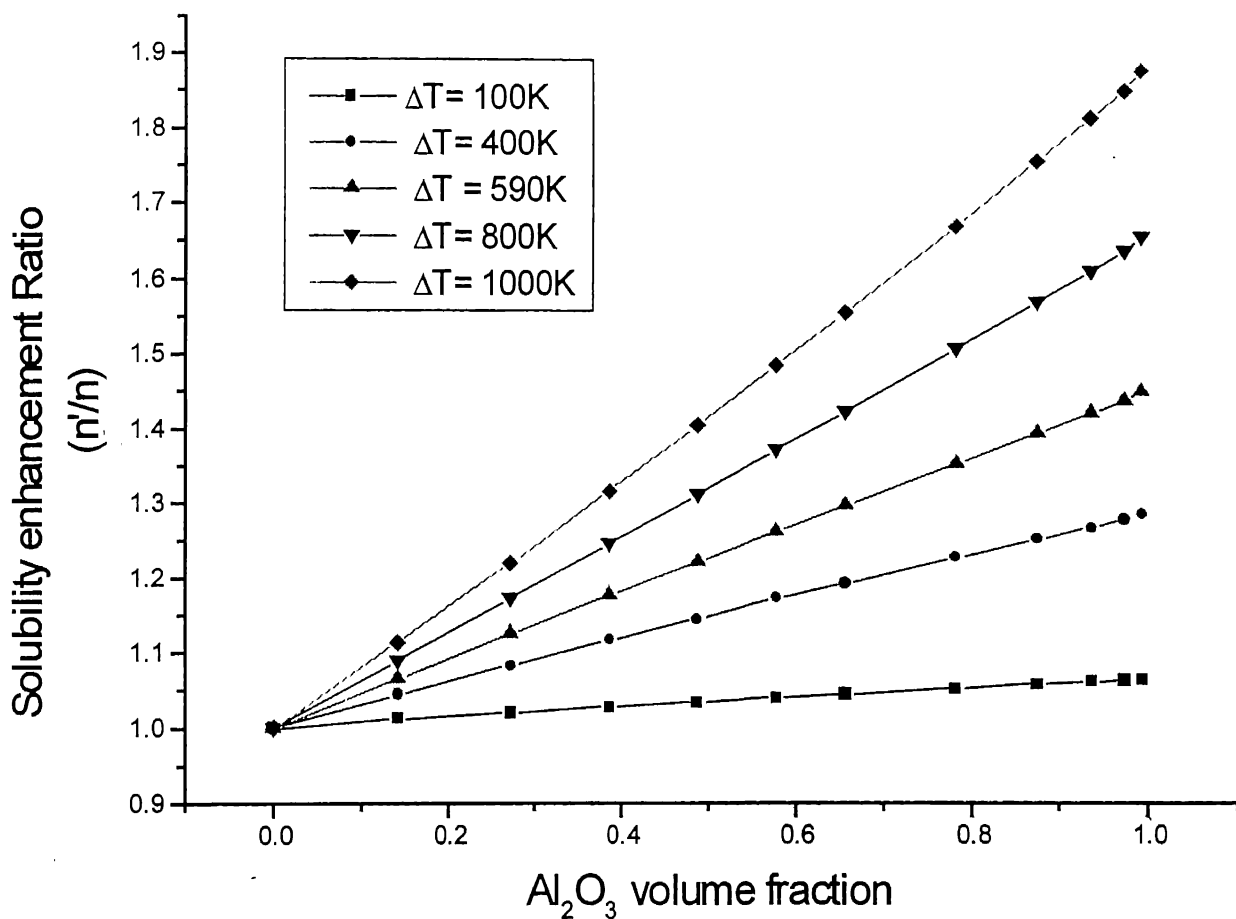


Figure 3.11 -- Variation of solubility enhancement ratio as a function of Al_2O_3 precipitate volume fraction for constant temperature difference for OI case.

3.7 Estimation of Helmholtz Free Energy

Helmholtz free energy density estimated potential of the particle for the temperature changes. Helmholtz free energy per unit volume in polar co-ordinates can be calculated from equation 2.7 as .

$$\psi = \frac{E}{2(1+\nu)}(\epsilon_{rr}^2 + 2\epsilon_{\theta\theta}^2) + \frac{1}{2} \frac{E\nu}{(1+\nu)(1-2\nu)}(\epsilon_{rr} + 2\epsilon_{\theta\theta})^2 - \frac{E}{(1-2\nu)}(\epsilon_{rr} + 2\epsilon_{\theta\theta}) \quad 3.25$$

The Helmholtz free energy over the whole volume is given by

$$\Psi = \int_0^b \psi \cdot 4\pi r^2 dr \quad 3.26$$

Helmholtz free energy (HFE) depends on material properties, temperature changes and strains. Figure 3.12 shows HFE curve as a function of radial distance at $\Delta T = 1000K$. In both cases, energy for Pd matrix is more than alumina precipitate energy obtained by Pd matrix IO case is very much as compared to other energies. At particular ceramic volume fraction, summation of HFE is done for alumina precipitate and also Pd matrix. Total HFE is obtains just by adding total HFE for alumina and Pd matrix.

HFE values changes with the changing value of alumina volume fraction for particular temperature difference. These values of HFE are plotted as a function of ceramic volume fraction for IO and OI case at Figure 3.13 and 3.14 for different temperature difference. The HFE for alumina precipitate is very less as compared to Pd matrix. The Figures 3.13 and 3.14 clearly shows that higher free energies are obtained for higher temperature difference. The alumina precipitate HFE is zero at initial part where Pd matrix HFE has maximum value. Alumina precipitate HFE increases with the increase of ceramic volume fraction and goes to maximum at 100% ceramic volume fraction. Just the opposite case occur for Pd matrix, it has lowest value at 100% ceramic fraction. The HFE is mainly influenced by the Pd matrix as the percent of Pd decreases with the increases of alumina precipitate, total Helmholtz free energy shows decreasing value with increasing ceramic fraction.

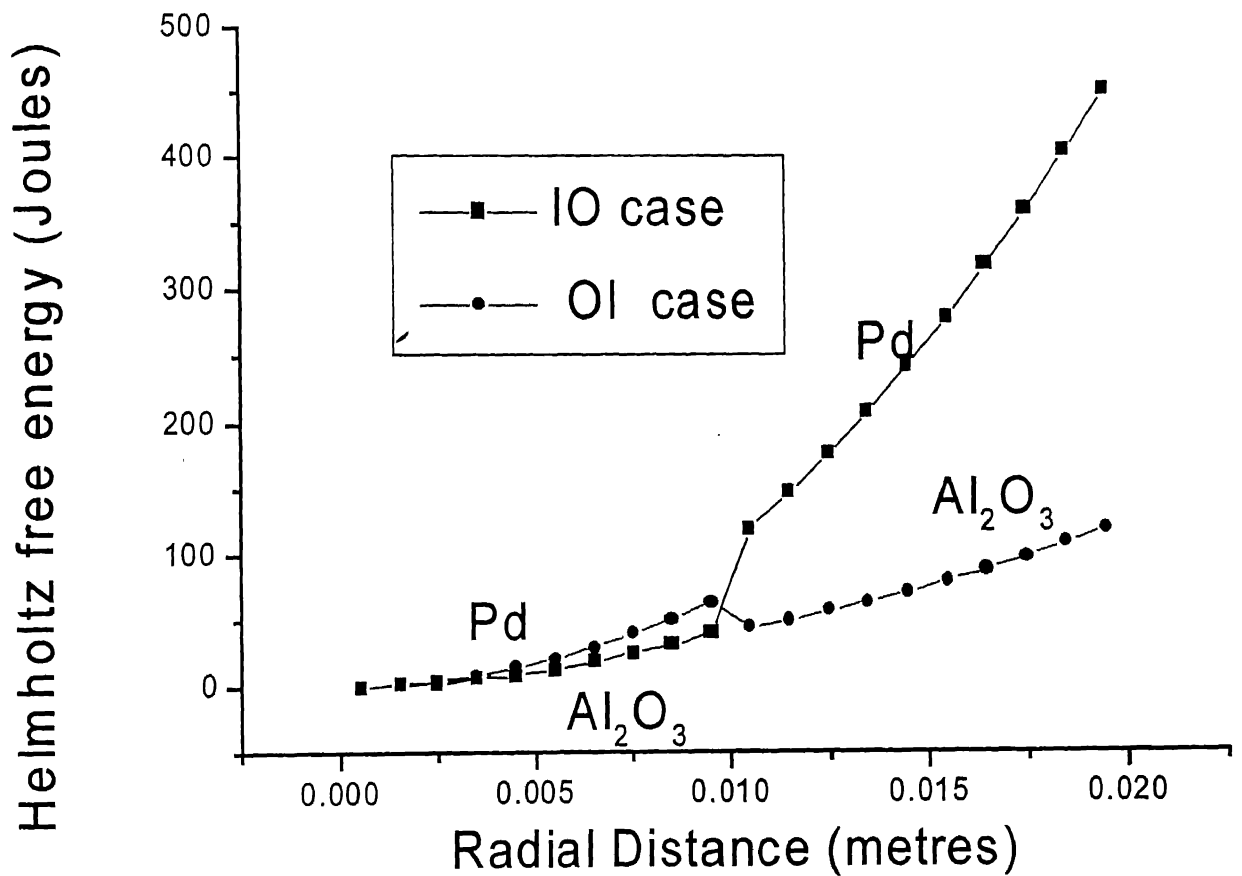


Figure 3.12 -- Variation of Helmholtz free energy as a function of radial distance at $\Delta T = 1000\text{K}$ for IO and OI cases.

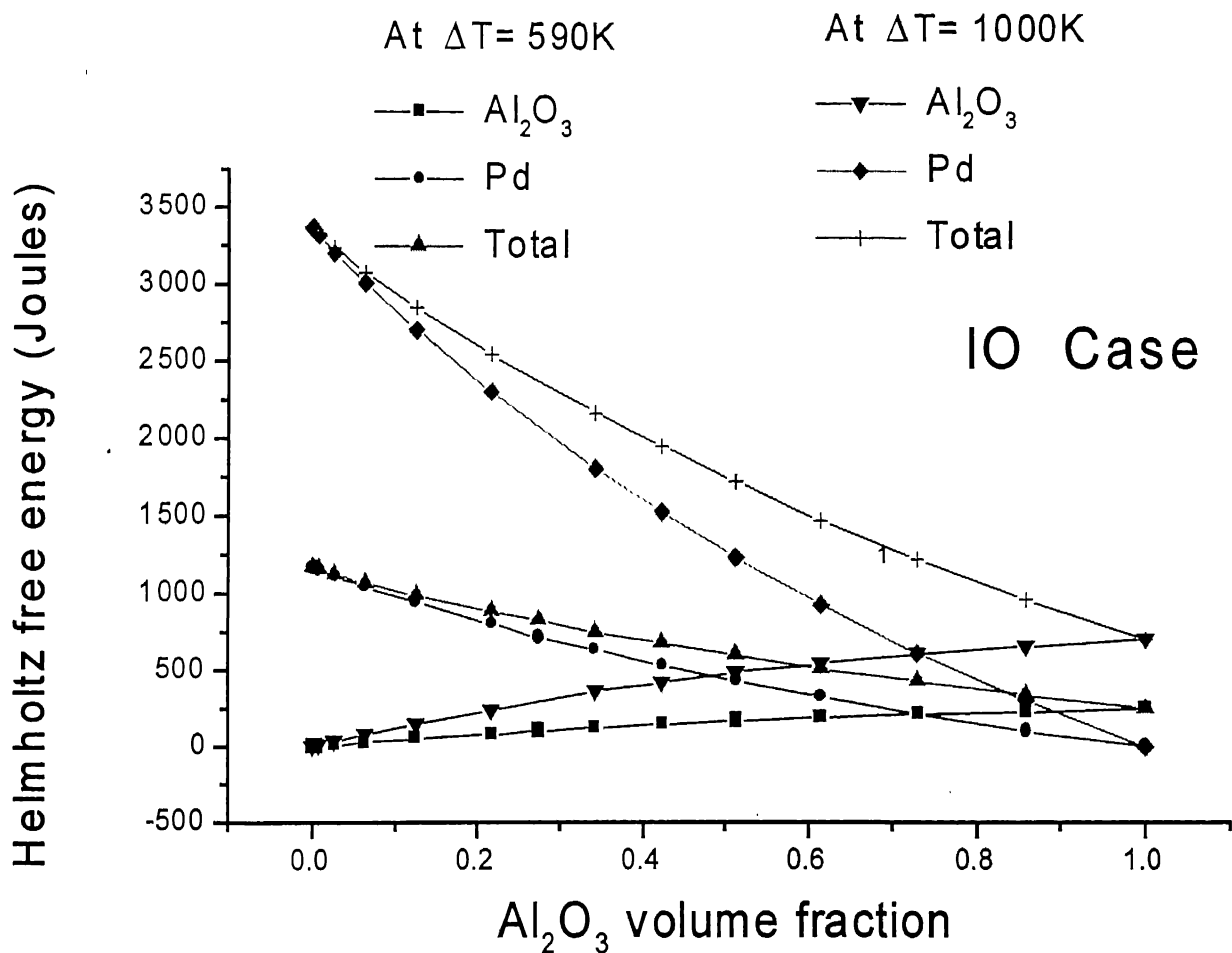


Figure 3.13 -- Variation of Helmholtz free energy as a function of Al_2O_3 precipitate volume fraction for different temperature difference values for IO case.

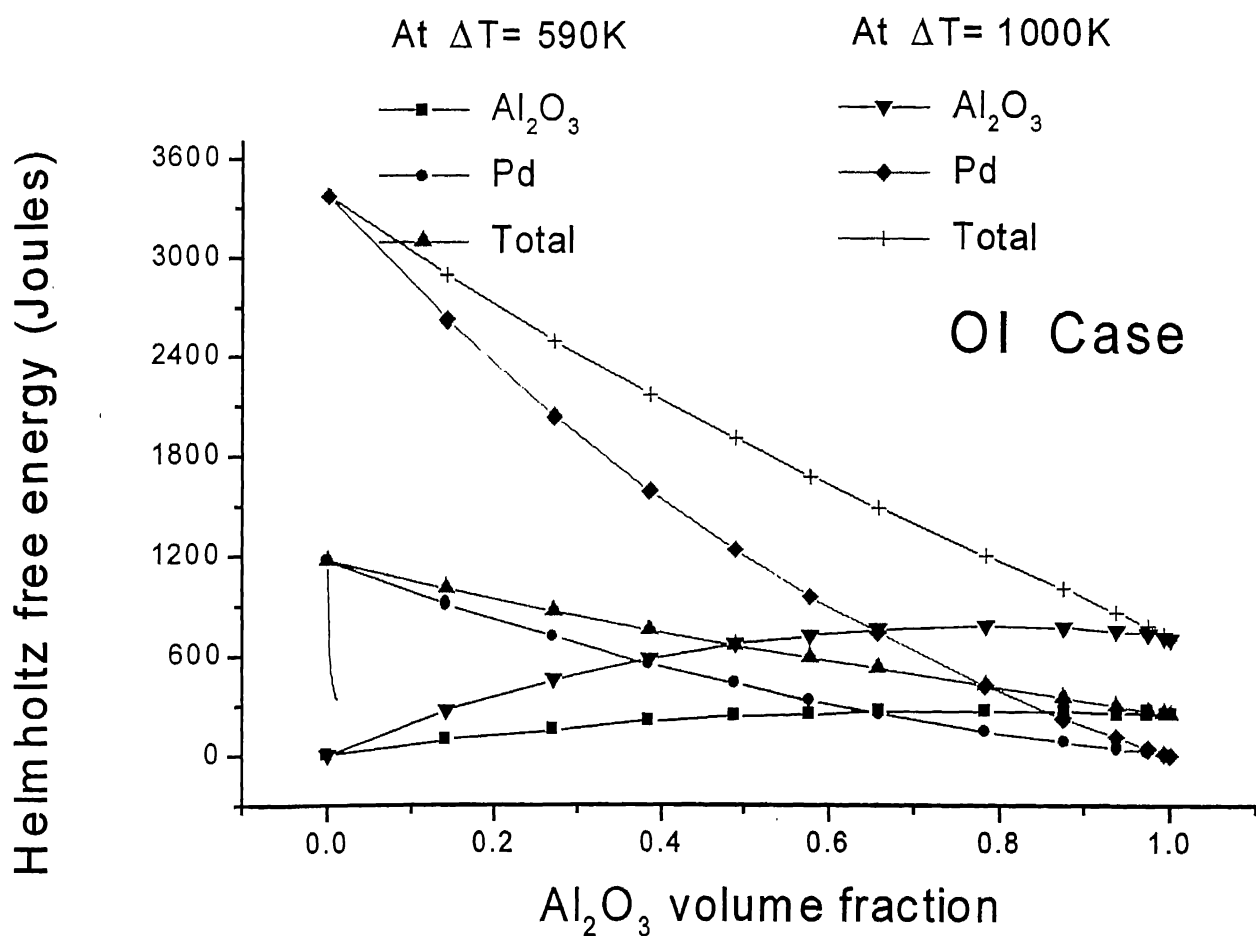


Figure 3.14 -- Variation of Helmholtz free energy as a functions of Al_2O_3 precipitate volume fraction for constant temperature difference for OI case.

3.8 Limitations Of The Model

The spherical infinite matrix considers only spherical precipitate and is based on a number of assumptions. These assumptions are basically the short coming of model. The major drawbacks of these model that no temperature change occur within the composite and model based on elastic case. Model gives the results for r and θ direction and fail to give results for third component ϕ , rather it assumes $\theta = \phi$ due to radial symmetry.

New model for cylindrical precipitate has been evaluates in the next chapter. It considers cylindrical precipitate in infinite cylindrical matrix (plane strain condition). The model considers temperature change within the composite.

Chapter 4

CYLINDRICAL PRECIPITATES (CASE - I)

Al_2O_3 precipitates are embedded in infinitely long cylindrical Pd matrix. It is cooled from high temperature to room temperature. Numbers of assumptions are made to evaluate this model. Basic assumptions of this model is that strain in z direction is neglected, so it is case of plain strain condition. The distance taken in x and y direction is same. The matrix has pure elastic behaviour. The stress-strain behaviour is independent of strain-rate and stress oriented. The temperature in MMC is vary all the directions in within the composites. The temperature near the origin changes drastically. For mathematical simplification, we assume that a given particle is surrounded by uniformly distributed neighbouring particles. This assumption allows us to use spherical coordinates whose origin is at the center of a ceramic particle with radial symmetry as shown in Figure 4.1. Each composite quarter element is divided into eight (8) divisions as shown in Figure 4.1, 1st division starts from x-axis and 8th division ends on y-axis.

4.1 Formulation Of Basic Equations

Consider an infinite cylindrical matrix whose internal surface contains ceramic particle and outer surface contains Pd matrix. The domain consists of four quarter parts and only first quarter is considered to study the FEM formulation as shown in Figure 4.1. Figure 4.1 shows the discretization of the domain for the case where Al_2O_3 precipitate is inside and Pd matrix is outside.

Any body subjected to external forces (body forces, surface forces) is described by the equations:

(i) Variables

Displacements: u, v, w which are functions of (x, y, z) .

Strain components: $\epsilon_{xx}, \epsilon_{yy}, \epsilon_{zz}, \epsilon_{xy}, \epsilon_{yz}$ and ϵ_{zx} .

Stress components: $\sigma_{xx}, \sigma_{yy}, \sigma_{zz}, \sigma_{xy}, \sigma_{yz}$ and σ_{zx} .

Where x, y and z are the direction of cartesian coordinates.

- (ii) In the present case, basic assumption is made that strain in third direction (z) is zero, so it becomes a plain strain case. Stress-strain relations for plain strain case is given below:

Strain in z direction is zero.

$$\begin{aligned}\varepsilon_{yz} = \varepsilon_{zx} = \varepsilon_{zz} &= 0 \\ \sigma_{xz} = 2\mu \varepsilon_{zx} &= 0 \quad \text{and} \quad \sigma_{yz} = 2\mu \varepsilon_{yz} = 0\end{aligned}$$

$$\sigma_{xx} = \lambda(\varepsilon_{xx} + \varepsilon_{yy}) + 2\mu\varepsilon_{xx} - (3\lambda + 2\mu)\alpha T \quad 4.1$$

$$\sigma_{yy} = \lambda(\varepsilon_{xx} + \varepsilon_{yy}) + 2\mu\varepsilon_{yy} - (3\lambda + 2\mu)\alpha T \quad 4.2$$

$$\sigma_{zz} = \lambda(\varepsilon_{xx} + \varepsilon_{yy}) + 2\mu\varepsilon_{zz} - (3\lambda + 2\mu)\alpha T \quad 4.3$$

$$\sigma_{xy} = 2\mu \varepsilon_{xy} \quad 4.4$$

$$\text{where } \lambda = \frac{\nu E}{(1+\nu)(1-2\nu)} \quad \text{and} \quad \mu = G = \frac{E}{2(1+\nu)}$$

ν = Poisson's Ratio of material.

E = Young's Modulus of material

T = Temperature of the composite of material.

$\mu = G$ = Shear Modulus of material

α = coefficient of thermal expansion of material

The strain equations are given by

The strain equations are given by:-

$$\varepsilon_{xx} = \frac{\partial u}{\partial x} = \text{strain in x direction} \quad 4.5$$

$$\varepsilon_{yy} = \frac{\partial v}{\partial y} = \text{strain in y direction} \quad 4.6$$

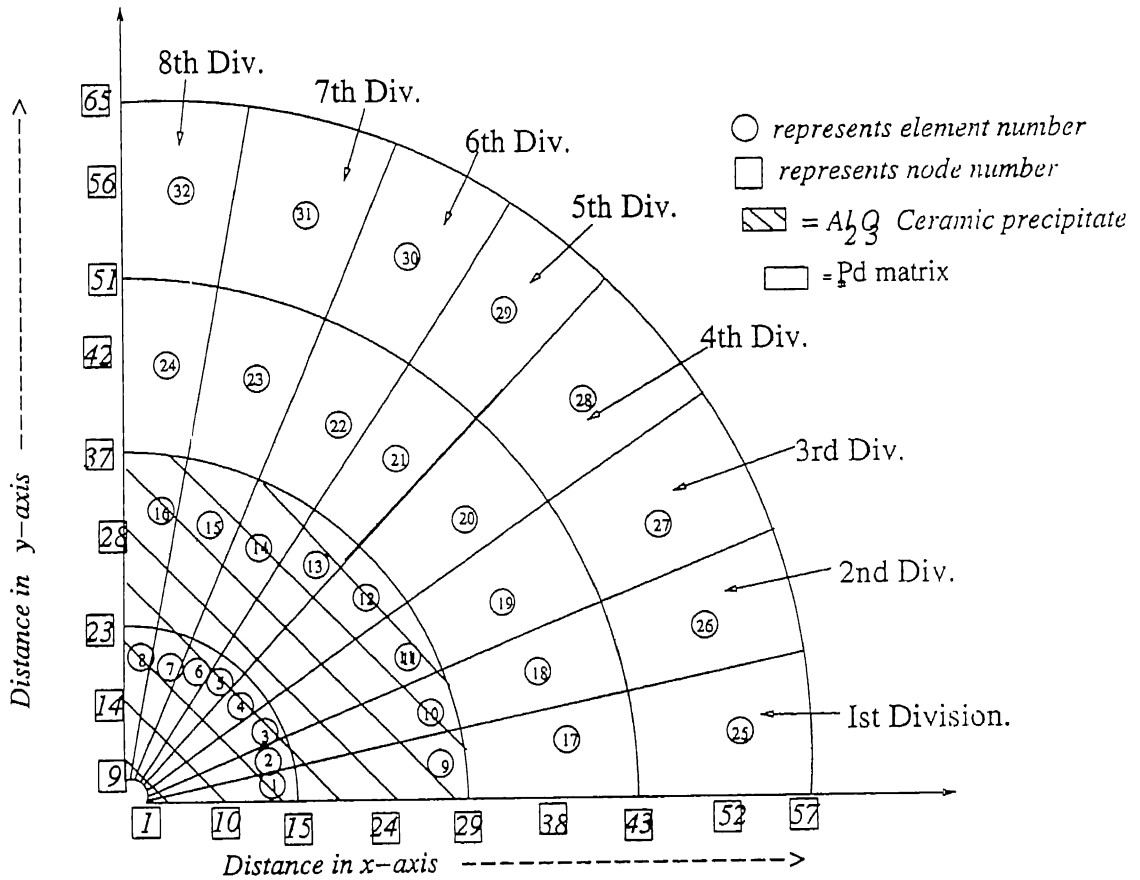


Figure 4.1 -- Discretization of the quarter domain using 2-D elements.

$$\varepsilon_{xy} = \frac{1}{2} \left(\frac{\partial u}{\partial y} + \frac{\partial v}{\partial x} \right) = \text{shear strain in x-y direction} \quad 4.7$$

Equations (4.1) to (4.4) can be inverted to gives the stresses in terms of strain (from equations 4.5 to 4.7) and temperature in matrix form:

$$\begin{aligned} \{\sigma\} &= \begin{Bmatrix} \sigma_{xx} \\ \sigma_{yy} \\ \sigma_{xy} \end{Bmatrix} = \begin{bmatrix} \lambda + 2\mu & \lambda & 0 \\ \lambda & \lambda + 2\mu & 0 \\ 0 & 0 & \mu \end{bmatrix} \begin{Bmatrix} \varepsilon_{xx} \\ \varepsilon_{yy} \\ 2\varepsilon_{xy} \end{Bmatrix} - (3\lambda + 2\mu)\alpha T \begin{Bmatrix} 1 \\ 1 \\ 0 \end{Bmatrix} \\ \{\sigma\} &= [D]_e \{\varepsilon\} - [D]_{Th} \{T\} \end{aligned} \quad 4.8$$

$$[D]_e = \begin{bmatrix} \lambda + 2\mu & \lambda & 0 \\ \lambda & \lambda + 2\mu & 0 \\ 0 & 0 & \mu \end{bmatrix} \text{ where } [D]_e \text{ is known as elastic property matrix [35].} \quad 4.9$$

It is clear that $[D]_e$ is a symmetric matrix.

$$[D]_{Th} = (3\lambda + 2\mu)\alpha \begin{Bmatrix} 1 \\ 1 \\ 0 \end{Bmatrix} \text{ where } [D]_{Th} \text{ thermal elastic property matrix.} \quad 4.10$$

4.2 Variational FEM Method

Variational approach has been discussed in section 3.2 for evaluating infinite spherical matrix. Variational formulations for elastic problems is developed either from governing differential equations or an equivalent physical principle. Second approach is followed to formulate the FEM problem. The strain energy in absence of body force is given by: -

$$\text{Strian energy} = I = \int_D \frac{1}{2} (\sigma_{xx} \varepsilon_{xx} + \sigma_{yy} \varepsilon_{yy} + 2\sigma_{xy} \varepsilon_{xy}) dA \quad 4.11$$

Strain energy in matrix form of stress and strain is given by

$$I = \int_D \frac{1}{2} (\sigma)^T \{\varepsilon\} dA \quad 4.12$$

Putting equations 4.8 in 4.12 gives :-

$$I = \int_D \left[\frac{1}{2} \{\varepsilon\}^T [D]_e \{\varepsilon\} - \{T\}^T [D]_{Th} \{\varepsilon\} \right] dA \quad 4.13$$

The variation of the dependent variable over each element is often expressed in terms of the unknown values of variable at certain point called a node and the known function is called the shape functions. Here, 8-noded isoparametric serendipity element is used to evaluate shape functions and mapping part element is shown on Figure 4.2.

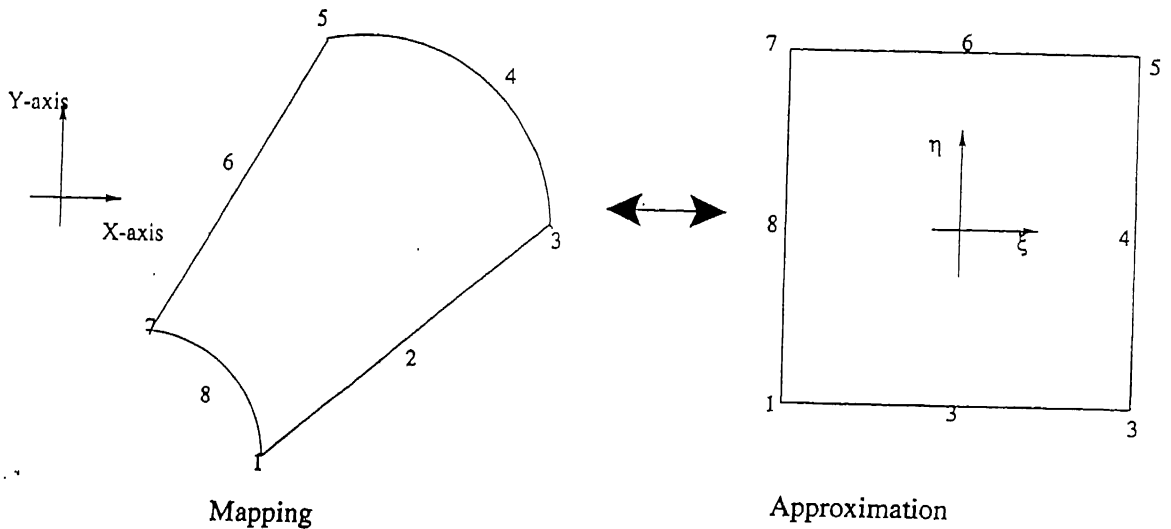


Figure 4.2 -- 8-noded isoparametric serendipity element.

The displacements and temperature in terms of shape functions are given by:

$$u = N_1^e u_1^e + N_2^e u_2^e + \dots + N_8^e u_8^e = \{N\}^e \{u\}^e \quad 4.14$$

$$v = N_1^e v_1^e + N_2^e v_2^e + \dots + N_8^e v_8^e = \{N\}^e \{v\}^e \quad 4.15$$

$$T = N_1^e T_1^e + N_2^e T_2^e + \dots + N_8^e T_8^e = \{N\}^e \{T\}^e \quad 4.16$$

Where u and v are the displacements in x and y directions only and T is the temperature term within the composite. Temperature in the composite is given by

$$\text{Temperature} = \text{Room temperature} + \text{temperature difference} \left(\frac{\log \frac{b}{r}}{\log \frac{b}{a}} \right)$$

where b = radius of precipitate in composite, a = radius at 1st node and r = radius.

The individual shape functions is given by:

$$\begin{aligned} N_1^e &= \frac{1}{4}(1-\xi)(1-\eta)(-1-\xi-\eta), & N_2^e &= \frac{1}{2}(1-\xi^2)(1-\eta), \\ N_3^e &= \frac{1}{4}(1+\xi)(1-\eta)(-1+\xi-\eta), & N_4^e &= \frac{1}{2}(1+\xi)(1-\eta^2), \\ N_5^e &= \frac{1}{4}(1+\xi)(1+\eta)(-1+\xi+\eta), & N_6^e &= \frac{1}{2}(1-\xi^2)(1+\eta), \\ N_7^e &= \frac{1}{4}(1-\xi)(1+\eta)(-1-\xi+\eta), & N_8^e &= \frac{1}{2}(1-\xi)(1-\eta^2). \end{aligned} \quad 4.17$$

Putting the values of derivatives of shape functions and element displacements, we obtain strain matrix from equations 4.5 and 4.7

$$\begin{aligned}
\{\varepsilon\} &= \begin{Bmatrix} \varepsilon_{xx} \\ \varepsilon_{yy} \\ 2\varepsilon_{zz} \end{Bmatrix} = \begin{Bmatrix} \frac{\partial u}{\partial x} \\ \frac{\partial v}{\partial y} \\ \frac{\partial u}{\partial y} + \frac{\partial v}{\partial x} \end{Bmatrix} = \begin{bmatrix} \frac{\partial N_1^e}{\partial x} & 0 & \frac{\partial N_2^e}{\partial x} & 0 & \dots & \frac{\partial N_8^e}{\partial x} & 0 \\ 0 & \frac{\partial N_1^e}{\partial y} & 0 & \frac{\partial N_2^e}{\partial y} & \dots & 0 & \frac{\partial N_8^e}{\partial y} \\ \frac{\partial N_1^e}{\partial y} & \frac{\partial N_1^e}{\partial x} & \frac{\partial N_2^e}{\partial y} & \frac{\partial N_2^e}{\partial x} & \dots & \frac{\partial N_8^e}{\partial y} & \frac{\partial N_8^e}{\partial x} \end{bmatrix} \begin{Bmatrix} u_1^e \\ v_1^e \\ u_2^e \\ v_2^e \\ \dots \\ u_8^e \\ v_8^e \end{Bmatrix} \\
&= \{B\}^e \{\delta\}^e
\end{aligned} \tag{4.18}$$

4.2.1 Calculation Of $\{B\}^e$ Matrix

In order to calculate coefficients of $\{B\}^e$, the derivatives of the shape function with respect to x and y are required, while these functions are given in terms of the intrinsic coordinates [35]: -

$$\begin{Bmatrix} \frac{\partial N_i^e}{\partial \xi} \\ \frac{\partial N_i^e}{\partial \eta} \end{Bmatrix} = \begin{bmatrix} \frac{\partial x}{\partial \xi} & \frac{\partial y}{\partial \xi} \\ \frac{\partial x}{\partial \eta} & \frac{\partial y}{\partial \eta} \end{bmatrix} \begin{Bmatrix} \frac{\partial N_i^e}{\partial x} \\ \frac{\partial N_i^e}{\partial y} \end{Bmatrix} \tag{4.19}$$

$$\begin{Bmatrix} \frac{\partial N_i^e}{\partial \xi} \\ \frac{\partial N_i^e}{\partial \eta} \end{Bmatrix} = [J] \begin{Bmatrix} \frac{\partial N_i^e}{\partial x} \\ \frac{\partial N_i^e}{\partial y} \end{Bmatrix}, \text{ where } [J] \text{ is the jacobian matrix.}$$

Inverting equation (4.18), the required shape functions derivatives can be obtained

$$\begin{Bmatrix} \frac{\partial N_i^e}{\partial x} \\ \frac{\partial N_i^e}{\partial y} \end{Bmatrix} = [J]^{-1} \begin{Bmatrix} \frac{\partial N_i^e}{\partial \xi} \\ \frac{\partial N_i^e}{\partial \eta} \end{Bmatrix}$$

$[J]^{-1}$ is impossible to solve as we cannot express shape functions in x and y rather we can express shape functions $\{N\}^e$ in terms of ξ and η .

We can easily evaluate $[J]$:-

$$\begin{aligned}
\begin{bmatrix} \frac{\partial x}{\partial \xi} & \frac{\partial y}{\partial \xi} \\ \frac{\partial x}{\partial \eta} & \frac{\partial y}{\partial \eta} \end{bmatrix} &= [J] = \begin{bmatrix} \frac{\sum_{i=1}^8 \partial N_i^e \cdot x_i^e}{\partial \xi} & \frac{\sum_{i=1}^8 \partial N_i^e \cdot y_i^e}{\partial \xi} \\ \frac{\sum_{i=1}^8 \partial N_i^e \cdot x_i^e}{\partial \eta} & \frac{\sum_{i=1}^8 \partial N_i^e \cdot y_i^e}{\partial \eta} \end{bmatrix} \\
&= \begin{bmatrix} \frac{\partial N_1^e}{\partial \xi} & \frac{\partial N_2^e}{\partial \xi} & \dots & \frac{\partial N_8^e}{\partial \xi} \\ \frac{\partial N_1^e}{\partial \eta} & \frac{\partial N_2^e}{\partial \eta} & \dots & \frac{\partial N_8^e}{\partial \eta} \end{bmatrix} \begin{bmatrix} x_1^e & y_1^e \\ x_2^e & y_2^e \\ \dots & \dots \\ x_8^e & y_8^e \end{bmatrix}
\end{aligned}$$

Putting equation (4.19) into eq. (4.18) gives $\{B\}^e$.

$\{\delta\}^e$ is the element displacement vector containing radial displacement at each node, substituting equation (4.19) for I leads to

$$\begin{aligned}
I &= \int_D \left(\frac{1}{2} \{\delta\}^{eT} \{B\}^{eT} [D]_e \{B\}^e \{\delta\}^e - \{\delta\}^{eT} [D]_{Th} \{B\}^e \{T\}^e \right) dA \\
I &= \sum_{i=1}^{n_e} \left[\frac{1}{2} \{\delta\}^{eT} [k]^e \{\delta\}^e - \{\delta\}^{eT} \{f_{Th}\}^e \right] \tag{4.20}
\end{aligned}$$

$$\text{where } [k]^e = \int_D \{B\}^{eT} [D]_e \{B\}^e dA = \text{elemental coefficient matrix} \tag{4.21}$$

$$\{f_{Th}\}^e = \int_D \{T\}^e [D]_{Th} \{B\}^e dA = \text{elemental right side vector} \tag{4.22}$$

4.2.2 Gaussian Quadrature

With higher-order elements, in which not only displacements but also strains and stresses vary over each element, the integration involved in the variational formulations generally cannot be evaluated analytically [35]. If there is no restriction on the positions at which the functions can be evaluated, then there is a class of numerical integration procedures referred to as Gaussian quadrature which to be preferred.

For integration of a functions, $f(\xi, \eta)$, of the independent variables over the two-dimensional region defined by $-1 < \xi < +1, -1 < \eta < +1$. The integration is given by

$$\int_{-1}^{+1} \int_{-1}^{+1} f(\xi, \eta) d\xi d\eta \approx \sum_{i=1}^{n_\xi} \sum_{j=1}^{n_\eta} w_i w_j f[\xi_i, \eta_j] \quad 4.23$$

where the ξ_i, w_i and η_j, w_j are the pairs of abscissae and weight factors established for functions of single variables [35].

Equation (4.21) is given by: -

$$\{f\}_{Th} = \sum_{i=1}^{n_\xi} \sum_{j=1}^{n_\eta} w_i w_j f \left[\{B\}^e{}^T [D]_e \{B\}^e \det |J| \right]_{\substack{\xi=\xi_i \\ \eta=\eta_j}}$$

Where $\det |J|$ is the determinant of jacobian matrix.

Equation (4.22) is given by

$$\{f\}_{Th}^e = \sum_{i=1}^{n_\xi} \sum_{j=1}^{n_\eta} w_i w_j f \left[\{T\}^T [D]_{Th} \{B\}^e \det |J| \right]_{\substack{\xi=\xi_i \\ \eta=\eta_j}}$$

We have used four noded gauss values to evaluate integration and their values are

$$\xi_1 = \eta_1 = -0.86113, \quad w_1 = 0.347855.$$

$$\xi_2 = \eta_2 = -0.33998, \quad w_2 = 0.652145.$$

$$\xi_3 = \eta_3 = 0.33998, \quad w_3 = 0.652145.$$

$$\xi_4 = \eta_4 = 0.86113, \quad w_4 = 0.347855.$$

The elemental displacement vector $\{\delta\}^e$ is related to global displacement vector $\{\Delta\}$ by the following equation:

$$\{\delta\}^e = [A]^e \{\Delta\} \quad 4.24$$

where the matrix $[A]^e$ depends on the elemental (i.e. load) and global node necessary systems. Substitution of equation 4.22 in 4.19, we get

$$I = \frac{1}{2} \{\Delta\}^T [K] \{\Delta\} - \{\Delta\}^T [F] \quad 4.25$$

$$[K] = \sum_{e=1}^n [A]^e{}^T [K]^e [A]^e \quad \text{where } [K] \text{ is the global body force vector.}$$

$$[F] = \sum_{e=1}^n [A]^e \{f_{Th}\}^e \quad \text{where } [F] \text{ is global right side vector.}$$

Extremization of I leads to (i.e. $\frac{\partial I}{\partial \Delta} = 0$)

$$\boxed{[K]\{\Delta\} = \{F\}} \quad 4.26$$

Solving the above equation gives displacement at all the nodes in X and Y directions.

Calculation of $[D]_e$ and $[D]_{Th}$ matrices

Composite consists of Pd and Al_2O_3 materials and there $[D]_e$ and $[D]_{Th}$ matrices are different for different material.

For Pd-matrix

$$[D]_e = \frac{4E_{mat}}{11} \begin{bmatrix} 5 & 3\sqrt{2} \\ 3\sqrt{2} & 8 \end{bmatrix} \quad [D]_{Th} = 4.E_{mat}.11.5 * 10^{-6} \begin{Bmatrix} 1 \\ 1 \\ 0 \end{Bmatrix}$$

For Al_2O_3 Ceramic Precipitates

$$[D]_e = \frac{E_{ppt}}{10} \begin{bmatrix} 12 & 4\sqrt{2} \\ 4\sqrt{2} & 10 \end{bmatrix} \quad [D]_{Th} = 2E_{ppt}.8.0 * 10^{-6} \begin{Bmatrix} 1 \\ 1 \\ 0 \end{Bmatrix}$$

4.3 Estimation of Displacements

Displacements at all nodes in the x and y direction can be solved by solving equation 4.26. Here, u means displacement in x direction and v means displacement in y direction. The composite is made to cool from high temperature to room temperature, in discussing the model $\Delta T = 800\text{K}$ means the difference between the temperature inside the composite to the outside the temperature is 800K. The temperature profile is shown at Figure 4.3 for $\Delta T = 800\text{K}$. Two types of cases are considered for analyzing FEM model and these are shown in figure 4.4. The first case will be called IO case where Al_2O_3 precipitate is inside the system and Pd matrix is outside and in the second OI, the Al_2O_3 precipitate is outside and Pd matrix is inside.

Figure 4.5.a and Figure 4.5.b show the variation of displacement of nodal points in x-axis line for IO and OI case at $\Delta T = 800\text{K}$ as a function of x-axis. In IO case, displacements in x direction (u) is positive where displacements in y directions (v) is negative. The value of displacement of Pd matrix is always higher than the Al_2O_3 due to higher coefficient of thermal expansion (CTEs) of Pd ($\alpha_m = 11.5 \times 10^{-6} / \text{K}$) than that of Al_2O_3 ($\alpha_c = 8 \times 10^{-6} / \text{K}$). In OI case, all the displacements values are negative it means that the particles are moving in negative x and y directions. Displacements are increasing with the increasing of distance.

Figures 4.6.a and 4.6.b show the variation of displacement for nodal points at y-axis line for both IO and OI cases respectively at $\Delta T = 800\text{K}$. The displacements value for initial part does not change much but at the interface the value changes. The Pd displacements are higher due to high CTEs of Pd matrix.

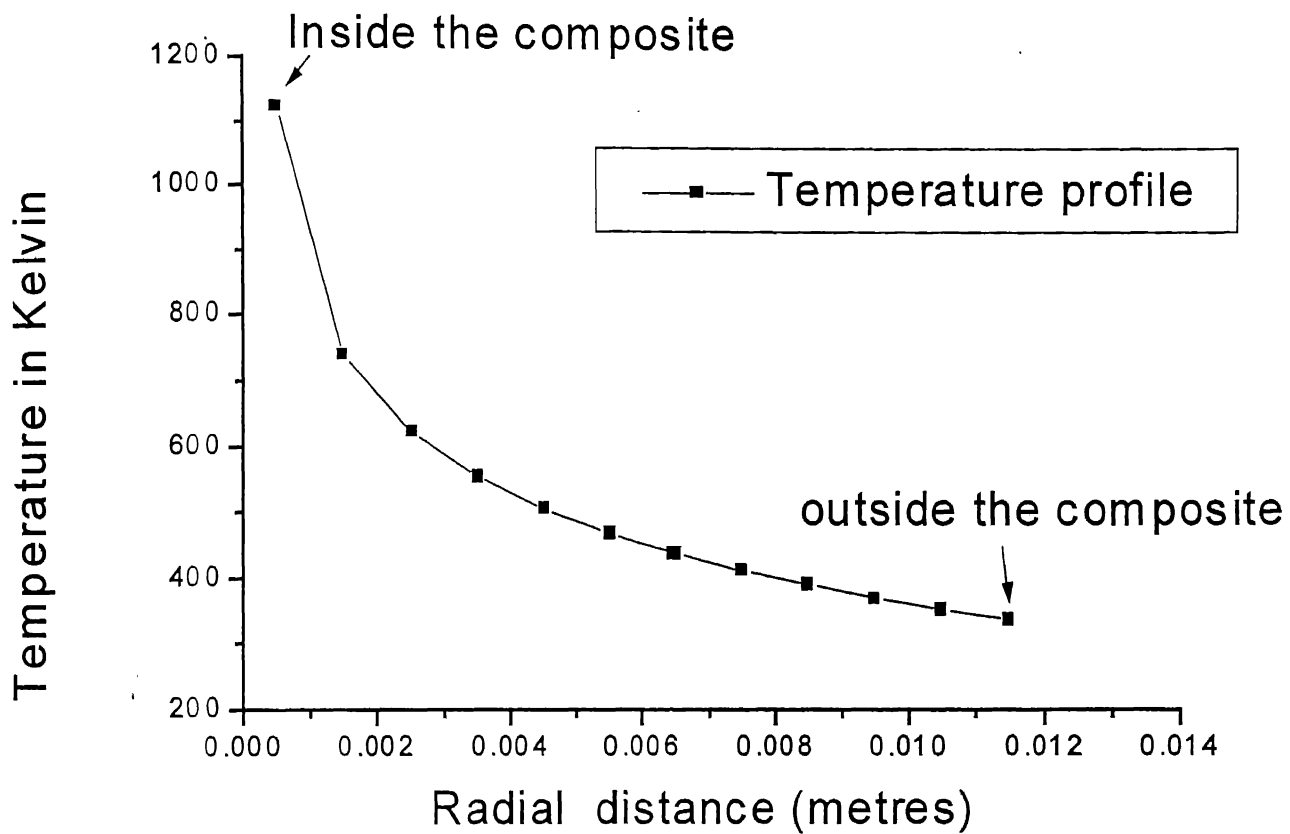


Figure 4.3 -- Temperature profile as a function of radial distance at $\Delta T = 800\text{K}$.

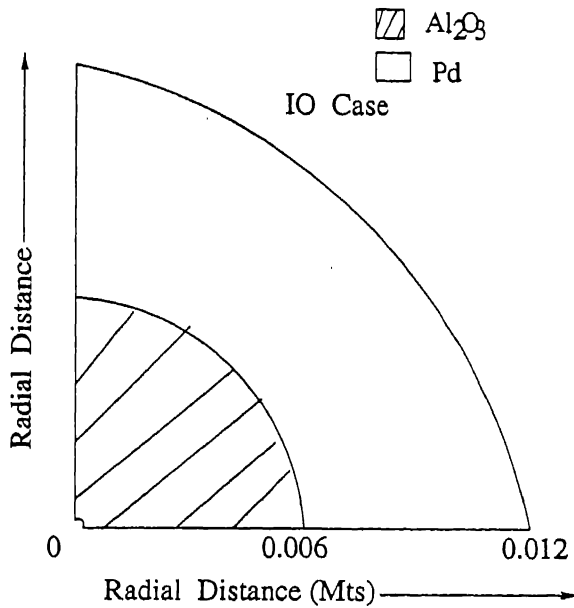


Figure 4.4.a - Cylindrical Precipitate is inside and Pd matrix is outside at $\Delta T=800\text{K}$ (Ceramic volume fraction 0.25) i.e. IO Case

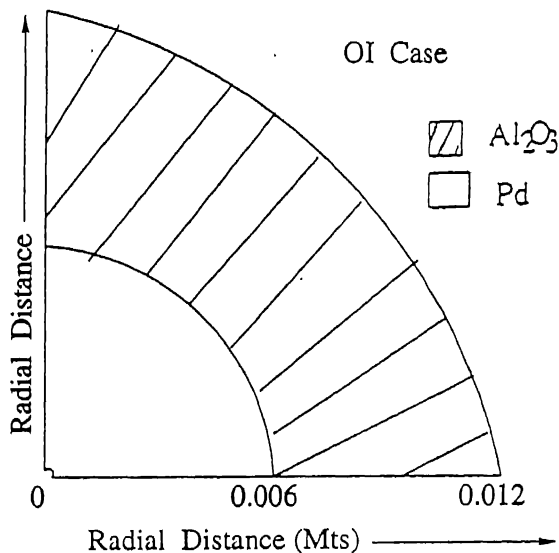


Figure 4.4.b - Cylindrical Precipitate is outside and Pd matrix is inside at $\Delta T=800\text{K}$ (Ceramic volume fraction 0.75) i.e. OI Case

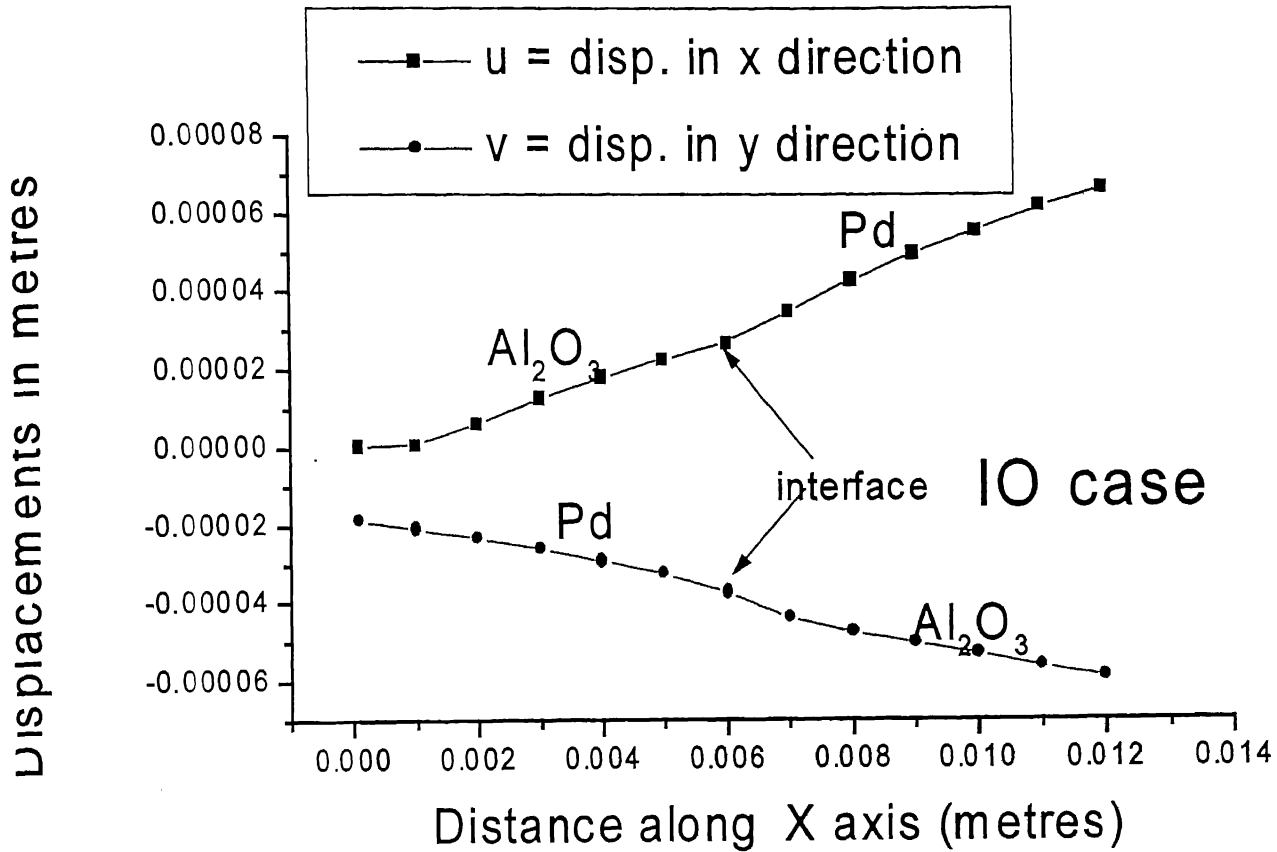


Figure 4.5.a -- Variation of displacements at nodal points as a function of distance along x-axis at $\Delta T=800K$ for IO case.

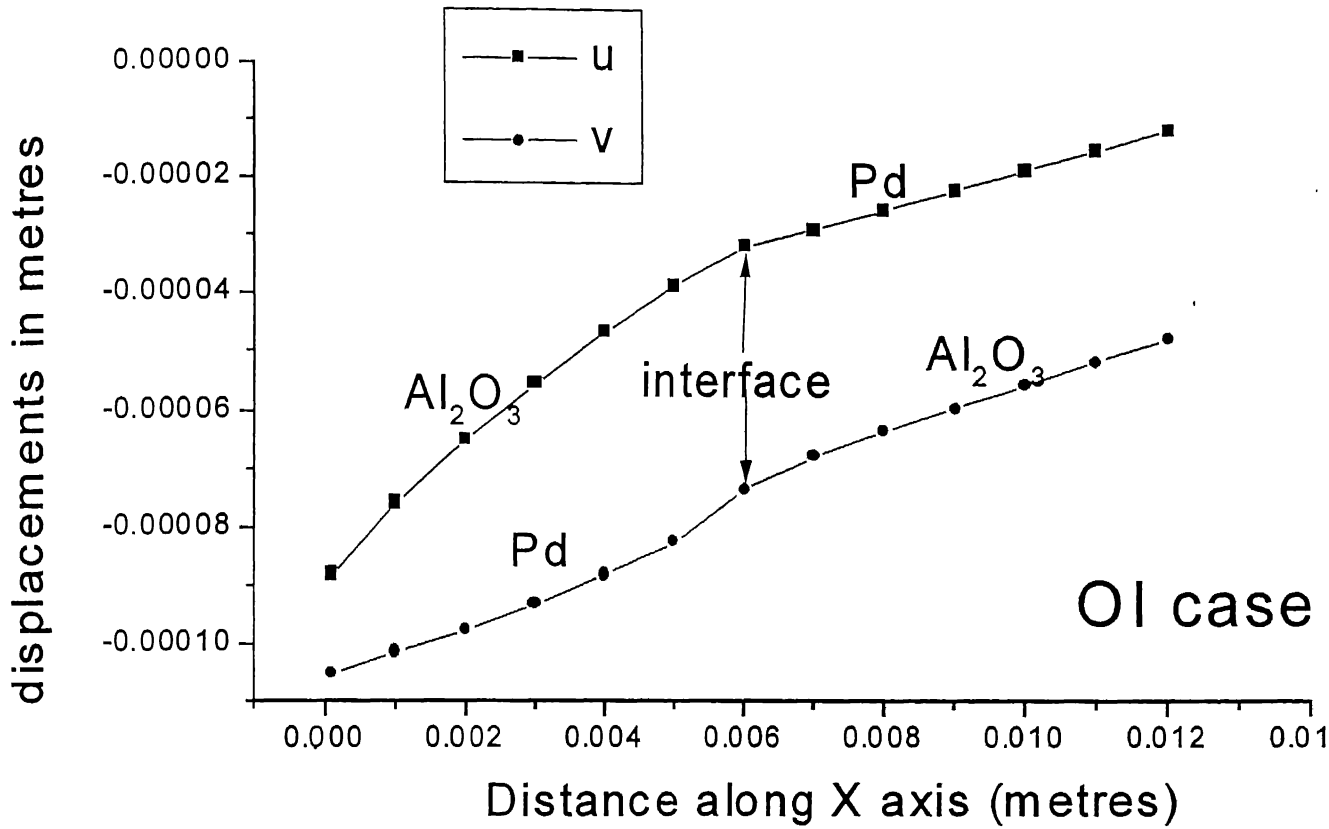


Figure 4.5.b -- Variation of displacements at nodal points as a function of distance along x-axis at $\Delta T=800K$ for OI case.

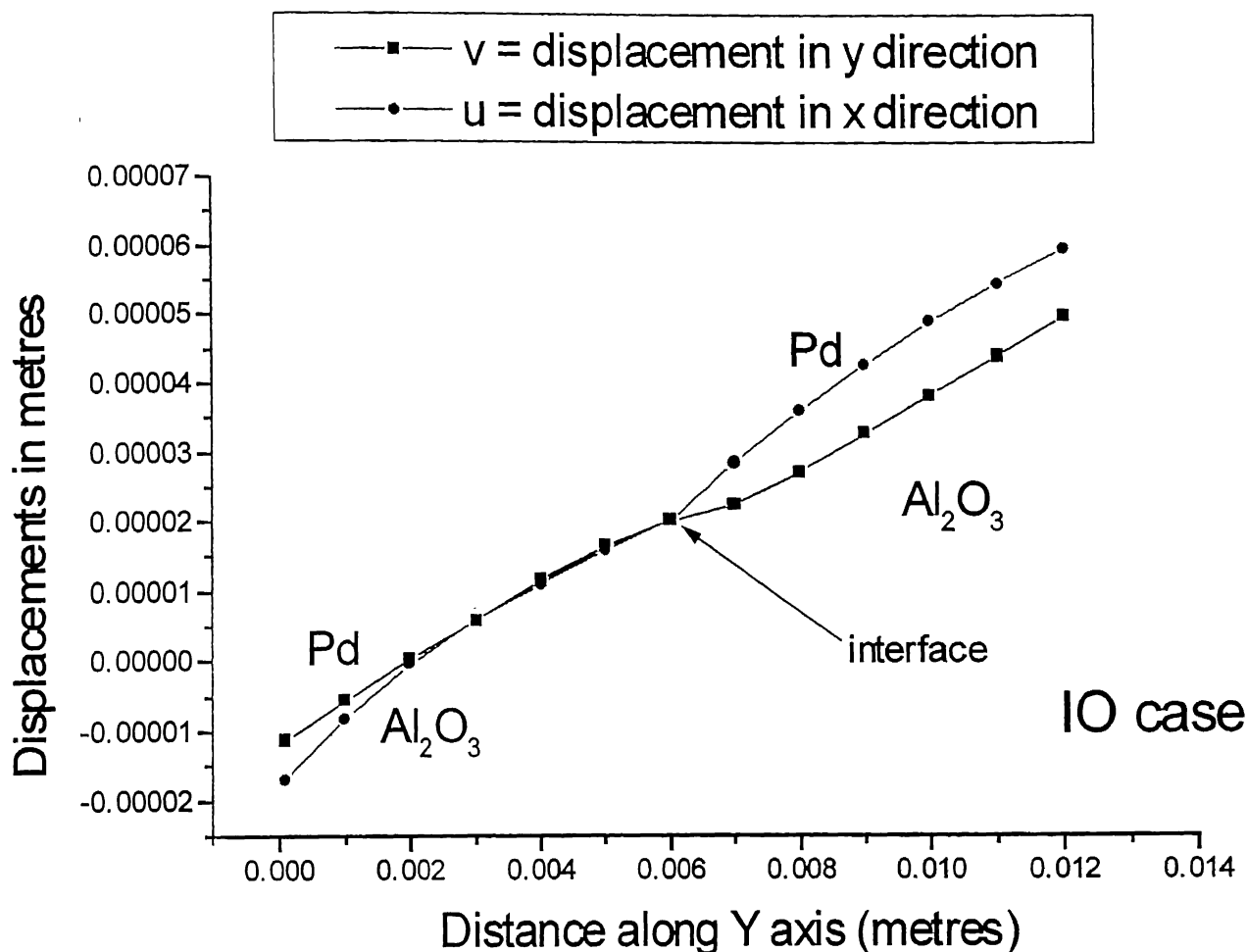


Figure 4.6.a -- Variation of displacements at nodal points as a function of distance along y-axis at $\Delta T=800\text{K}$ for IO case.

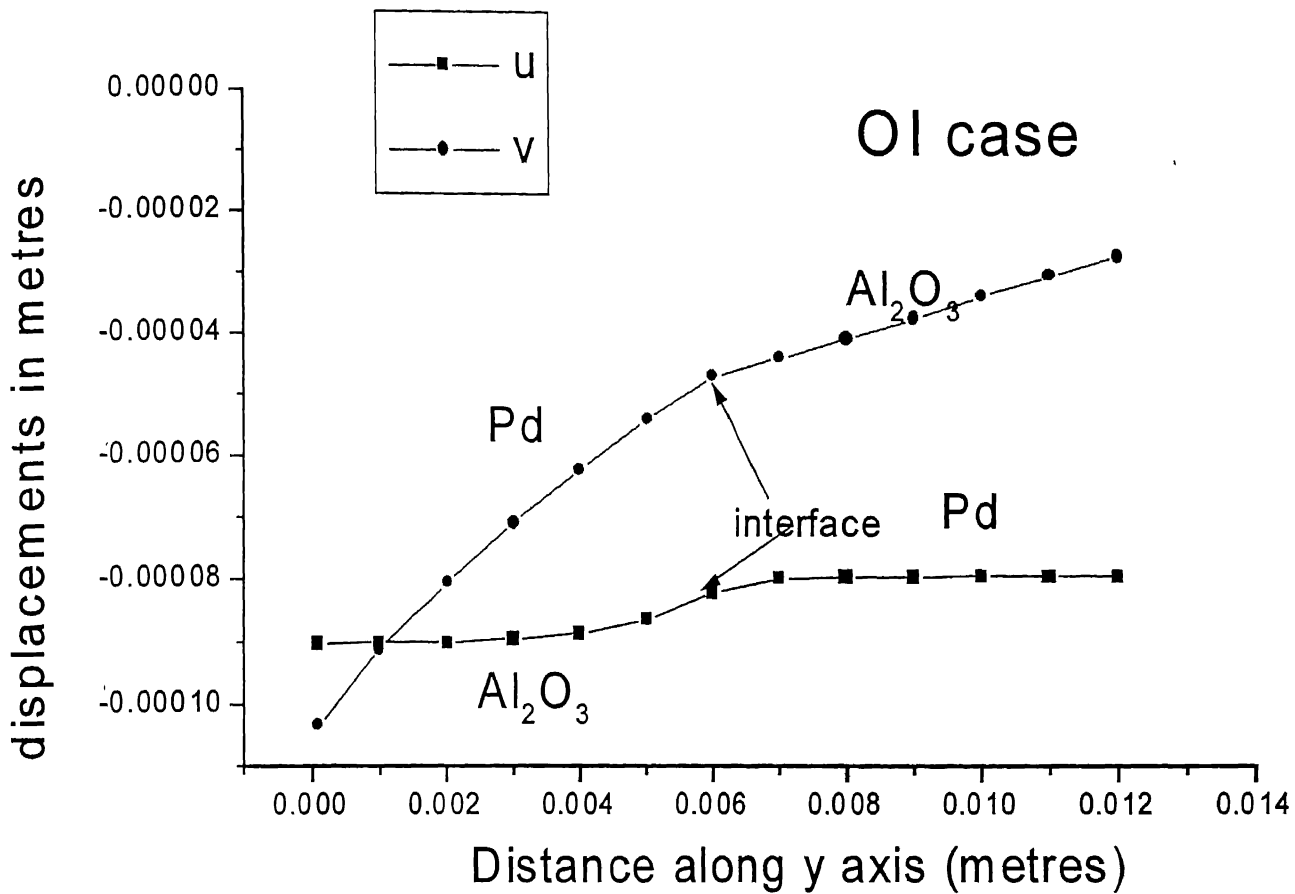


Figure 4.6.b -- Variation of displacements at nodal points as a function of distance along y-axis at $\Delta T=800K$ for OI case.

4.4 Estimation of Strains

After having evaluating displacements in x and y directions, strains can be evaluated from equation 4.17. Strain $\{\epsilon\}^e$ matrix at each element is evaluated at average gauss points. We have used 4 gauss points to integrate the $[k]^e$ and $\{f_{th}\}^e$ matrix. Average values of gauss points are made and these values were used to evaluate all the results involve elemental composite.

Figure 4.7 shows the variation of ϵ_{xx} as a functions of x-axis distance for IO and OI cases. The magnitude of strains for Pd matrix is higher than Al_2O_3 . The values of strains at 2nd, 5th & 8th divisions are nearly same for both the cases. Strains decreases with increase of distance because the temperature is also decreasing with increase of distance (equation 4.2). the lesser the temperature within the composite lesser will be the strain developed. Fluctuation of 2nd division at interface is more as compared to other division.

Figure 4.8 shows the variation of ϵ_{yy} as a distance for IO and OI cases at $\Delta T = 800K$. The trend obtained for Figure 4.7 nearly same as Figure 4.6 but the values are different. The strains for Pd is always more then Al_2O_3 due to high coefficient of thermal expansion of Al_2O_3 .

Figure 4.9 shows strains (ϵ_{xy}) as a function of distance at x-axis for both the cases at $\Delta T = 800K$. The values of OI case are higher than IO case. CTEs of Pd ($\alpha_m = 11.5 \times 10^{-6} /K$) is higher than Al_2O_3 ($\alpha_c = 8 \times 10^{-6} /K$), Pd's strains are always high as compared to Al_2O_3 .

4.5 Estimation of Stresses

Stresses can easily be evaluated if the strains and temperature profile at each element are known. It is obtained from equation 4.8. Stresses depend on strains, temperature and material properties per element. All the figures are evaluated at average of gauss points.

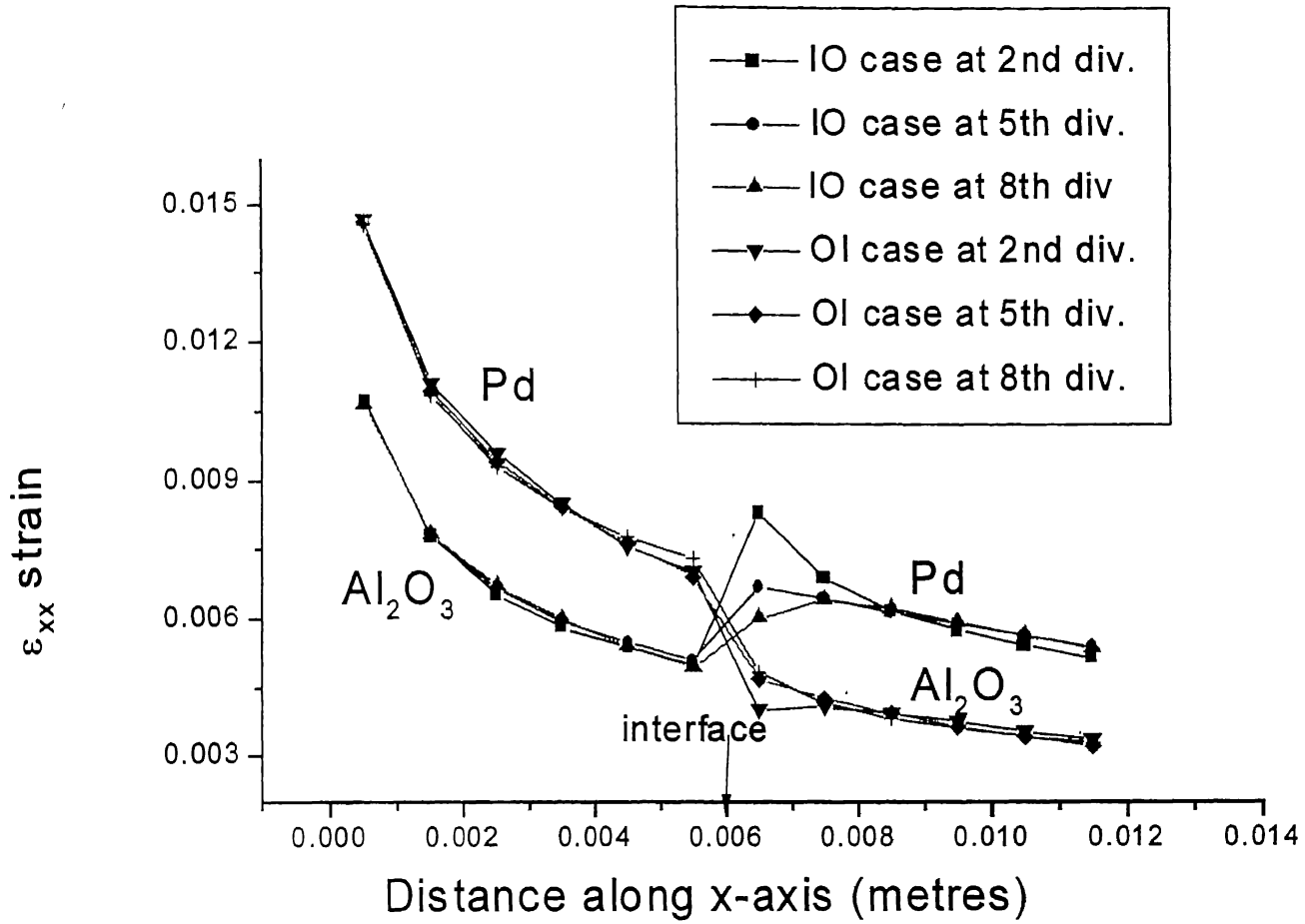


Figure 4.7 -- Variation of strain (ϵ_{xx}) as a function of distance along x-axis for $\Delta T=800K$ for IO and OI cases.

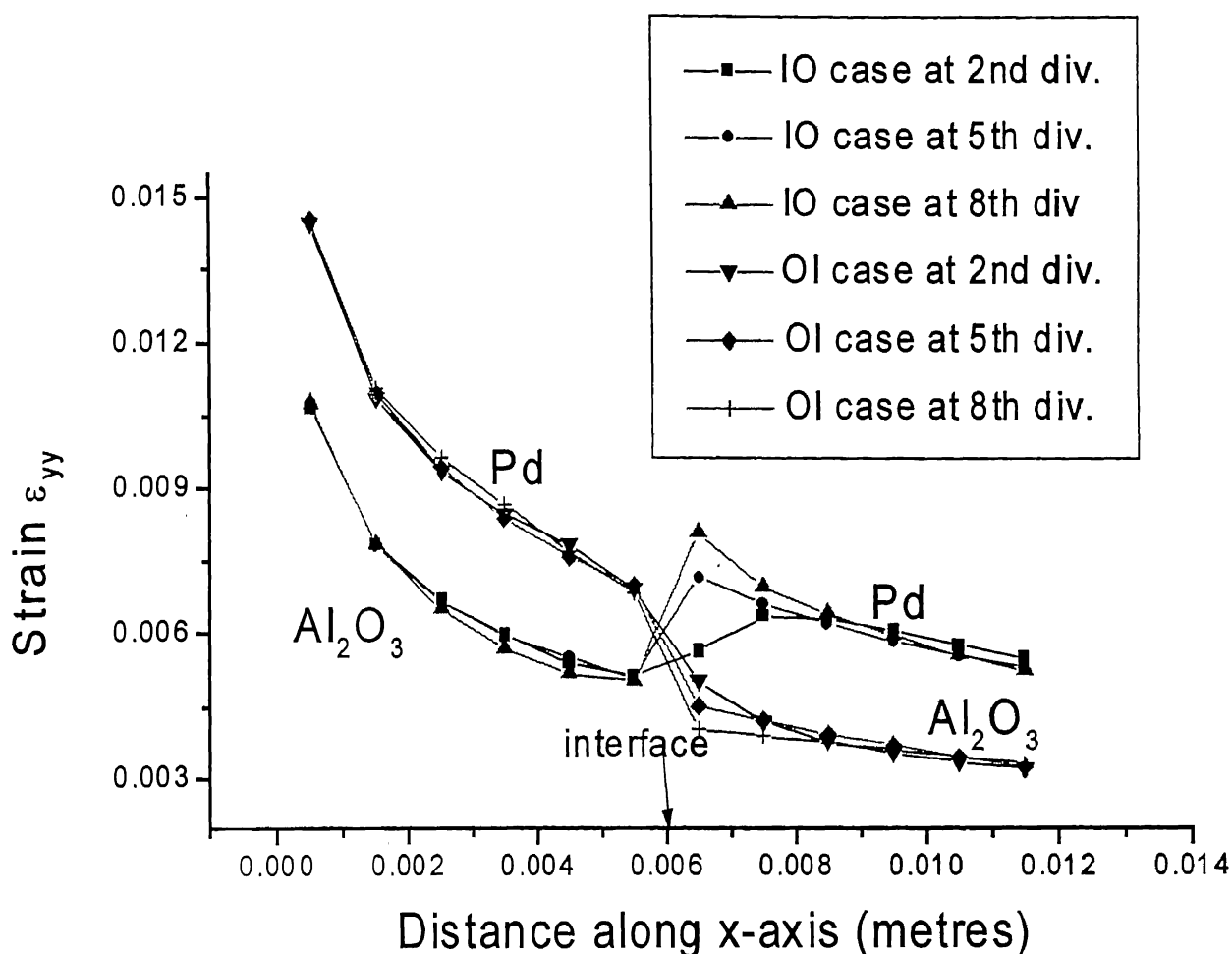


Figure 4.8 -- Variation of strain (ϵ_{yy}) as a function of distance along x-axis for $\Delta T=800K$ for IO and OI cases.

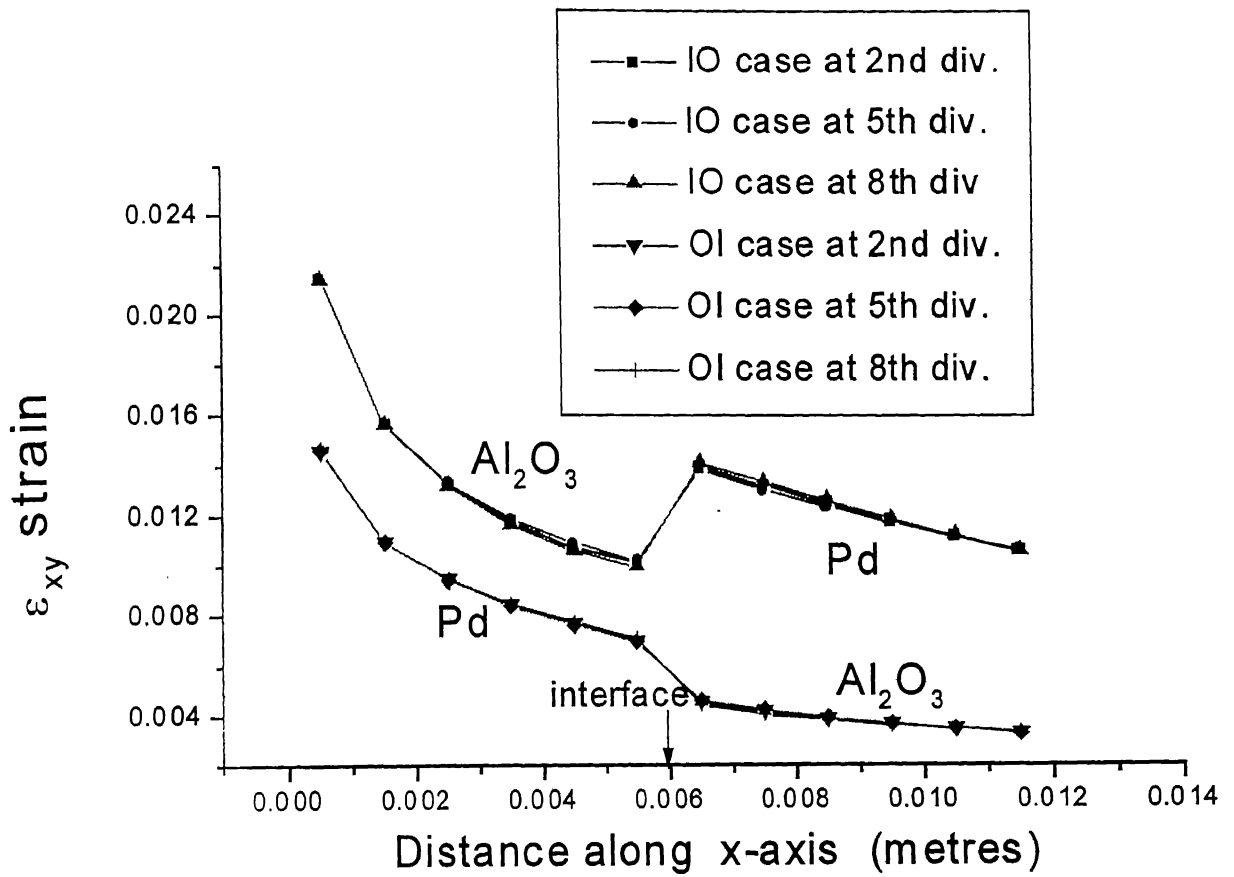


Figure 4.9 -- Variation of strain (ϵ_{xy}) as a function of distance along x-axis for $\Delta T=800K$ for IO and OI cases.

Figure 4.10.a and Figure 4.10.b show the variation σ_{xx} curve as function of distance along x-axis for both IO and OI cases at $\Delta T = 800K$. For IO case, initially as the temperature decreases with distance, stresses start decreasing but as the σ_{xx} reaches the Pd-Al₂O₃ interface, Al₂O₃ precipitate stresses shoot up due to high Young's Modulus ($E_c = 380$ GPa) as compared to Pd matrix ($E_m = 123$ GPa). To compensate the tensile stress in Al₂O₃, stresses developed in Pd matrix is compressive most of the time, this is shown by elements at the 5th div. For IO case, the stresses obtained by most of Al₂O₃ are tensile, whereas the stresses for Pd matrix is compressive. The reason behind this is that Al₂O₃'s Young's modulus value is much higher than Pd matrix.

Figure 4.11.a and Figure 4.11.b show the variation σ_{xx} curve as function of distance along x-axis for both IO and OI cases at $\Delta T = 800K$. The values obtained are similar to Figure 4.9.a and 4.9.b. The stresses for element of 2nd division fluctuates most.

Figure 4.12 shows the σ_{xy} stress curve as the function of x-axis at $\Delta T = 800K$. The results obtained for 2nd, 5th and 8th divisions are nearly same. The magnitude of σ_{xy} is higher by a factor of 10 as compared to σ_{xx} and σ_{yy} . Stresses (σ_{xy}) of Al₂O₃ is high due to high Young's Modulus of Al₂O₃ ($E_c = 380$ GPa) than that of Pd matrix ($E_m = 123$ GPa). The decreasing trend of stresses occurred due to decreasing of temperature with distance.

4.5.1 Estimation Of Polar Stresses From Cartesian Stresses

Polar stresses are important for calculating solubility enhancement ratio as it involves radial stress. Polar stresses are evaluated from the cartesian stresses from the following equations

$$\sigma_{rr} = \sigma_{xx} \cos^2 \theta + \sigma_{yy} \sin^2 \theta + 2\sigma_{xy} \sin \theta \cos \theta \quad 4.27$$

$$\sigma_{\theta\theta} = \sigma_{xx} \sin^2 \theta + \sigma_{yy} \cos^2 \theta - 2\sigma_{xy} \sin \theta \cos \theta \quad 4.28$$

$$\sigma_{r\theta} = (\sigma_{yy} - \sigma_{xx}) \sin \theta \cos \theta + \sigma_{xy} (\cos 2\theta) \quad 4.29$$

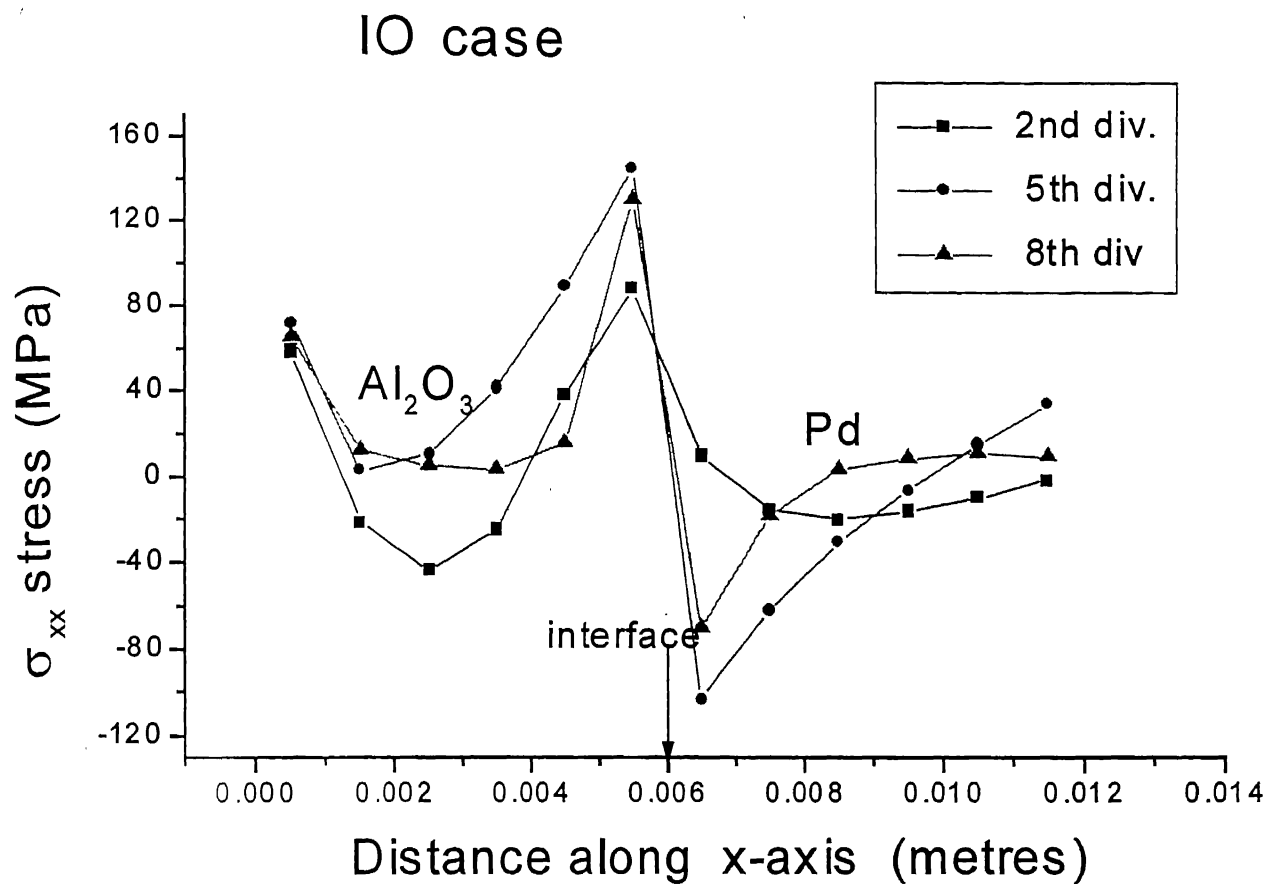


Figure 4.10.a -- Variation of stress (σ_{xx}) curve as a function of distance along x-axis at $\Delta T=800K$ for IO case.

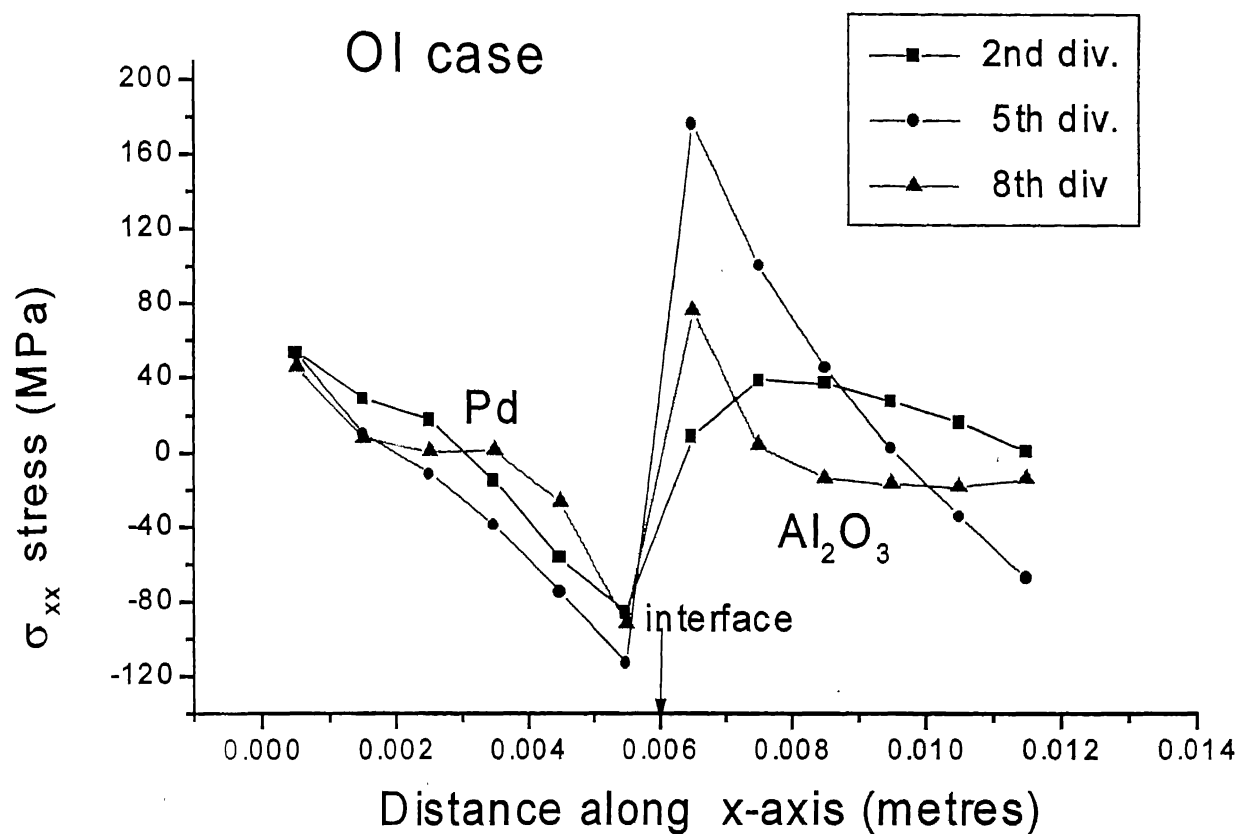


Figure 4.10.b -- Variation of stress (σ_{xx}) curve as a function of distance along x-axis at $\Delta T=800K$ for Ol case.

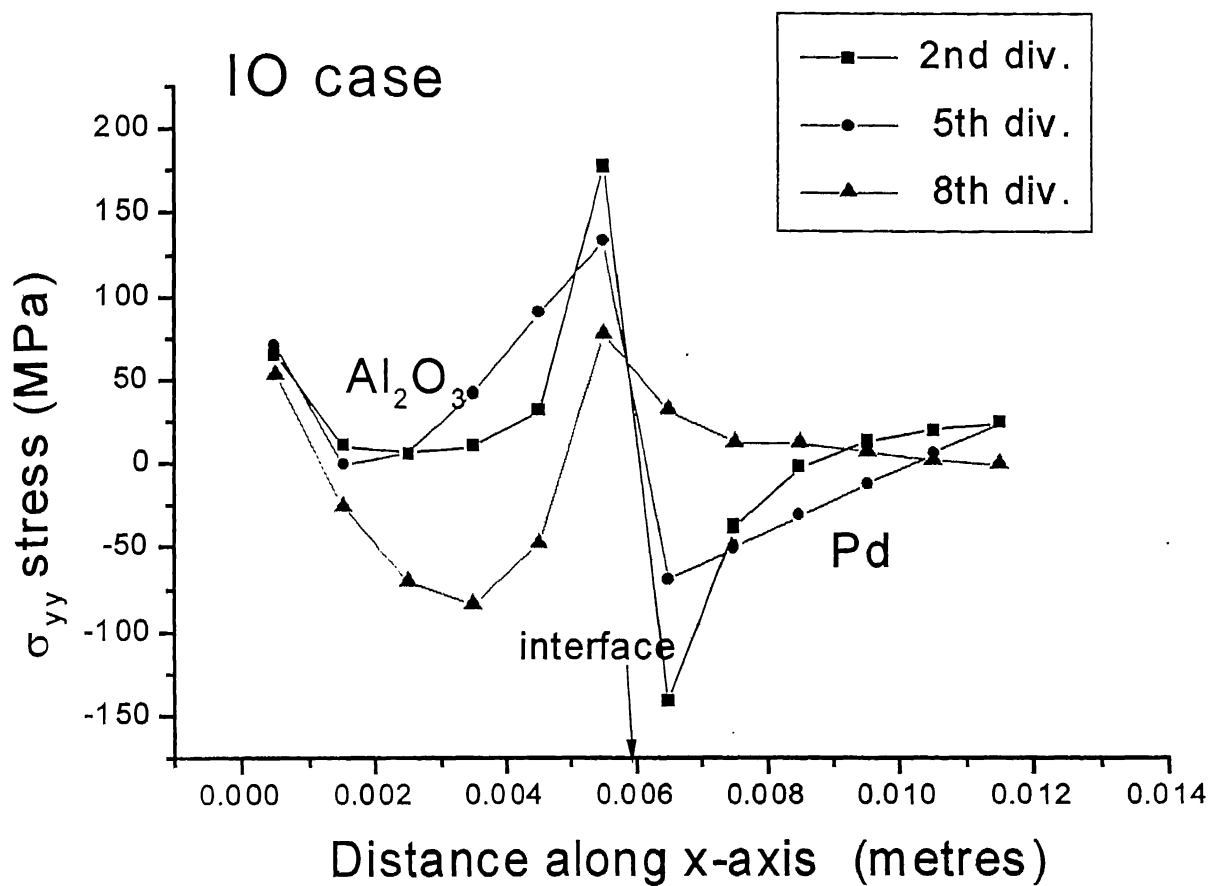


Figure 4.11.a -- Variation of stress (σ_{yy}) curve as a function of distance along x-axis at $\Delta T=800\text{K}$ for IO case.

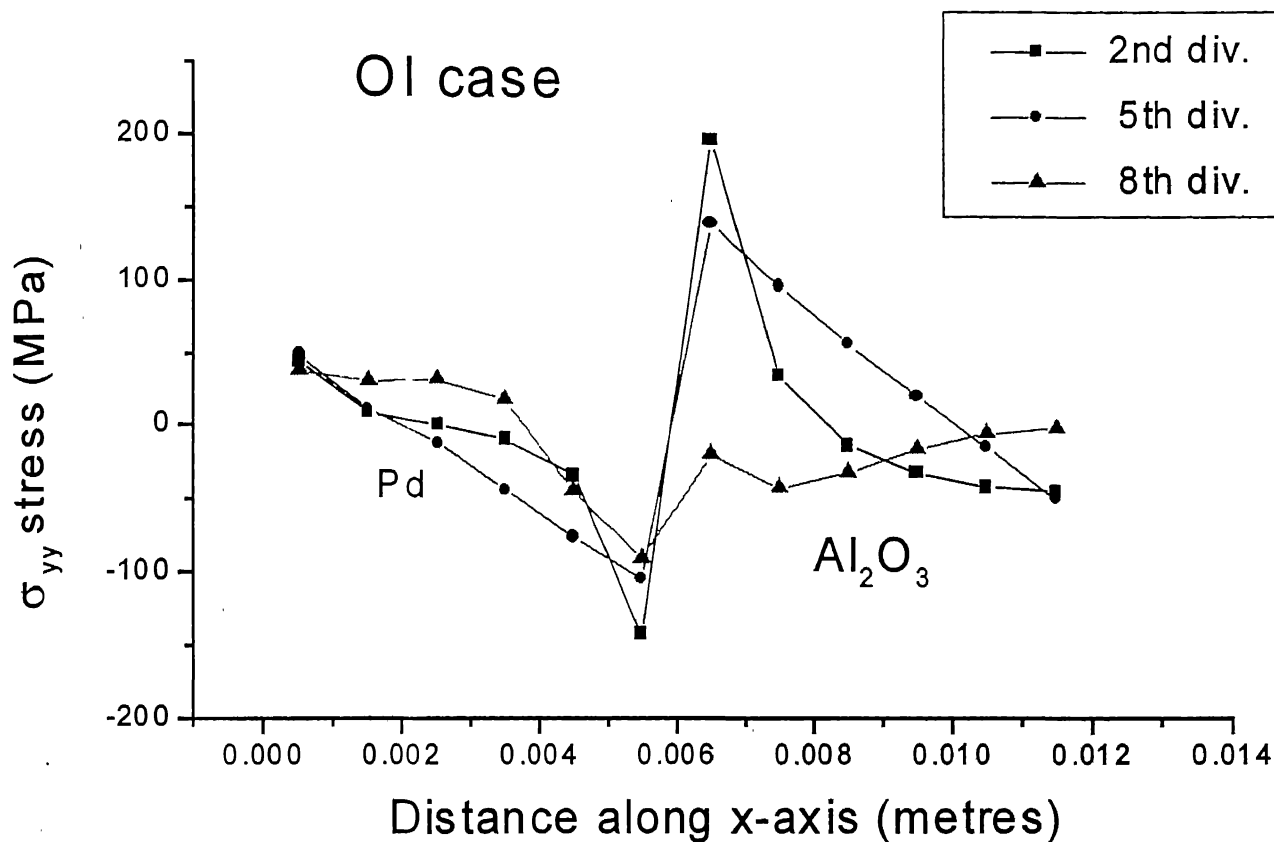


Figure 4.11.b -- Variation of stress (σ_{yy}) curve as a function of distance along x-axis at $\Delta T=800K$ for Ol case.

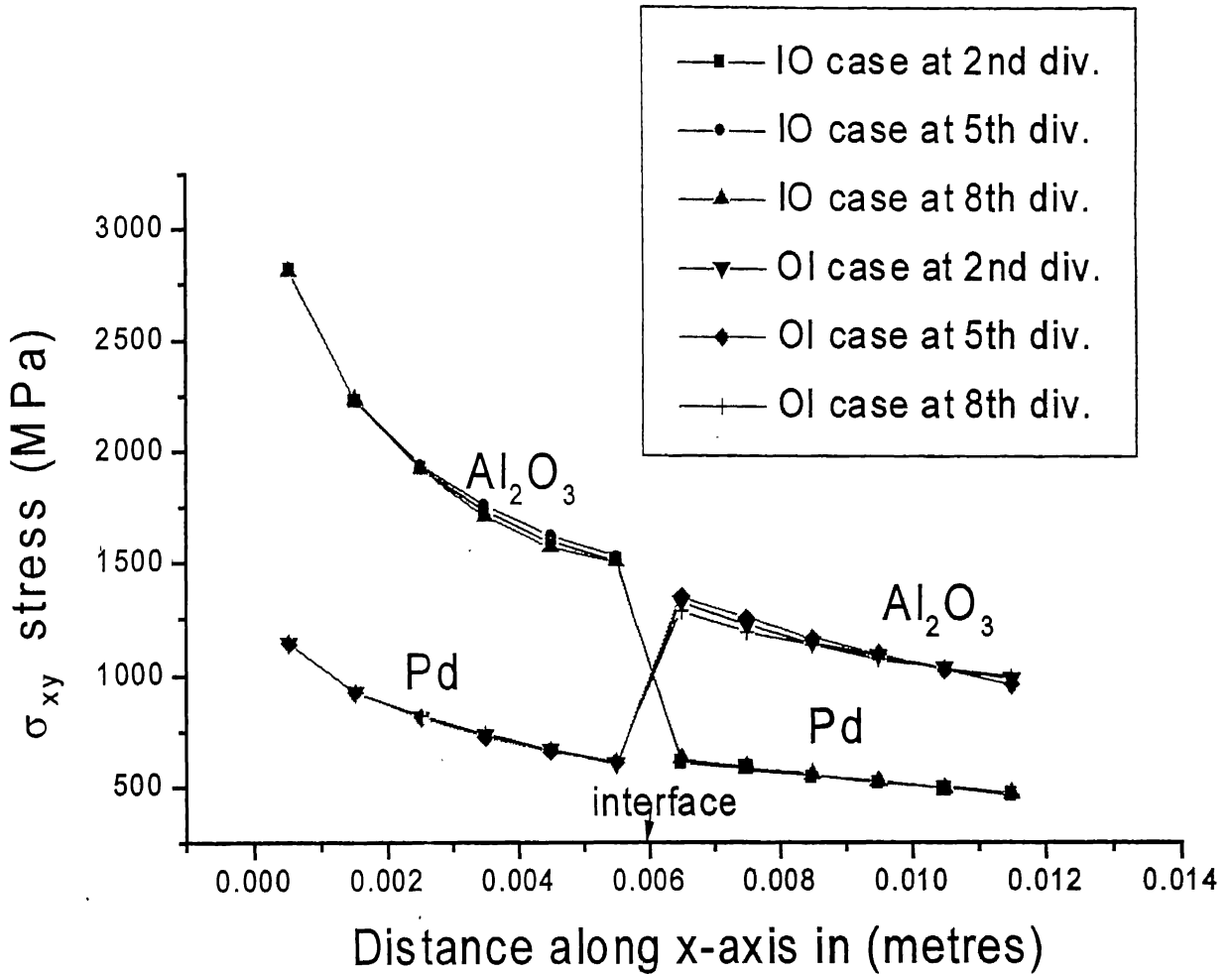


Figure 4.12 -- Variation of stress (σ_{xy}) curve as a function of distance along x-axis at $\Delta T=800\text{K}$ for IO and OI cases.

The radial stress is used for calculating tensile hydrostatic stress for understanding solubility enhancement ratio. Radial stress (σ_{rr}) means the stress is evaluated at 'r' distance whereas tangential stress ($\sigma_{\theta\theta}$) at the 'θ' direction. Figure 4.13.a and Figure 4.13.b shows the variation of radial stress with radial distance for IO and OI cases respectively at $\Delta T = 800K$.

The magnitude of radial stress of Al_2O_3 is more compared to Pd due to high Young's modulus of Al_2O_3 . Average value of gaussian values are taken, the results obtained by 5th, 6th, 7th and 8th divisions are same compared to 4th, 3rd, 2nd and 1st divisions. So, results of 1st, 2nd, 3rd and 4th division are plotted in Figure 4.13.a and 4.13.b.

In both IO and OI case, the major radial stresses are generated at elements at 3rd and 4th divisions and very little is contributed from 1st and 2nd divisions. The value of radial stresses for IO and OI cases become more negative to less negative as the distance increases from origin, this is due to decrease of temperature from inside of composite to outside of composite. The stresses obtained for IO case is more negative than obtained for OI case.

Figure 4.14.a and Figure 4.14.b show tangential stress ($\sigma_{\theta\theta}$) curve as a function of radial distance at $\Delta T = 800K$ for IO and OI cases. The tangential stresses depend on 'θ' values with respect to x-axis. The figures show symmetry with respect to 'θ' values. The stresses obtained for elements at 1st, 2nd, 3rd and 4th divisions are symmetry with 8th, 7th, 6th and 5th divisions respectively. The results obtained for elements at 1st to 4th division are positive where as the values for elements at 5th to 8th divisions are negative. The magnitude of tangential stresses for elements at 1st and 8th division are more than stresses for 4th or 5th division. The results obtained for IO case is more compared to OI case, this is due to previous values of σ_{xx} , σ_{yy} and σ_{xy} . The stresses generated at Al_2O_3 precipitate is more as compared to Pd matrix and it is due to large value of Young's modulus of Al_2O_3 .

4.6 Estimation Of Solubility Ratio Curve

The tensile hydrostatic stresses are generated from radial stresses as given in equation 3.8. Tensile hydrostatic stresses obtained in Pd matrix is averaged and averaged hydrostatic stress value is put in the equation 1.1 to obtain the solubility ratio. The ratio becomes one for 100% Al₂O₃ or 100% Pd matrix, the radial stresses generated for 100% particle is zero. The above ratios are obtained for particular ceramic volume fraction keeping temperature difference constant. Ratios are obtained by varying ceramic volume fraction and these results are plotted in Figure 4.14.a and Figure 4.14.b for both IO and OI cases respectively.

Figure 4.15.a and Fig.4.15.b shows ratio as 1 for 100% precipitate or 100% matrix. The ratio increases with the higher temperature difference. In IO case the ratio slowly decreases due to the decrease of Pd percentage in the composite.

4.7 Estimation of Helmholtz Free Energy

To calculate the potential in composite, Helmholtz free energy density in plane strain condition (eq. 2.7) needs to be written in the component form.

$$\psi = \frac{E}{2(1+\nu)}(\epsilon_{xx}^2 + \epsilon_{yy}^2 + 2\epsilon_{xy}^2) + \frac{1}{2} \frac{E\nu}{(1+\nu)(1-2\nu)}(\epsilon_{xx} + \epsilon_{yy})^2 - \frac{E}{(1-2\nu)}(\epsilon_{xx} + \epsilon_{yy}) \quad 4.28$$

Helmholtz free energy over the total volume is given by

$$\Psi = \int_D \psi .dA \quad 4.29$$

As the radial distance is taken for 0 to 12mm, so the thickness is taken as 1mm. At particular Al₂O₃ volume fraction, HFEs are obtained for fixed tempertaure difference and these results are plotted in Figures 4.16.a and 4.16.b. Figure 4.16.a and Figure 4.16.b show the variation of HFEs as a function of ceramic volume fraction for IO and OI cases at different temperature difference values.

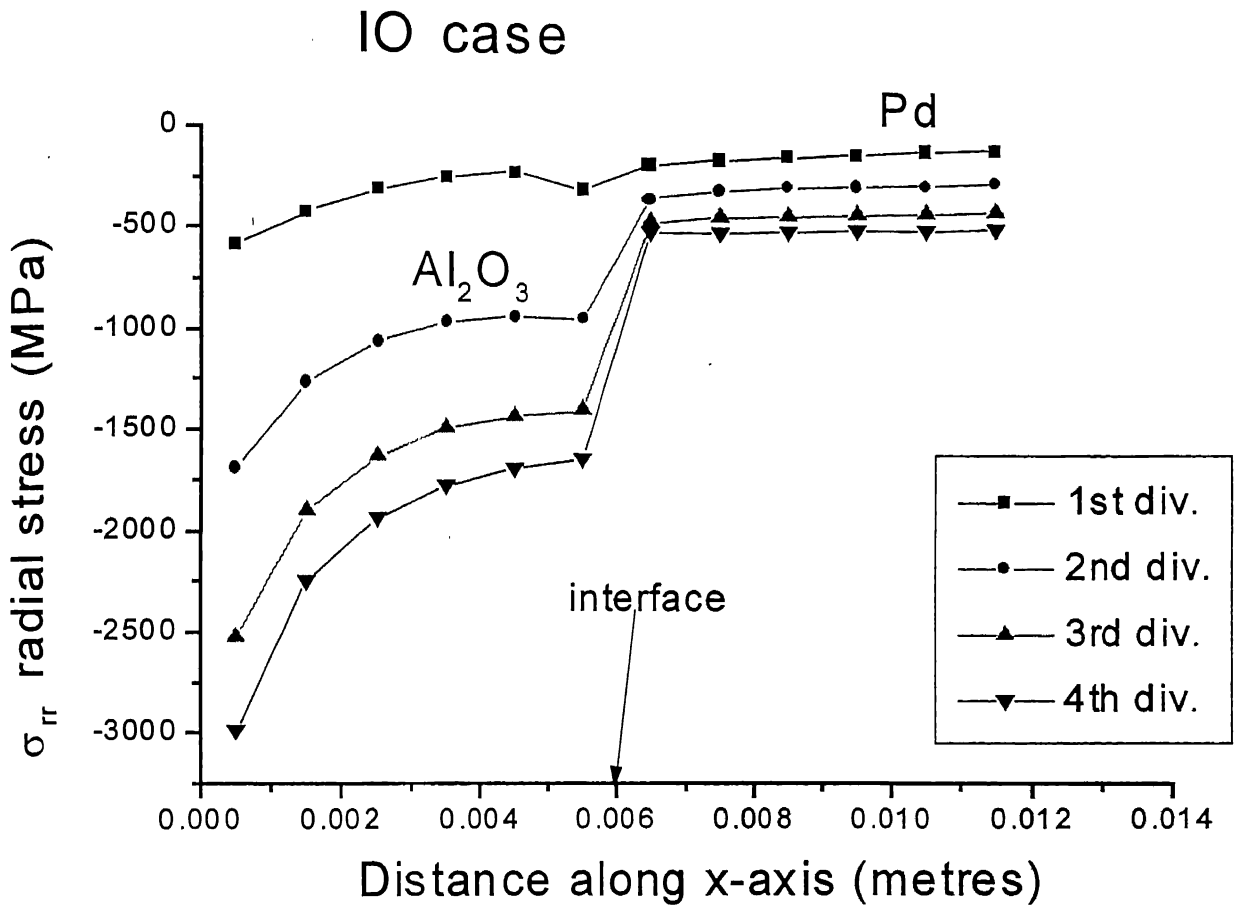


Figure 4.13.a -- Variation of radial stress (σ_{rr}) curve as a function of distance along x-axis at $\Delta T=800\text{K}$ for IO case.

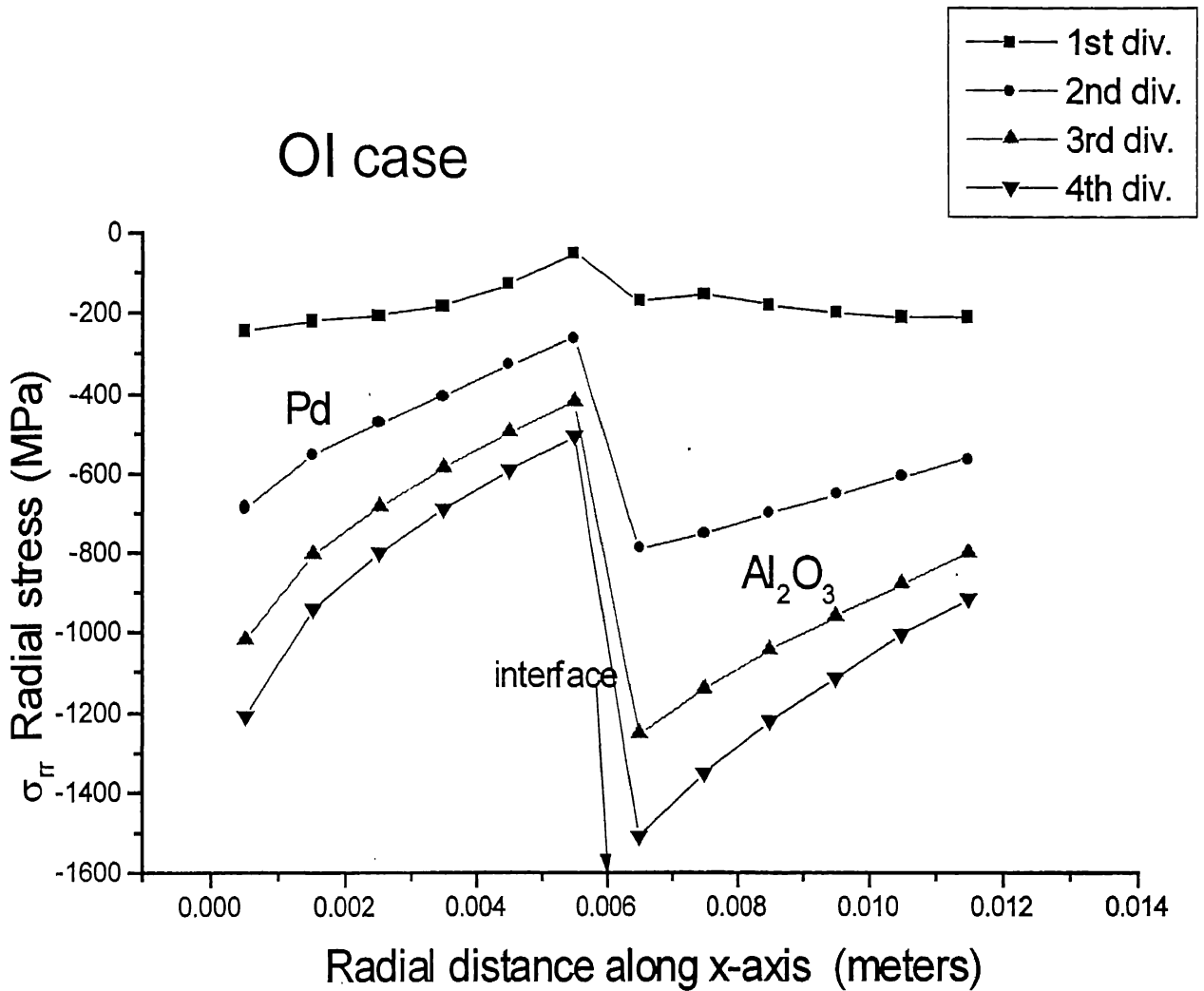


Figure 4.13.b -- Variation of radial stress (σ_{rr}) curve as a function of distance along x-axis at $\Delta T=800K$ for OI case.

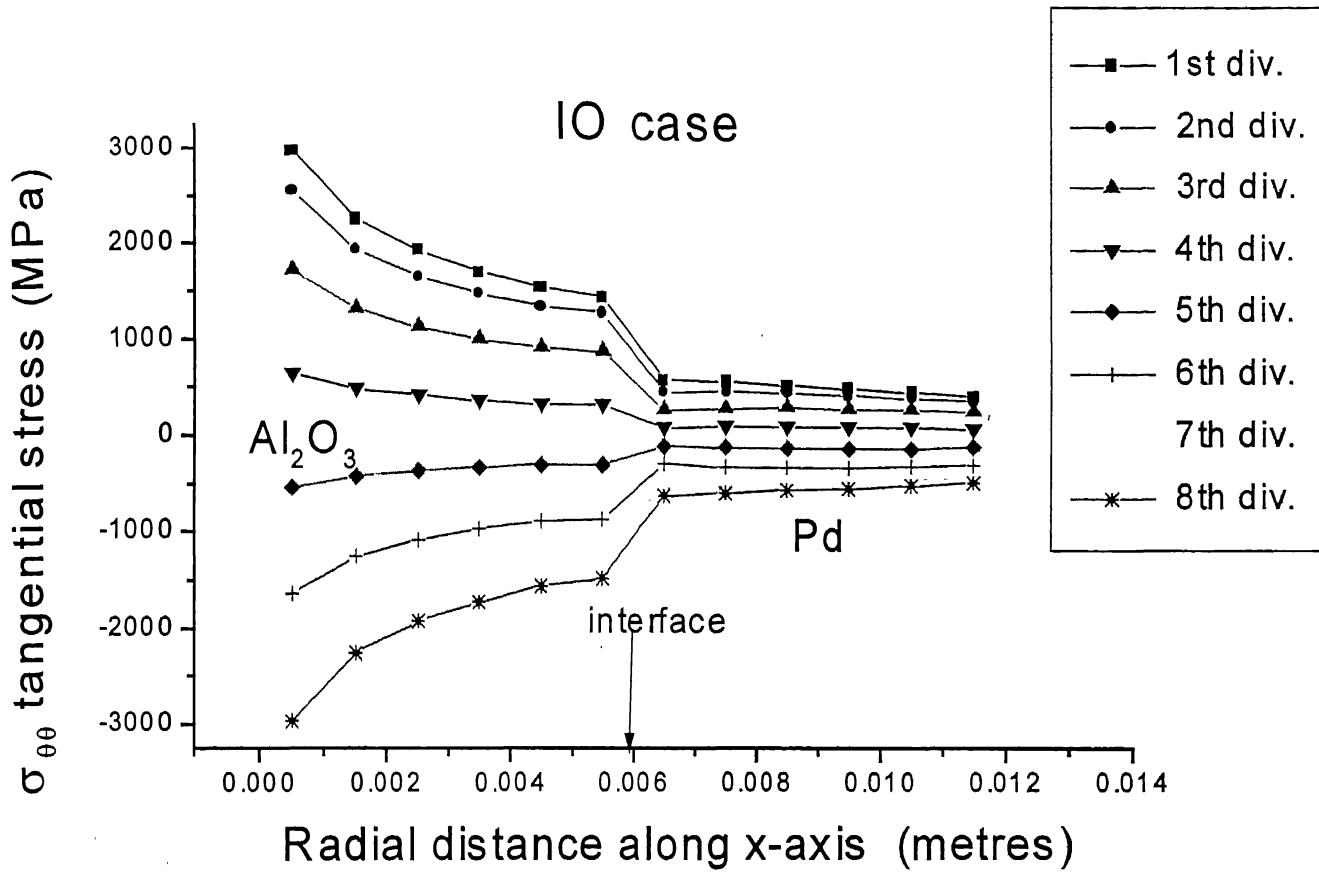


Figure 4.14.a -- Variation of tangential stress ($\sigma_{\theta\theta}$) curve as a function of distance along x-axis at $\Delta T=800\text{K}$ for IO case.

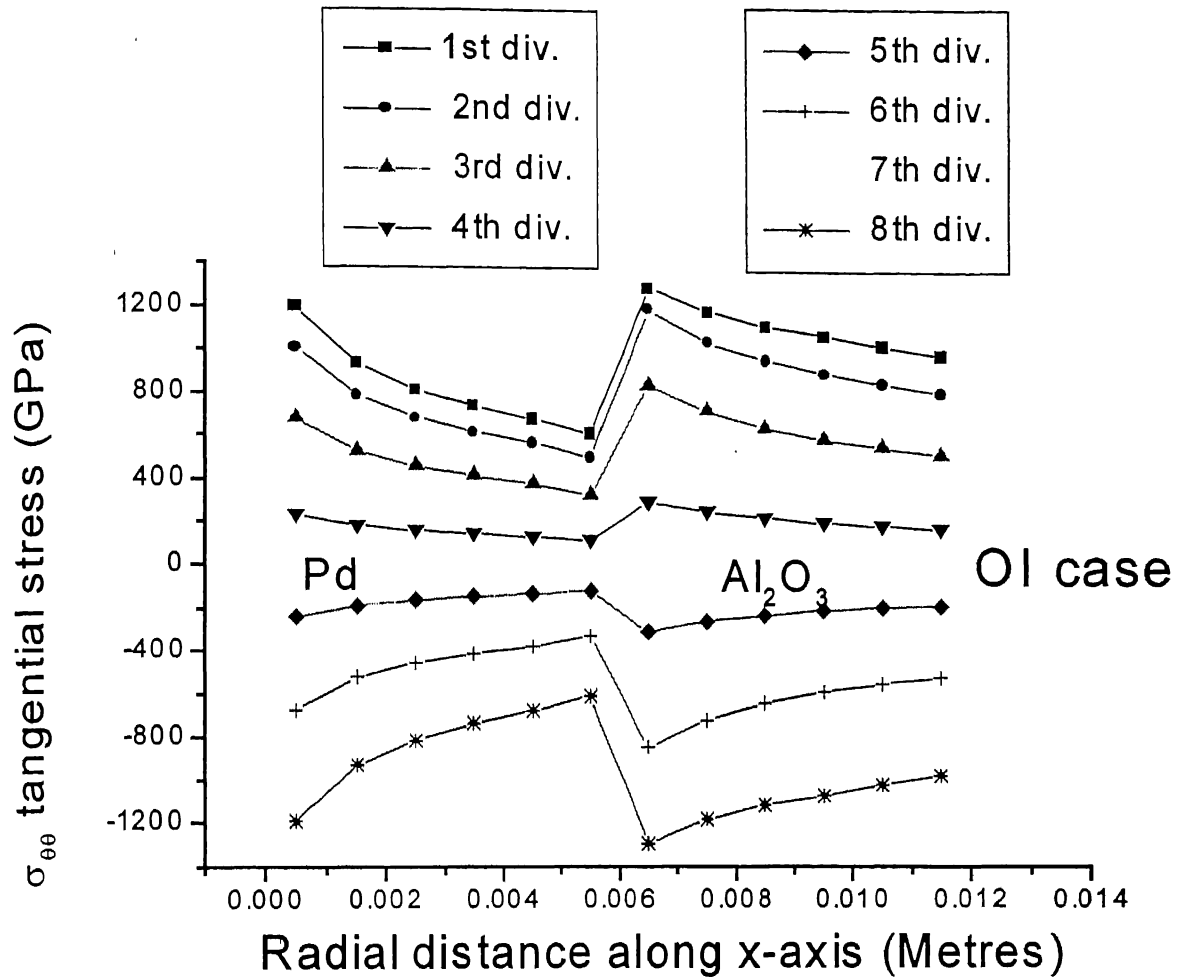


Figure 4.14.b -- Variation of tangential stress ($\sigma_{\theta\theta}$) curve as a function of distance along x-axis at $\Delta T=800\text{K}$ for OI case.

4.6 Estimation Of Solubility Ratio Curve

The tensile hydrostatic stresses are generated from radial stresses as given in equation 3.8. Tensile hydrostatic stresses obtained in Pd matrix is averaged and averaged hydrostatic stress value is put in the equation 1.1 to obtain the solubility ratio. The ratio becomes one for 100% Al₂O₃ or 100% Pd matrix, the radial stresses generated for 100% particle is zero. The above ratios are obtained for particular ceramic volume fraction keeping temperature difference constant. Ratios are obtained by varying ceramic volume fraction and these results are plotted in Figure 4.14.a and Figure 4.14.b for both IO and OI cases respectively.

Figure 4.15.a and Fig.4.15.b shows ratio as 1 for 100% precipitate or 100% matrix. The ratio increases with the higher temperature difference. In IO case the ratio slowly decreases due to the decrease of Pd percentage in the composite.

4.7 Estimation of Helmholtz Free Energy

To calculate the potential in composite, Helmholtz free energy density in plane strain conditions (equation 2.7) needs to be written in the component form

$$\psi = \frac{E}{2(1+\nu)} (\epsilon_{xx}^2 + \epsilon_{yy}^2 + 2\epsilon_{xy}^2) + \frac{1}{2} \frac{E\nu}{(1+\nu)(1-2\nu)} (\epsilon_{xx} + \epsilon_{yy})^2 - \frac{E}{(1-2\nu)} (\epsilon_{xx} + \epsilon_{yy}) \quad 4.28$$

Helmholtz free energy over the total volume is given by

$$\Psi = \int_D \psi . dA \quad 4.29$$

As the radial distance is taken for 0 to 12mm, so the thickness is taken as 1mm. At particular Al₂O₃ volume fraction, HFEs are obtained for fixed temperature difference and these results are plotted in Figures 4.16.a and 4.16.b. Figure 4.16.a and Figure 4.16.b show the variation of HFEs as a function of ceramic volume fraction for IO and OI cases at different temperature difference values.

At 0% Al_2O_3 precipitate, Pd matrix has 100% HFE. With the increase of Al_2O_3 ceramic precipitate, contribution of Al_2O_3 HFEs slowly increases, where for Pd matrix it begins to decrease. At 100% Al_2O_3 precipitate, no contribution is made by Pd matrix. The total HFEs energy is obtained simply by adding energies of Pd matrix and Al_2O_3 energies. The total energies is mainly contributed by Pd matrix as compared to Al_2O_3 precipitate.

Energies obtained from IO case is more than OI case due to large values obtained from strains for IO cases. Energies depend on the strains and temperature and not on stress values. As Pd strains are higher so their HFEs is much higher than Al_2O_3 precipitates.

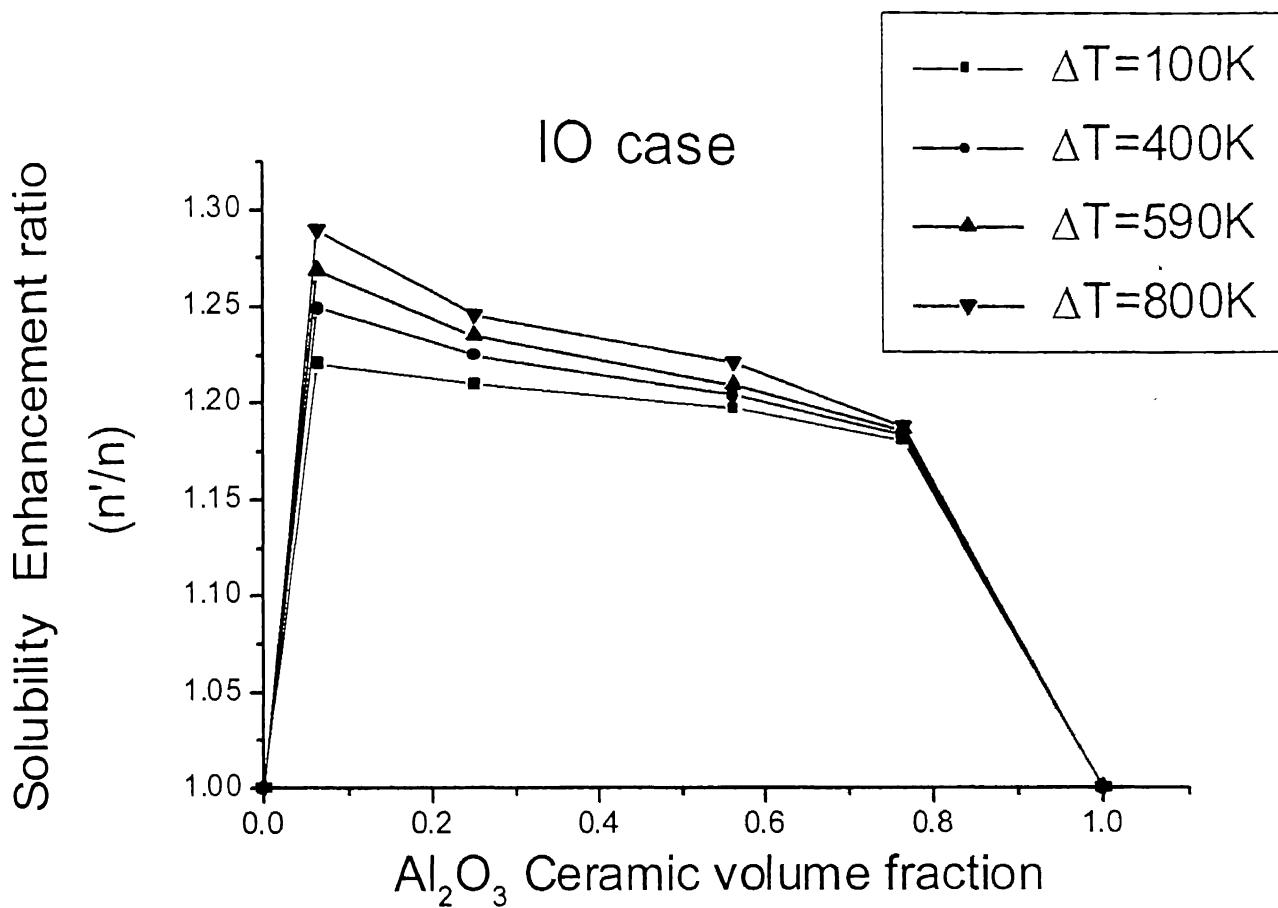


Figure 4.15.a -- Variation of solubility enhancement curve as a function of ceramic volume fraction for different temperature difference values for IO case.

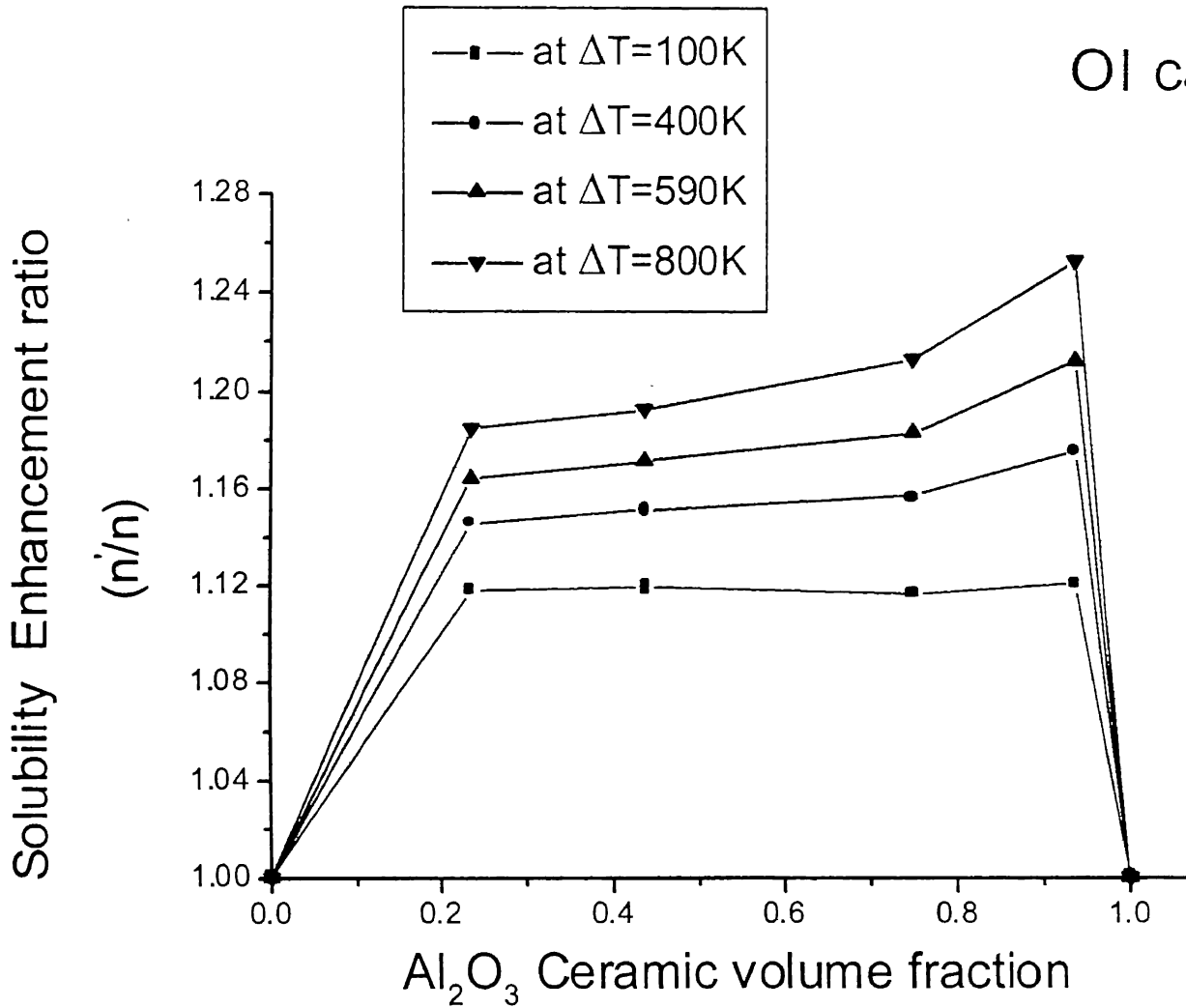


Figure 4.15.b -- Variation of solubility enhancement curve as a function of ceramic volume fraction for different temperature difference values for OI case.

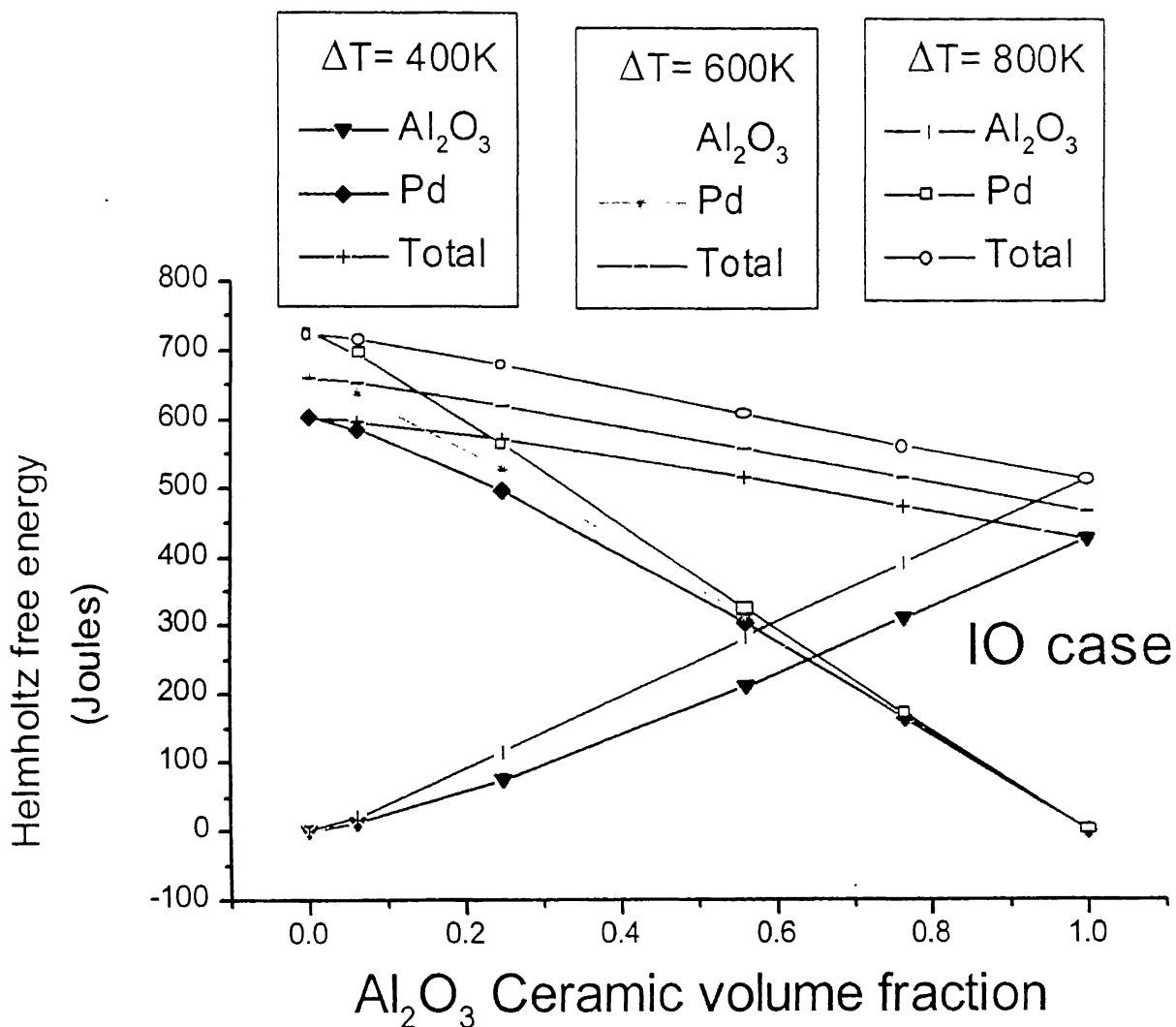


Figure 4.16.a -- Variation of Helmholtz free energy as function of ceramic volume fraction at different temperature difference values for IO case.

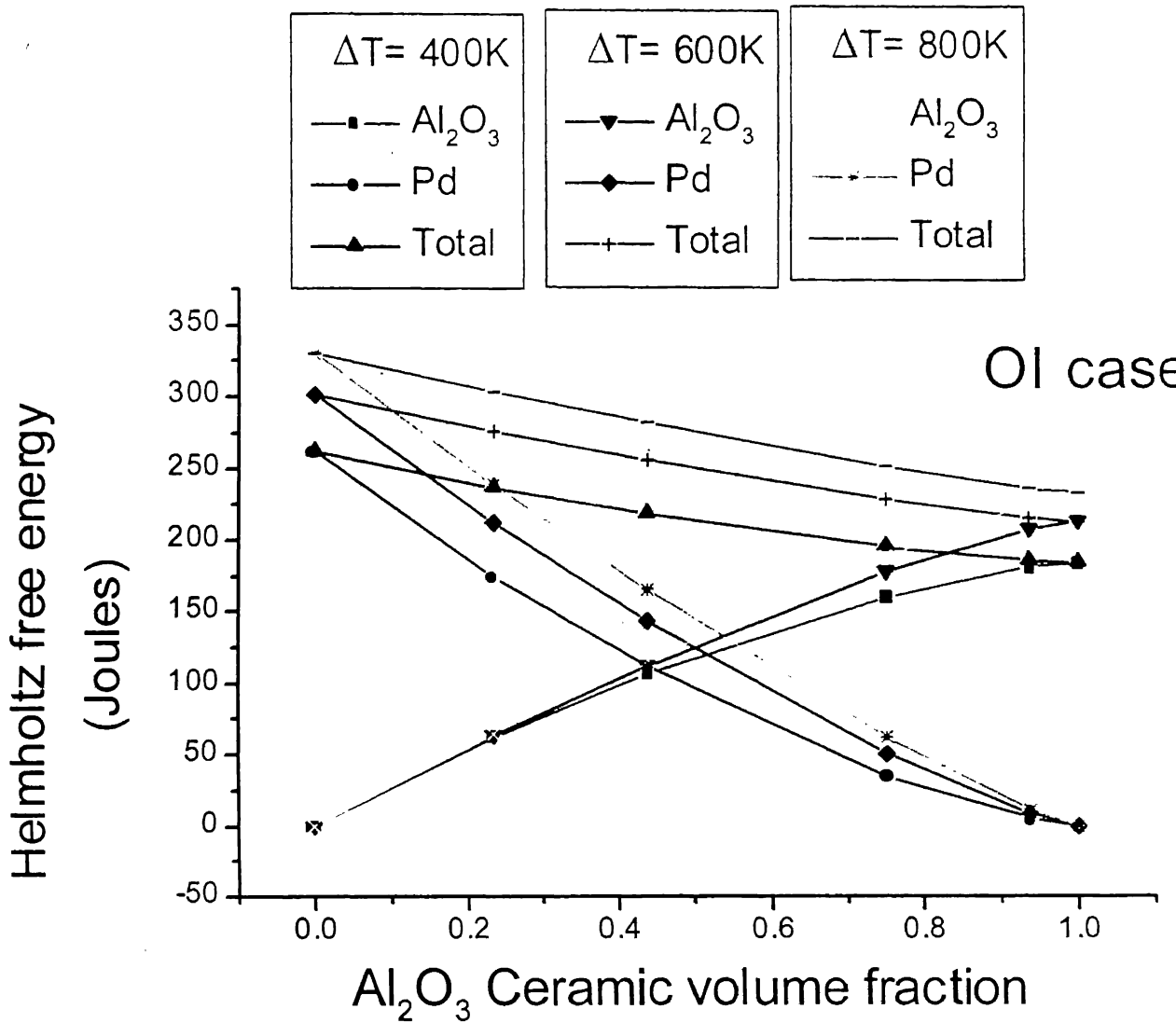


Figure 4.16.b -- Variation of Helmholtz free energy as function of ceramic volume fraction at different temperature difference values for OI case.

Chapter 5

CYLINDRICAL PRECIPITATES (CASE II)

Now we will consider intermediate ceramic precipitates to study the thermal residual stresses in composites. Figure 5.1 shows discretization of intermediate 8 elements precipitates in infinitely long cylindrical matrix. Results are obtained by using 8 elements Al_2O_3 precipitates at different locations. Here residual stress, solubility enhancement and Helmholtz free energy results are evaluated to study the above figure.

Figure 5.2 shows the variation of residual stress as a function of residual distance of 8 elements precipitates. Residual stresses at middle of composite has high magnitude value due to presence of Al_2O_3 precipitates. The stresses slowly increase as we slowly proceed from x-axis to a direction 45° to x-axis. Maximum magnitude of stresses is shown.

Different ratios are obtained at various ceramic volume fraction at constant temperature difference. These results are plotted in Figure 5.3 for different temperature differences. The ratio has value 1 for 0% Al_2O_3 ceramic fraction. As the ceramic volume fraction is increased slowly, the change in ratio is very small. High temperature difference results in high residual stresses which results in high solubility ratio.

Figure 5.4 shows HFEs per mole as a variation of ceramic volume fraction at different temperature difference. The ceramic volume fraction only changes from 0 to 0.15, contribution of Al_2O_3 precipitate on HFEs as compared to Pd matrix is nil. So, only HFEs of Pd matrix and total composites are plotted. HFEs are calculated using equation (2.7). High energies are produced for high temperature difference due to high thermal strains in composites.

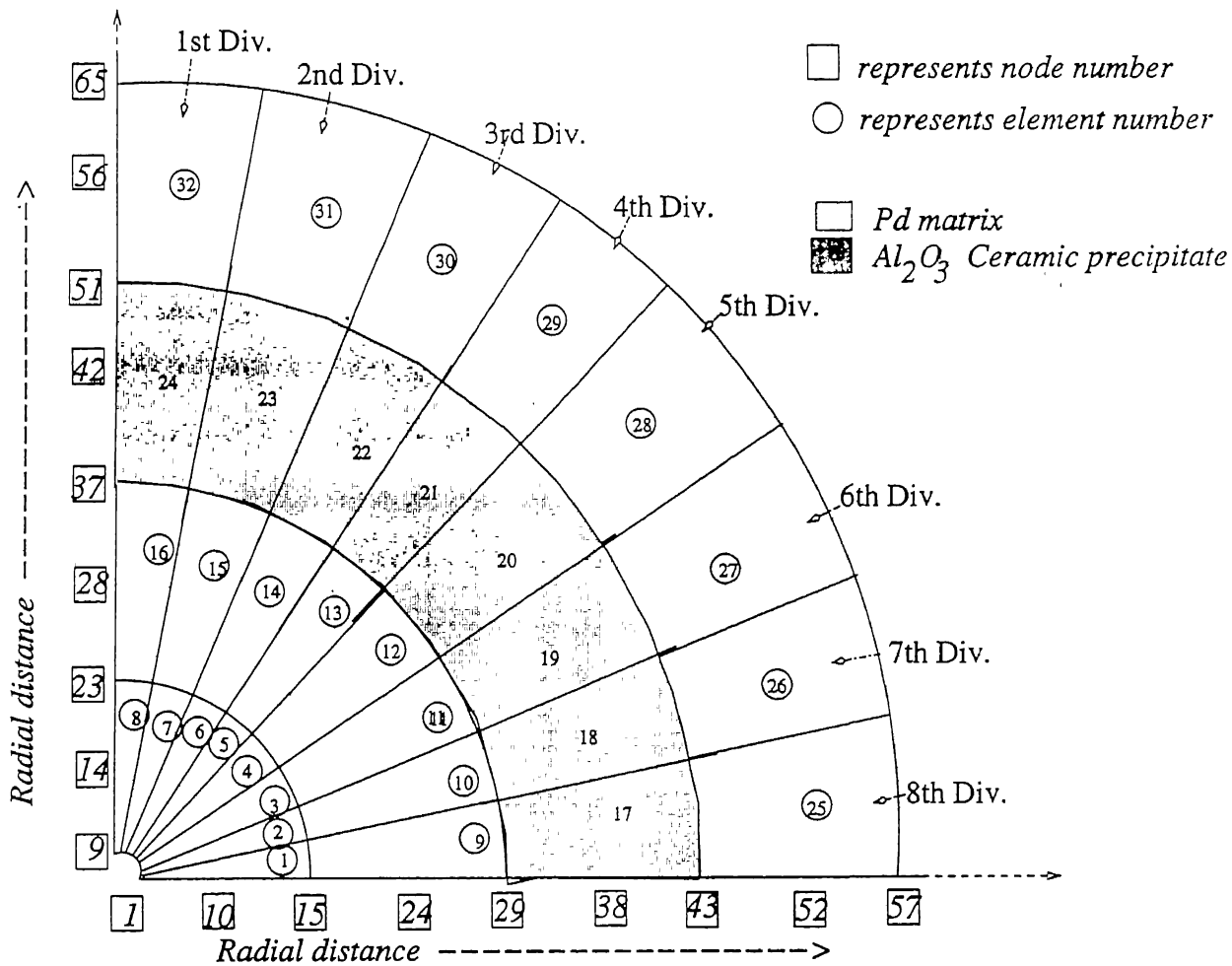


Figure 5.1 - Discretization of the quarter domain using 2-D elements having 8-elements intermediate precipitates.

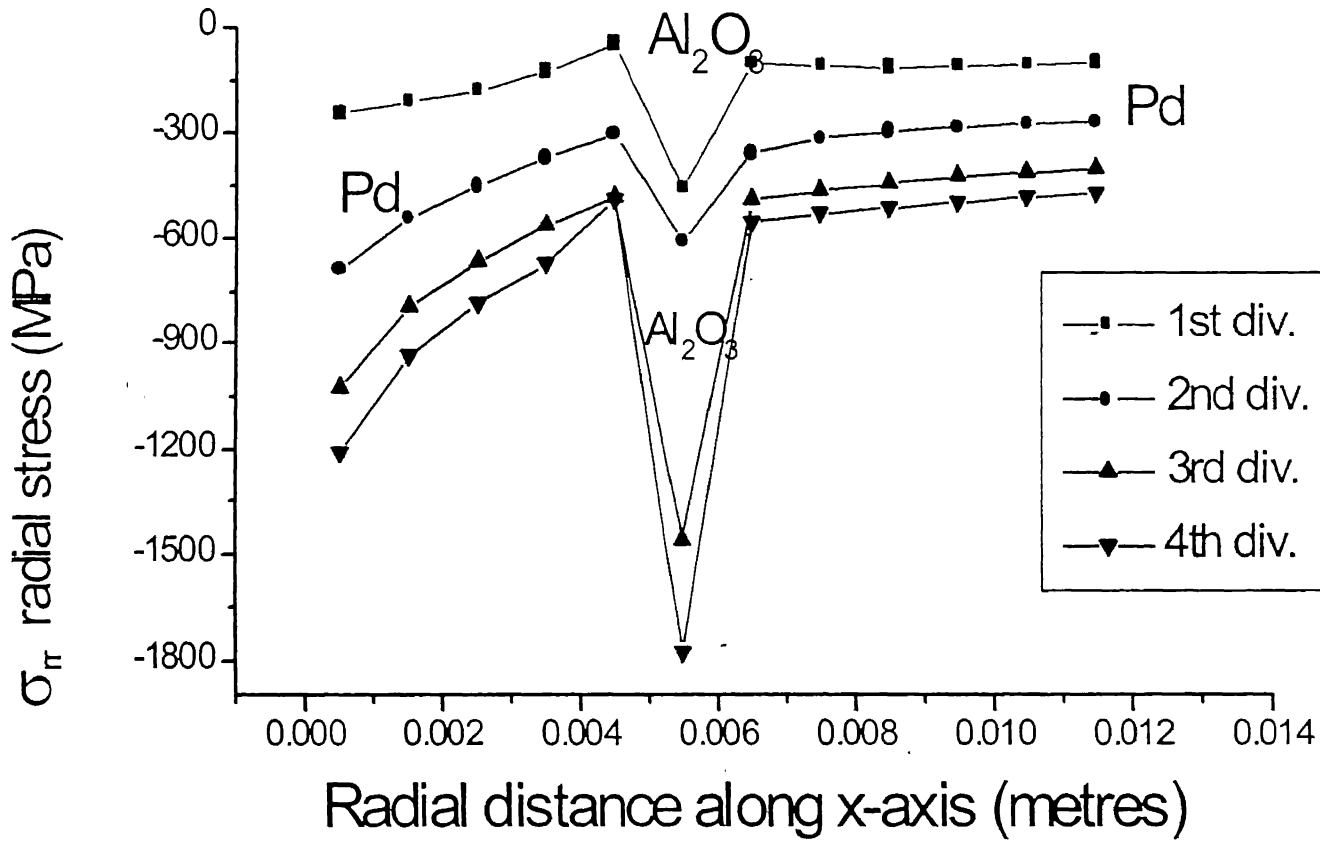


Figure 5.2 -- Variation of radial stress (σ_{rr}) as a function of distance along x-axis at $\Delta T=800\text{K}$ for case II.

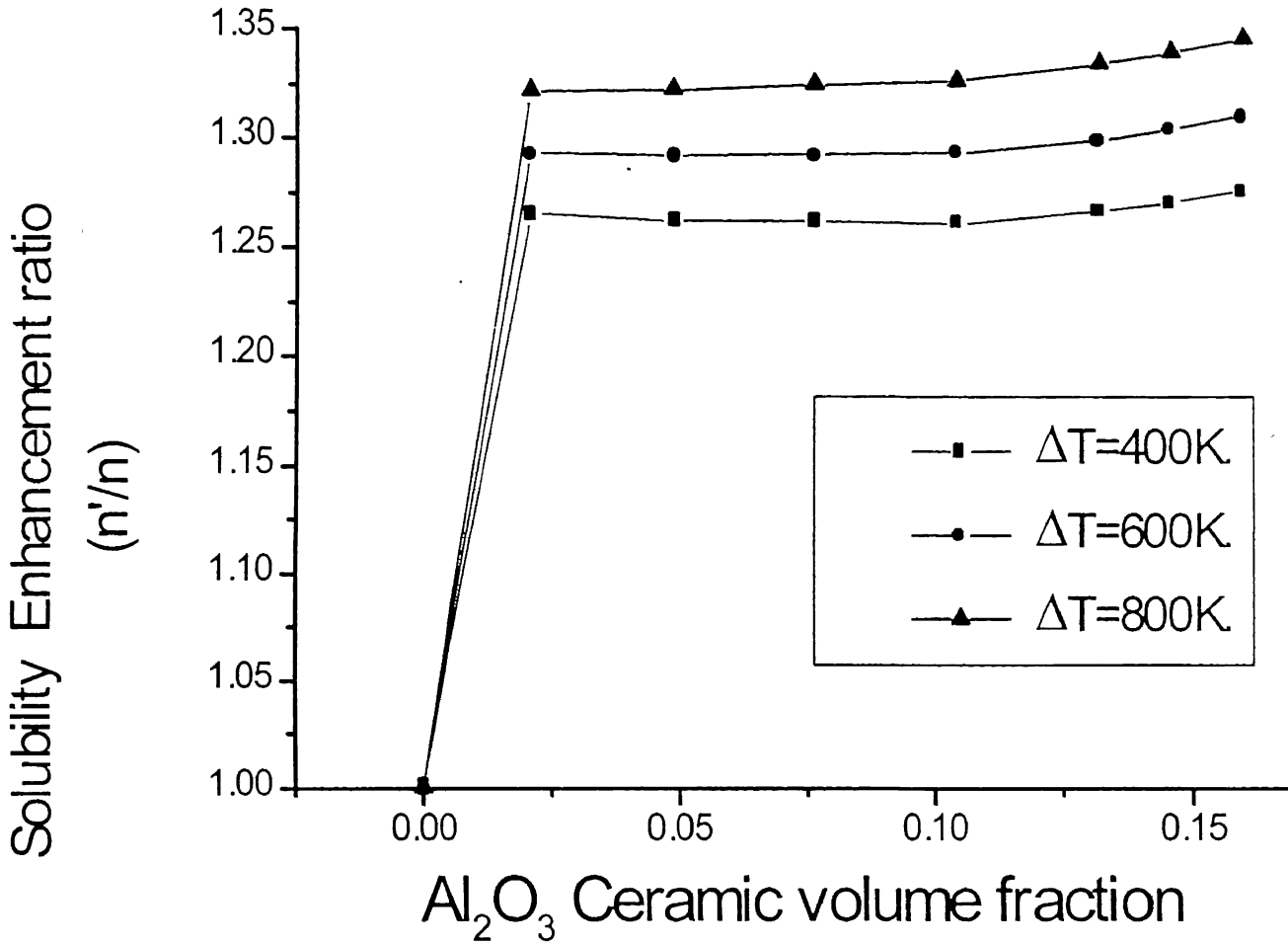


Figure 5.3 -- Variation of solubility enhancement curve as a function of ceramic volume fraction for different temperature difference values for case II.

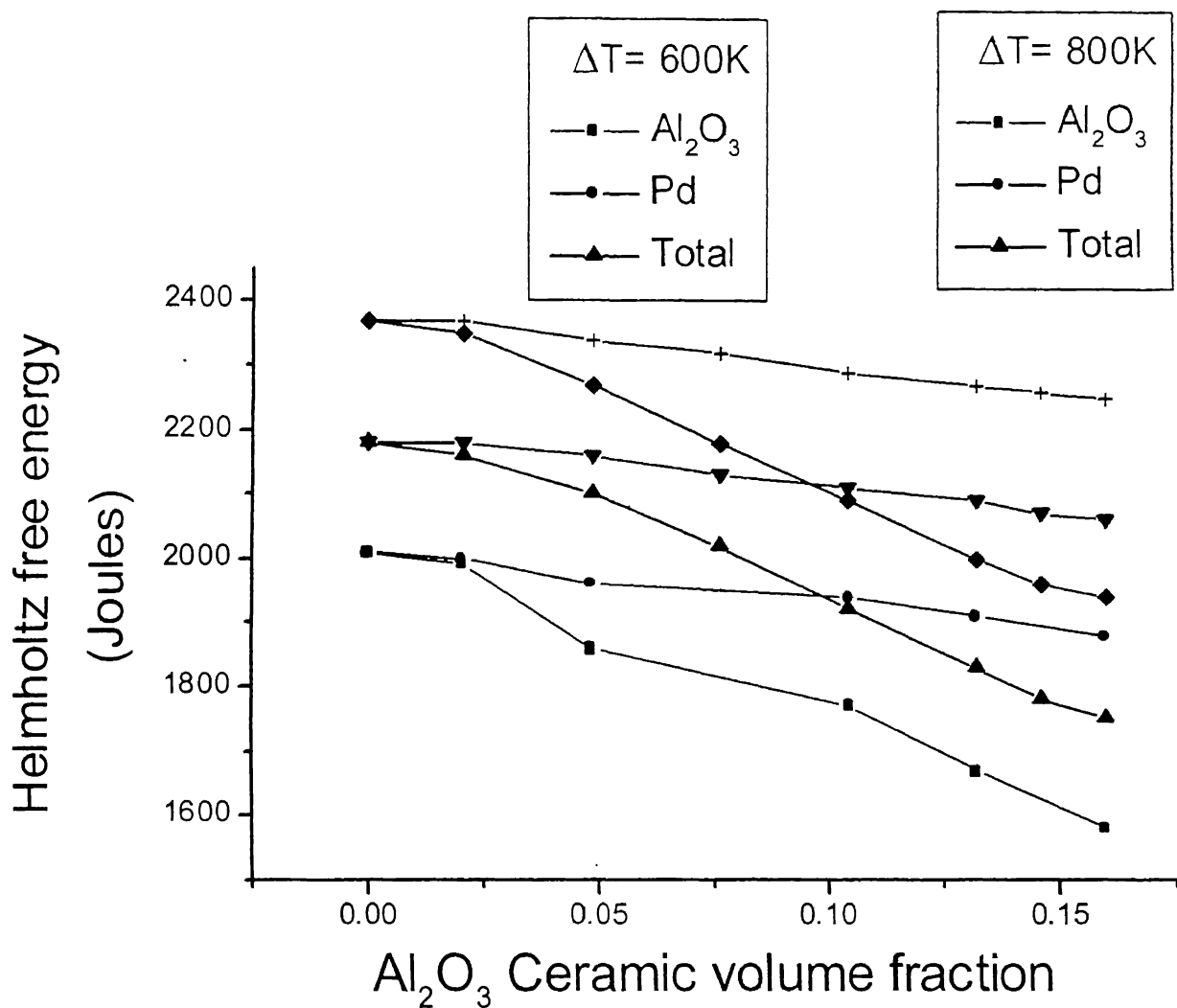


Figure 5.4 -- Variation of Helmholtz free energy as function ceramic volume fraction at different temperature difference values for case II.

Chapter 6

CYLINDRICAL PRECIPITATES (CASE III)

Only 4 Al_2O_3 precipitates are embedded at the middle infinitely long composite at the middle infinitely long composite. Figure 6.1 shows discretization of composite with intermediate 4 ceramic precipitates elements. Here, whole matrix is influenced by only 4 Al_2O_3 precipitates.

Figure 6.2 shows the variation of radial stress as the function of radial distance at $\Delta T = 800\text{K}$. Al_2O_3 precipitate contains in 3rd and 4th divisions, radial stresses at 3rd and 4th divisions are more negative. No changes occur for elements at 1st and 2nd division as it contains Pd matrix only.

Figure 6.3 shows solubility of intermediate 4 elements precipitates as a function of radial distance at different temperature difference. The ratio increases with more temperature difference. The ceramic volume fraction is less compared to precipitates Figure 5.1. The solubility ratio in present case is much more than case II and is shown in Table 6.1.

The volume fraction of Pd matrix of case III is more than that of case II, so HFEs of case III is higher than case II. The contribution of HFEs is very small because its volume fraction is less than 1%. HFEs graph is plotted on Figure 6.4. As the percentage of Al_2O_3 is very less, helmoltz free energy is contributed mainly from Pd matix. In Figure 6.4, HFEs of precipitates are neglected due to low value.

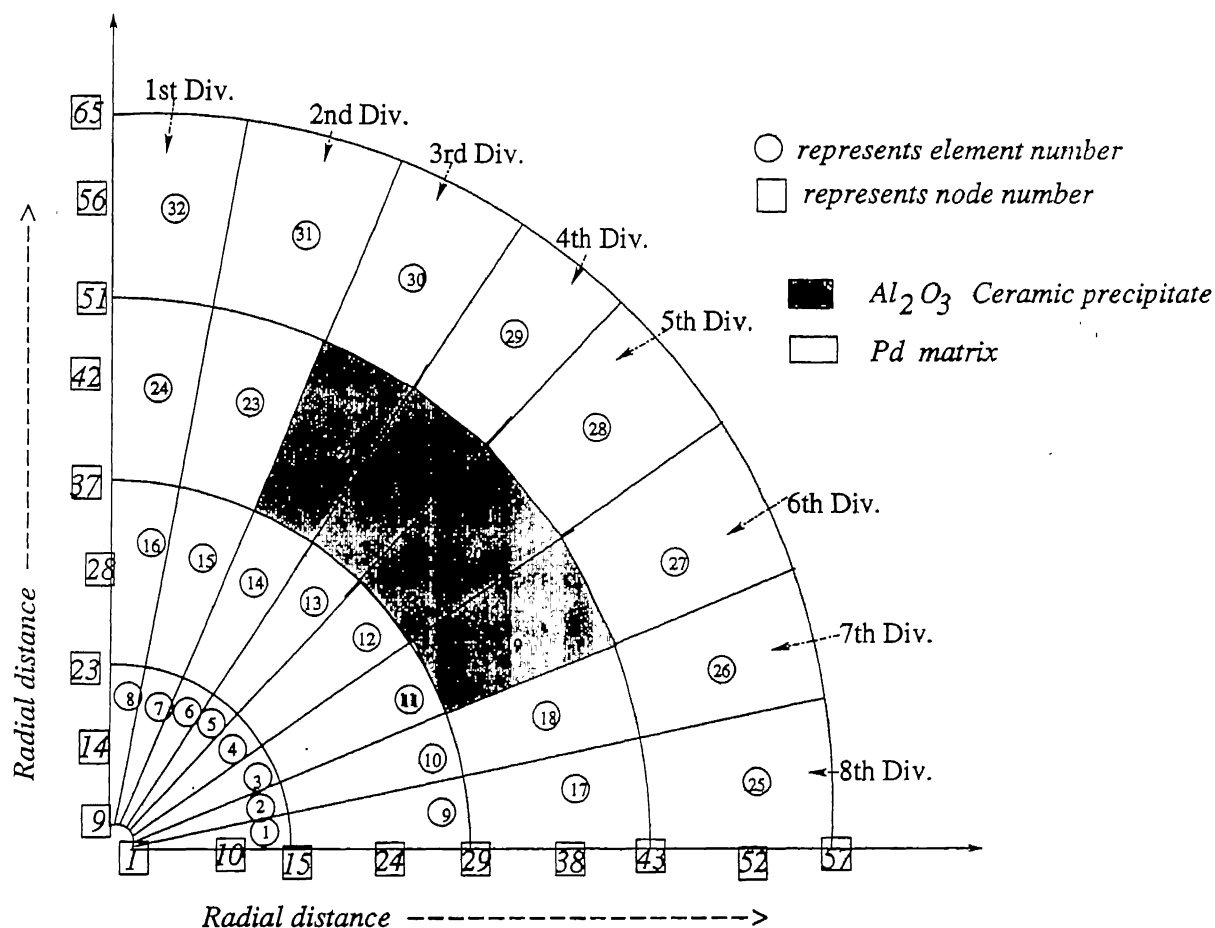


Figure 6.1 - Discretization of the quarter domain using 2-D elements having 4-nodes intermediate precipitates.

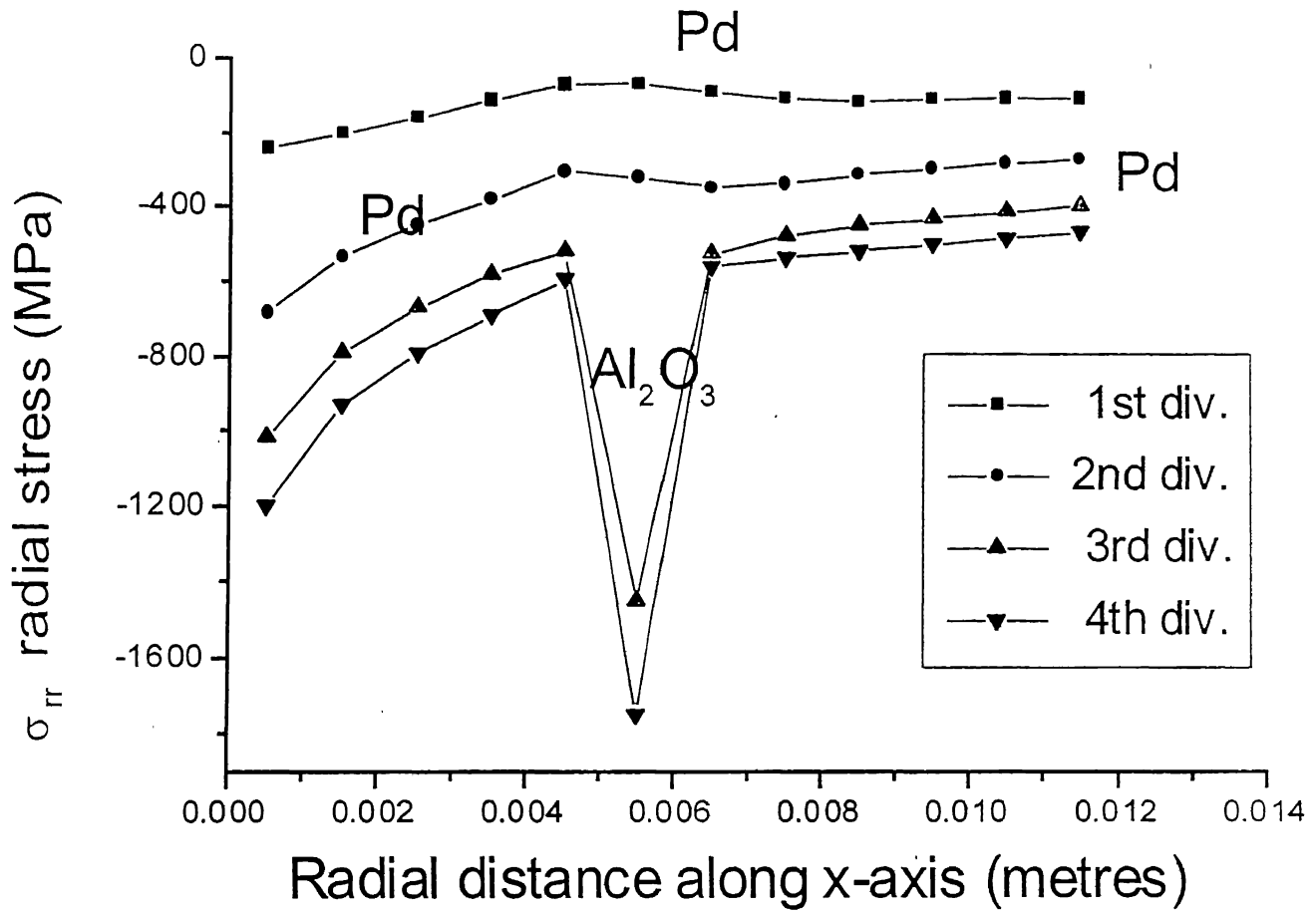


Figure 6.2 -- Variation of radial stress (σ_{rr}) as a function of distance along x-axis at $\Delta T=800K$ for case III.

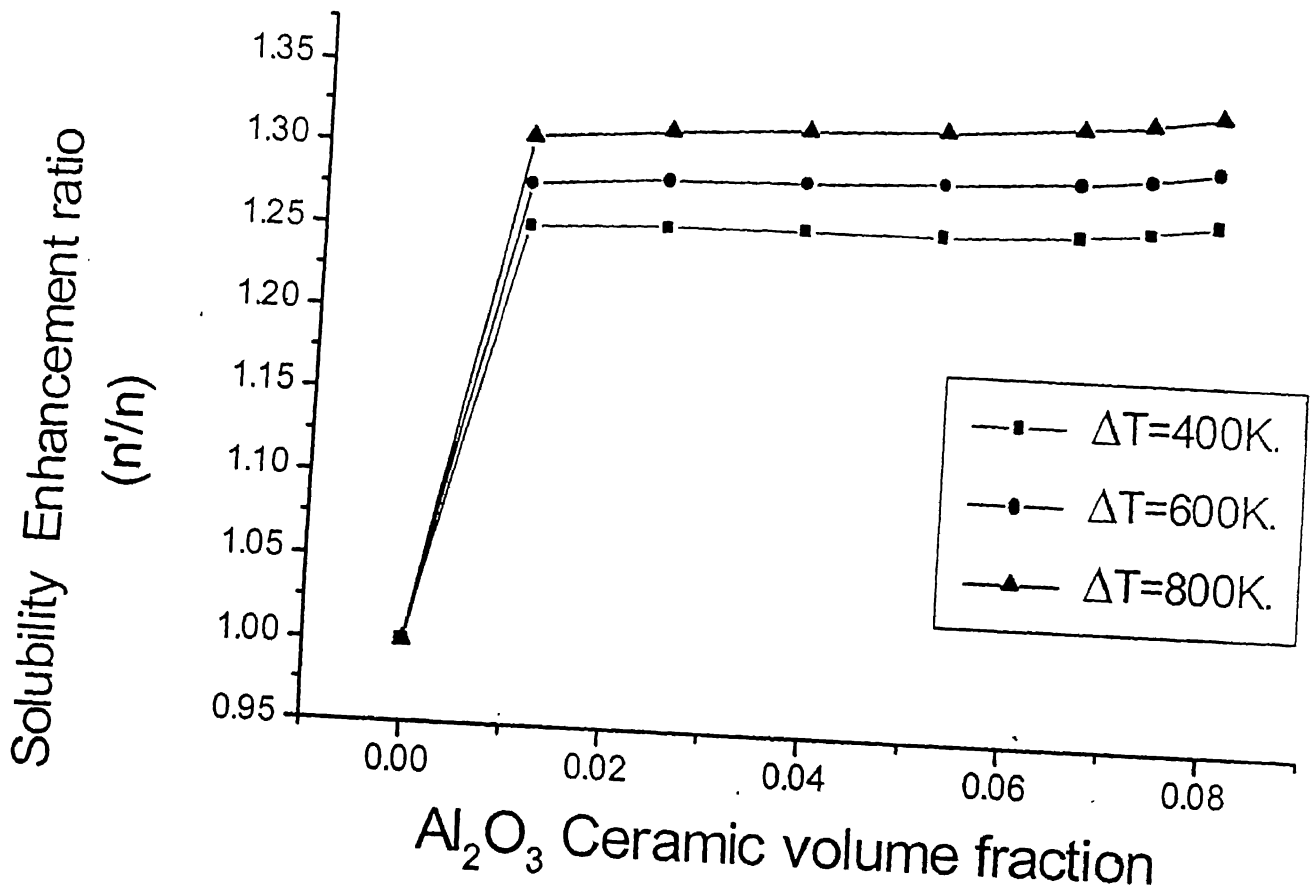


Figure 6.3 -- Variation of solubility enhancement curve as a function of ceramic volume fraction at different temperature difference values for case III.

Ceramic volume fraction	For case II			Ceramic volume Fraction	For case III		
	$\Delta T=400K$	$\Delta T= 600K$	$\Delta T= 800K$		$\Delta T= 400K$	$\Delta T= 600K$	$\Delta T= 800K$
	0	1	1		0	1	1
0.02083	1.26546	1.29344	1.32203	0.0104	1.25303	1.2797	1.30693
0.04861	1.26298	1.2927	1.32313	0.0243056	1.25576	1.28472	1.31435
0.07639	1.26252	1.29365	1.32555	0.0381944	1.2571	1.28738	1.31839
0.10417	1.26238	1.29459	1.32765	0.0520833	1.25854	1.28982	1.32189
0.13194	1.26754	1.3005	1.33575	0.0659722	1.26204	1.29426	1.3273
0.14583	1.2716	1.30578	1.34088	0.0729167	1.2655	1.29816	1.33166
0.15972	1.2772	1.31194	1.34762	0.0798611	1.27117	1.30428	1.33827

Table 6.1 -- Comparison of solubility curve for case II and case III.

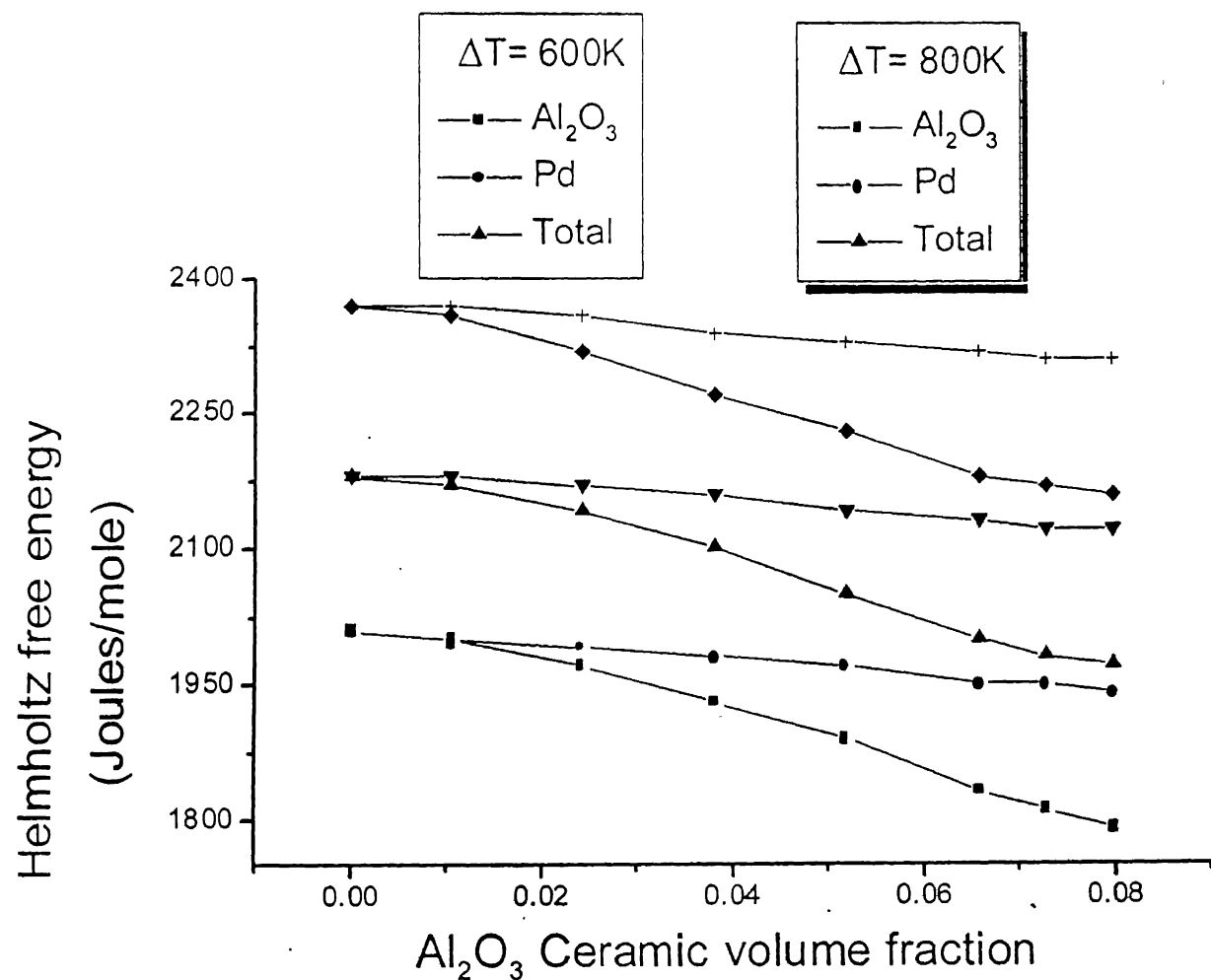


Figure 6.4 -- Variation of Helmholtz free energy as a function of ceramic volume fraction at difference temperature different values for case III.

6.1 Limitations of case I, case II and case III.

It involves plain strain condition so it becomes infinite cylindrical matrix. We cannot predict results for 3-dimensional rather it predicts for 2-dimensional. We assume that strain at z direction is zero so we basically can't predict anything about strain at z direction. Strain energy evaluated at per unit length and it cannot be evaluated over total volume. Elasto-plastic or plastic model are not evaluated to study the plastic behaviour of composites.

Chapter 7

CONCLUSIONS AND SCOPE FOR FUTURE WORK

7.1 Conclusions

The hydrogen solubility enhancements in Pd-Al₂O₃ composites (produced by internal oxidation of Pd-Al alloys) due to thermal residual stresses has been evaluated by the finite element method. The following are the salient conclusions of the study:

1. Two different types of systems were evaluated: spherical and cylindrical. The FEM approach was applied to both the methods.
2. In the case of the spherical system, the alumina was assumed to be within the Pd matrix (IO case) as well as surrounding the Pd phase (OI case). Results were obtained for both the cases. No temperature variation was considered within the Pd-Al₂O₃ and the temperature difference applied to the difference between high and room temperature.
3. The salient conclusions using the spherical system are:
 - (a) For both IO and OI cases, displacements for the Pd matrix were always higher than those in Al₂O₃. This has been explained by the coefficient of the thermal expansion of Pd when compare to that of Al₂O₃.
 - (b) Radial and tangential strains were larger in Pd. This has again been explained by the thermal expansion coefficient of Pd. Moreover, radial strains at the Pd-Al₂O₃ interface showed a irregular discontinuity due to change of material properties. However, the tangential strains a regular discontinuity .
 - (c) The radial stresses developed in the Pd and Al₂O₃ were compressive for both IO and OI cases.
 - (d) Solubility enhancement ratio curve determined for the different volume fraction of alumina in the composite. It was found that the ratio exhibited a maximum for the IO case which appeared at relatively low volume fraction of alumina. This has been explained by the high constraints in the Pd-Al₂O₃ phases. Moreover the

solubility enhancement ratio were higher for the larger ΔT and this has been explained by the higher stresses generated due to large temperature difference.

- (e) Helmholtz free energy (HFE) depends on the strains and the temperature. As the strains obtained in the Pd matrix was always higher, this result in higher HFEs for Pd matrix. In both IO and OI cases, the overall HFEs decreased with increasing alumina fraction.
4. In the case of infinitely long cylindrical system, three types of situations were again considered. In the first situation, the alumina precipitates were considered to be surrounded by the Pd matrix and the volume fraction of alumina was varied. In the second situation, the cylindrical alumina precipitates were placed within the system such that Pd matrix enclosed it on both the sides. In the third situation, the alumina precipitates were placed in specific area of the system. The temperature change occurred within the composite. The temperature change within the composite was considered by ensuring the temperature in the center and outer surface of the composite was different and this was represented by ΔT .
5. Salient features for Case I system were as follows:
- (a) The Pd phase displacements were always high due to its high coefficient of thermal expansion. Displacements varied continuously in the entire composite due to the imposed temperature gradient.
 - (b) Strain in the Pd were always higher in the IO case when compared to OI case
 - (c) Stresses (cartesian) generated in the Al_2O_3 were tensile in nature where as for Pd it was compressive. This has been explained based on the material properties and matches with previously reported results in the literature. The σ_{xy} values were much higher than compared with σ_{xx} and σ_{yy} in both IO and OI cases. The tangential stresses were symmetric with respect to θ values. The radial and tangential stresses of Al_2O_3 were always higher than Pd.
 - (d) Solubility ratio were higher for larger temperature difference. These were higher in IO case when compared with the IO case for all volume fraction of alumina.
 - (e) The Helmholtz free energy of Pd matrix was higher. Higher temperature difference contributed higher HFEs because of enhanced generation of residual stresses.

6. The salient features of the cylindrical system for situation two and three were as follows: The ceramic volume fraction was relatively low in these two cases. As the solubility enhancement ratios obtained for the situations were higher compared to situation one due to large constrained offered by the Pd matrix. Helmholtz free energies depend on strains and temperature. The strains for Pd matrix are always higher than Al_2O_3 . For Case II and III, Al_2O_3 volume fraction is very low so the HFEs for Al_2O_3 is very less compared to Pd matrix. Overall HFEs is also higher than Case I due to greater Pd volume fraction.
7. Finite element method is a powerful technique to analyze residual stresses in composite systems and the present study enhances this viewpoint.

7.2 Scope for future work

1. From the model the strain ϵ_{zz} could not be evaluated. Future work should address this aspect.
2. The models considered here are purely elastic cases. In future work, elasto-plastic and plastic models may be evaluated specially in the case of metal matrix composites.

Chapter 8

REFERENCES

1. R. Balasubramniam, N. Noh, T. B. Flanagan and Y. Sakamoto, *Acta Metallurgica*. Vol. 45, Page 1725-1730, Year 1997.
2. C. T. Kim, J. K. Lee and M. R. Plichta, *Metallurgical Transaction A*, Vol. 21, Page 673-682, Year 1990.
3. S. Ho & E. J. Lavernia, *Thermal Residual Stress in Metal-Matrix Composites : A Review*, *Journal of Advanced Composite Material*, Year 1995,
4. J. L. Meijering, *Advances in Materials Research*, Vol. 5 (Edited by H. Herman), Page 1, John Wiley, New York (1971).
5. N. Birks and G. H. Meier, *Introduction to high temperatures oxidation of metals*, Page 96, Edward Arnold, London, Year 1982.
6. R. Balasubramniam, N. Noh, T. B. Flanagan and J. A. Eastman, *Scripta Metallurgica*, Vol. 34, Page 665, Year 1996.
7. S. D. Tsai, D. Mahulkar, H.L. Marcus, I. C. Noyan and J. B. Cohen, *Material Science Engg.*, Vol. 47, Page 145, Year 1981.
8. H. M. Ledbetter and M. W. Austin, *Material Science Engg.*, Vol. 89, Page 53, Year 1987.
9. A. J. Ardell, *Acta Metallurgical*, Vol. 20, Page 61, Year 1966.
10. J. C. M. Li, R. A. Orani and L. S. Darken, *Journal of Phys. Chem. (N.F.)*, Vol. 49, Page 271, Year 1966.
11. B. Eigenmann, B. Scholtes and E. Macherauch, *Material Science Engg.*, Vol. A118, Year 1989.
12. A. M. Bourka Mark, J. A. Goldston, M. C. Tout and A. Needleman, *Fundamentals of MMC* (edited by S. Suresh) Putterworth-Heinemann, Chap. 4, Page 68, Year 1993.
13. J. D. Eshelby, *Proceeding of R. Society*, Vol. 252A, Page 566, Year 1959.
14. J. D. Eshelby, *Proceeding of R. Society*, Vol. 241A, Page 379, Year 1957.
15. R. J. Arsenault and M. Taya, *Acta Metallurgical Material*, Vol. 35, Page 651,

Year 1987.

16. T. Mura and M. Taya, ASTM STP, Vol. 864, Page 204, Year 1985.
17. K. Tanaka and T. Mori, Acta. Metallurgical Material, Vol. 18, Page 931, Year 1970.
18. K. Wakashima, M. Otsuka and S. Umaker, Journal of Composite Material, Vol. 8, Page 391, Year 1974.
19. S. Ho, PhD Dissertation, Tufts University, Year 1994.
20. E. A. Bigelow, Journal of Composite Technology Res., Vol. 15, Page 304, Year 1993.
21. S. Ho and A. Saigal, Acta. Metallurgical Material, Vol. 42, Page 3253, Year 1994.
22. A. Levy and J. M. Papazian in Proceedings 12th Riso. Ins. Symposium on Material Science, Page 475, Year 1991.
23. N. Shi and R. J. Arsenault, Journal of Composite Technology Res., Vol. 13, Page 211, Year 1991.
24. S. Suresh and T. Nakamura, Acta. Metallurgical Material, Vol. 41, Page 1665, Year 1993.
25. S. Ho and A. Saigal, Material Science Engg., Vol. A183, Page 39, Year 1994.
26. M. Suery, C. Teodosiu and L. F. Menezes, Material Science Engg., Vol. A176, Page 97, Year 1993.
27. A. Saigal, D. S. Kupperman and S. Majumdar, Material science Engg., Vol. A150, Page 59, Year 1992.
28. J. f. Durodola and B. Derby, Acta. Metallurgica Mater., Vol. 42, Page 1525, Year 1994.
29. C. A. Bigelow, Journal of Composite Technol. Res., Vol. 14, Page 211, Year 1994.
30. J. A. Eastman and M. Ruhle, Ceramic Eng. Sci. Proc., Vol. 10, Page 1515, Year 1989.
31. L. C. Cox, Proceedings of ASM's Conference on Residual Stress in Design, Process and Material Selection (W. B. Young, ed.), Metal Parks OH, ASM International, Page 109-115, Year 1987.

32. A. D. Krawitz, "Stress Measurement in Composite Using Neutron Diffraction.", NATO Workshop on Residual Stresses (M. T. Hutchings, ed.), Amsterdam: Kluwer.
33. S. Majumdar, J. P. Singh, D. Kuppermann and A. D. Krawitz, Journal Engin. Mater. Tech., Vol. 113, Page 51-59, Year 1991.
34. S. R. Timoshenko and J. N. Goodier, Theory of Elasticity, Tata McGraw-Hill, Chap. Thermal Stress (Page 435-446), Chap. Stress and Strains in Polar Coordinates (Page 65-70), Year 1982.
35. R. T. Fenner, Engineering Elasticity, Ellis Horwood Ltd., Chap.-12 Finite Element Method, Year 1986.
36. O. C. Zienkowitz and K. Morgan, Finite Element Approximations, John Wiley and Sons, Preface, Page vii, Year 1982.
37. E. Malvern Lawrence, Introduction to the mechanics of a continuous Medium, Prentice-Hall, Chapter – General Principles (Page 271), Chapter – Constitutive Equations (Page 282-285), Year 1969.